ENERGY RESOLVING POWER OF TRANSITION-EDGE X-RAY MICROCALORIMETERS

ENERGY RESOLVING POWER OF TRANSITION-EDGE X-RAY MICROCALORIMETERS

ENERGIESCHEIDEND VERMOGEN VAN RÖNTGENMICROCALORIMETERS MET FASEOVERGANGSTHERMOMETER

(met een samenvatting in het Nederlands)

Proefschrift ter verkrijging van de graad van doctor aan de Universiteit Utrecht op gezag van de Rector Magnificus, Prof. Dr. W.H. Gispen, ingevolge het besluit van het College voor Promoties in het openbaar te verdedigen op maandag 1 maart 2004 des middags te 16.15 uur

door

Wouter Michiel Bergmann Tiest

geboren op 7 augustus 1975, te Naarden

Promotor: Prof. Dr. Ir. J.A.M. Bleeker
             SRON National Institute for Space Research, Utrecht
             Astronomical Institute, Utrecht University

Copromotor: Dr. H.F.C. Hoevers
             SRON National Institute for Space Research, Utrecht

CONTENTS

Contents

CHAPTER 1

INTRODUCTION

In this introductory chapter, we will start with an overview of the research described in this thesis. After that follows an introduction into X-ray spectroscopy.

1.1 Thesis overview

This thesis deals with the development and physical understanding of X-ray microcalorimeters with a high energy resolving power based on transition edge sensor thermometers. An X-ray microcalorimeter of this type is a very small device ($\sim 300~\mu$m across) that measures the energy of a single X-ray photon very accurately ($\sim 0.1\%$). A picture of such a device is shown in figure 1.1. It consists of an absorber and a thermometer. The absorber converts an absorbed X-ray photon into heat. The temperature increase is measured by the thermometer. The thermometer is a superconducting-to-normal phase transition edge sensor (TES). This sensor uses the very steep temperature dependence of the resistance of a superconductor in its transition from superconducting to normal behaviour to act as a sensitive temperature to resistance tranducer. The sensor is operated with a constant bias voltage and the current is read out using a very sensitive SQUID amplifier. The current signal from the thermometer after absorption of a photon is a pulse as plotted in figure 1.2 (left). The area of this pulse is a measure of the energy of the photon. Through filtering of the signal, this energy is determined as accurately as possible from the pulse. When this is done for a number of pulses, the energies can be sorted into a histogram. In this way, an energy spectrum of the radiation is created, as shown in figure 1.2 (right). Thus, the device can be used as a spectrometer.

The point of this thesis is to show that these devices can attain an energy resolution of a level that qualifies them for use in an X-ray spectroscopic instrument, superior to many other energy dispersive techniques. Subsequently, we wish to understand this resolution and investigate what limits it. In order to do so, we start by establishing the theory behind
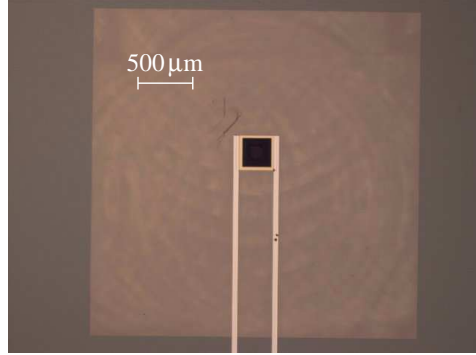
Figure 1.1: Photograph of an X-ray microcalorimeter with a magnification of $1600\times$. The vertical lines are electrical wiring. The dark square in the centre is the absorber which sits on top of the thermometer. The device is supported by a membrane (the large square).
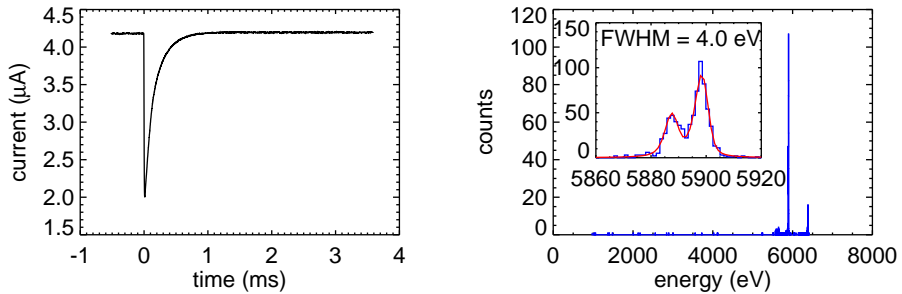
Figure 1.2: **Left**: Electrical signal from an X-ray microcalorimeter after the absorption of a photon. The area of the pulse is a measure of the energy of the photon. **Right**: Histogram of a large number of pulse integrals, calibrated to the energy of the Mn Kα line at 5.9 keV. The inset shows an enlargement of this line, showing that the line components Kα_1 and Kα_2 are resolved. The smooth curve is a fit to the data.

the transition edge sensor. This includes a model of the noise generated in the device and a performance prediction based on this model. Then, we investigate what dictates the design parameters of a TES-based X-ray microcalorimeter. The specifications of a real application, the NFI2 instrument on the XEUS satellite, are used to design such a sensor. After that, we briefly discuss what is involved in fabricating and testing this sensor, and the test results of a few samples are described.

After the functionality of this technique has been established, the focus shifts to understanding the performance of the device. An important part of this thesis is devoted to the question of how the device geometry influences the internal thermal fluctuation noise. This noise component is the result of random movements of energy in the sensor. Using experiments and computer simulations, we examine how this noise can be manipulated. Then, a more accurate model of the sensor responsivity is developed to explain a discrepancy in the predicted and the measured energy resolution. Finally, we have a look at the challenges involved in building a space-borne instrument based on the spectroscopic technique described here.

In the appendices, an overview is presented of all the devices discussed in the text. Furthermore, some topics are treated there that do not pertain to new scientific work, but may be of interest to people involved in detector research: a description is given of the signal processing that is involved in creating the spectra, and the details of a numerical noise simulation are presented. But first, in the remainder of this chapter, we will put the motivation for this work in an appropiate context and assess the potential benefits of a new X-ray spectrometer.

1.2 X-ray spectroscopy

This section deals with the subject of X-ray spectroscopy, since the motivation for the work described in this thesis is the development of an X-ray spectrometer. First, we will discuss how X-ray are produced. For the applications of X-ray spectroscopy, the main focus is on X-ray astronomy, but other fields are also briefly considered. Finally, an overview is given of the most important spectroscopic techniques.

1.2.1 X-ray generation mechanisms

X-rays are electromagnetic radiation with a photon energy between approximately 0.1 and 100 keV. In order to see what information is contained in this type of radiation, we need to look at the origin of X-rays. X-rays can be produced in several ways, of which the most important ones are mentioned here.

Transitions of electrons to a lower atomic energy level can produce characteristic X-ray emission, that is X-ray emission with discrete energies, particular to the element that produces it. The transition occurs when a vacancy in one of the inner electron

shells (usually K or L) is filled by an electron from a higher shell. A photon is then emitted with an energy equal to the difference between the electron levels. The vacancy in the inner shell may be the result of electron capture by the nucleus, as takes place in radioactive decay. Alternatively, the electron may have been ejected from the inner shell by high-energy electrons, photons or heavier particles.

Black body radiation is the thermal radiation as described by Planck's law. When the temperature of an object is 10^7–10^8 K, it emits X-rays with a continuous, thermal spectrum.

Bremsstrahlung is the emission of radiation from high-energy electrons that are decelerated by the electrostatic field of an ion or atomic nucleus. Depending on the energy of the electrons, the emitted radiation lies in the X-ray range. It has a continuous spectrum that can be either thermal or non-thermal. Thermal bremsstrahlung occurs when the electrons and ions are in local thermal equilibrium. When the electrons do not have a Maxwellian energy distribution, it is called non-thermal bremsstrahlung.

Cyclotron radiation is the radiation emitted by high-energy non-relativistic electrons spiraling in a magnetic field. Their continuous acceleration in the magnetic field causes radio, optical and X-ray emission. The spectrum consists of characteristic lines, which depend on the electron velocity and magnetic field strength.

Synchrotron radiation is similar to cyclotron radiation, but the electrons have relativistic velocities. This process can occur in supernova remnants, where the spectrum is continuous and non-thermal, but also in synchrotron accelerators, where very narrow X-ray lines can be generated.

Inverse Compton scattering is the process of low-energy photons gaining energy by scattering from high-energy relativistic electrons. In this way, photons in the X-ray and γ-ray range are created. It is called 'inverse' because energy is transferred from the electron to the photon instead of the other way around, as is the case in regular Compton scattering. It produces a continous, non-thermal spectrum.

The shape of the continuous radiation spectra is determined by the local production conditions (temperature, energy distribution etc.). The presence of specific elements causes characteristic emission lines in the spectrum. Also, when the radiation passes through certain materials, absorption lines are introduced in the spectrum. Therefore, information about high-energy phenomena in the universe and chemical and elemental abundances in stars, gas clouds and material samples can be obtained from spectroscopic X-ray measurements.

1.2.2 Astronomical applications

Astronomical X-ray measurements are an important complement to the observations in the optical and radio range. Since the 1960's, a large number of experiments on balloons, rockets and satellites have been launched to perform measurements of the X-ray sky. There are very many interesting phenomena to be studied in the X-ray universe. We mention a few examples here [1].

First, we will look at phenomena in which collisional ionisation occurs. This is the production of X-rays through interactions within matter, as encountered in hot cosmic gas clouds. There is a large amount of X-ray emission from stellar (including solar) coronae. The spectrum is that of an equilibrium energy distribution with a temperature of about a 10^6 K or higher. In the corona, there are areas of high activity associated with starspots (sunspots) and coronal loops. Using high-resolution X-ray spectroscopy, these areas can be mapped through Doppler imaging. This is done by tracking the movement of emission lines through the spectrum as a function of time, while the star rotates. In this way, information can be obtained about the structure of the corona.

The diffuse X-ray background is the X-ray emission coming from all directions that is not associated with resolved sources. Since it is brighter at low galactic latitudes, a large part of this radiation is believed to originate from the interstellar medium in our galaxy. It has the spectrum of an equilibrium energy distribution with a temperature of $10^6 - -10^7$ K. Study of this spectrum and of the spatial distribution of the emission provides us with information about the composition and structure of the interstellar medium. There is also a spatially more uniform component which has an extragalactic origin.

The gravity of a cluster of galaxies binds a large cloud of hot ($\sim 10^8$ K) gas to the space between those galaxies. From observations of the X-ray emission from this gas, the shape of the gravitational potential in the cluster can be determined. This tells us something about the mass distribution in the cluster, implying the existence of large quantities of 'dark matter'. From the shape of the spectral continuum, the temperature of the gas is obtained, while the characteristic emission lines indicate the composition and therefore the origin of the intracluster medium.

An example of non-equilibrium spectra is found in supernova remnants, see figure 1.3 (left). After a supernova explosion, mass is ejected into the circumstellar environment, which collides with the interstellar matter surrounding the supernova. This creates a shockwave travelling outwards, but also a reverse shock travelling inwards. X-ray spectra and images provide information about the structure of the supernova remnant and also about the properties of the progenitor star.

Next, we will discuss some phenomena that involve photo-ionisation, that is the production of X-rays through interaction with photons. A radiation source irradiates matter around it and creates a photoionized nebula. This occurs in sources powered by mass accretion. Most of the brightest X-ray stars are binaries: a white dwarf, neutron star or black hole and a companion star orbit each other. Mass is transferred from the companion
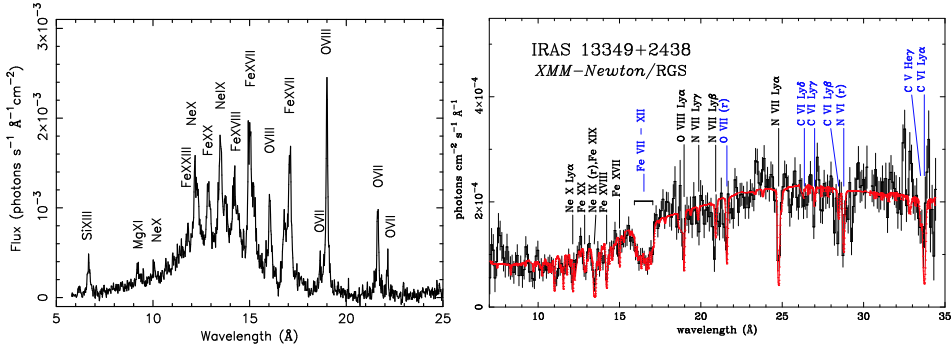
Figure 1.3: **Left**: X-ray spectrum of supernova remnant N 103B taken with the RGS instrument on XMM-Newton. The most prominent emission lines are indicated. Emission is clearly present from ionised O, Ne and Mg. From [2]. **Right**: X-ray spectrum of quasar IRAS 13349+2438, corrected for cosmological redshift, with a fitted model. From the numerous absorption lines, the column densities of various ions in the line-of-sight material can be determined. From [3].

and while it falls towards the accreting star, it emits energy in the form of radiation. The properties of the orbit can be determined from the Doppler shift in the X-ray spectrum as a function of time. If the compact object has a strong magnetic field, the mass will move along the field lines towards the magnetic poles. The X-ray emission will then not be uniform in all directions but will have a beam-like character. If the magnetic poles are off the rotation axis, the direction of the X-ray beam will rotate and the object will be observed as an X-ray pulsar. The rate of change in the pulse period carries information about the system. Another type of X-ray binary is the X-ray burster. Accreted H on the surface of the neutron star fuses into He. When the density and temperature of this He reaches a critical point, a thermonuclear burst may occur. This shows as a sudden increase in X-ray luminosity that decays back to the original level. The process repeats when enough new H is accreted. When the accreting object is very massive, the emitted spectrum is redshifted by gravitation. This redshift can be detected using a high spectral resolution measurement. Thus, X-ray observations can teach us a lot about the evolution of binary systems.

A special type of binary system is the cataclysmic variable. This is a white dwarf showing a nova outburst, which is the result of unstable thermonuclear burning. They are binary systems with a low-mass star as a companion. Between nova outbursts, the accretion disc emits soft X-rays. The study of the X-ray spectra helps understand the way the accretion takes place and what causes the outbursts.

Active galactic nuclei (AGN) are among the most energetic phenomena in the universe. They are thought to be massive black holes in the centre of galaxies, accreting

matter from the surrounding interstellar medium and nearby stars. The accretion disc emits a smooth power-law spectrum of soft X-rays. Fluorescense of the gas surrounding the X-ray source causes an Fe emission line to be present as well. The absorption lines in the spectrum are from the interstellar medium in that galaxy, see figure 1.3 (right).

In addition to all this, there is a growing interest in investigating the early universe. In particular, astrophysicists wonder about the formation of massive black holes and their evolution in terms of mass and spin. The way black holes evolve can be determined from the shape of the Fe K emission line. To resolve this line in detail in nearby AGNs requires high spectral resolution. Furthermore, to be able to detect this line in the earliest AGNs at high redshifts of $z > 5$, a very large detection area is necessary. But a telescope for this purpose should also be able to look at brighter objects. Therefore, it must be capable of a large dynamic range in brightness. And in order to avoid source confusion, the spectral resolving power needs to be combined with a reasonable angular resolution. This is where the future observatories *Constellation-X* (NASA) and XEUS (X-ray Early Universe Spectroscopy mission, ESA and Japan) come in. With effective collecting areas at 1 keV of 1.5 m^2 (Con-X) and 6 m^2 (XEUS) and a spectral resolving power of ~ 1500 around 8 keV, these telescopes should be able to answer questions about the first black holes and dark matter in small (young) clusters of galaxies. Also, the structure of the intergalactic medium and the evolution of galaxy clusters could be studied. This is an important driver for the development of a high-efficiency, high-resolution X-ray spectrometer with imaging capabilities.

1.2.3 Other applications

Besides astrophysics, there are other applications that of X-ray spectroscopy that can benefit from a high-resolution spectrometer.An important application is X-ray microanalysis. Here, a sample is irradiated with an electron beam from a scanning electron microscope. This produces X-rays which are measured with a spectrometer. The emission spectrum shows the concentration of the elements that are present. Because the electron beam is very narrow, extremely precise measurements (~ 1 nm) are possible. This technique has a very wide range of applications, from biology and material science to the semiconductor industry. For the best energy resolution, wavelength-dispersive spectrometers have been used up to now. However, they posess a narrow bandwidth and are not easy to operate. Therefore, an energy-dispersive spectrometer that approaches the energy resolution of the wavelength-dispersive spectrometer is a very useful development [4].

Another application mentioned here is in the field of metrology. There is no well-defined standard of low-energy radioactivity. While they decay, radioactive sources such as ^{55}Fe emit X-rays and Auger electrons at a certain rate. With measurements using a high-efficiency spectrometer, comparisons between activities become possible [5]. Since a measurement of the total emission (including electrons) is desired, this application is not limited to X-ray spectroscopy. Nevertheless, it is mentioned here because the detectors

described in this thesis could be used for this purpose.

1.2.4   X-ray spectrometers

Now that we have an idea of the applications of X-ray spectroscopy, we will take a look at the available instrumental techniques. The quality of spectrometers is expressed in terms of their resolving power. This is the ratio $E/\Delta E$ between the measured energy and the minimum energy difference that can be discerned at that energy. The number can also be expressed as an absolute energy resolution, in units of eV FWHM (full width at half maximum). Spectrometers fall into two categories: wavelength-dispersive (WDS) and energy-dispersive (EDS). For WDS, the resolving power usually increases linearly with *wavelength*, while for EDS, it increases either linearly with or with the square root of *energy*. Therefore, in general, WDS is more suited for low-energy (long-wavelength) radiation, whereas EDS is better for the high-energy (short-wavelength) end. Moreover, there are other factors to consider, such as detection efficiency and bandwidth.

WDS instruments convert the wavelength of the radiation into a dispersion angle, which corresponds to a position on the focal plane. The spectrum is then recorded by a detector, nowadays usually a CCD. There are three types of dispersive elements used in WDS: transmission gratings, reflection gratings and Bragg crystals. A transmission grating spectrometer such as used on the Chandra X-ray observatory has a spectral resolving power of about 800 at 0.5 keV. For the reflection grating spectrometer on XMM-Newton, it is around 400, but with a much larger detection area. Because most of the radiation intensity goes into the zeroeth-order beam which contains no spectral information, the gratings are not very efficient, just 10–20%. Also, because the focal plane areas for the different dispersion orders overlap, there is the problem of order confusion. This can be resolved by using the intrinsic spectral resolution of the CCD.

The Bragg spectrometer uses a crystal that reflects only a specific wavelength which is dependent on the angle of incidence. This type of spectrometer requires a curved crystal or a mechanism for rotating the crystal to scan the diffraction angle. Furthermore, a lot of different crystal types are necessary to get a reasonable bandwidth. Although it has a potentially very high resolving power ($\sim$ 10,000), the fact that only a small range of wavelengths can be measured at a time leads to a very low throughput.

WDS has a very good resolving power, but lacks good imaging capability. For that purpose, we need to turn to EDS. In spectrometers in this category, single photons are absorbed and their energy is measured [6]. This is done in a variety of ways, but in general the photon absorption creates a number of 'signal carriers', which are counted. A factor that determines the energy resolution is the amount of energy necessary for creating a single signal carrier, w. In table 1.1, a number of EDS techniques, discussed below, are summarised. For a measured energy E, the number of signal carriers is $n = E/w$. The variance in this number is $\sigma_n = \sqrt{Fn}$, where F is the Fano factor of the detector. The Fano factor corrects for the error that is made by the assumption of pure Poisson

Table 1.1: Some energy-dispersive X-ray spectroscopic techniques and their approximate signal carrier generation energies.

Detector	Signal carrier energy w (eV)	Preferred application
proportional counter	30	large detection area, $\gtrsim 1$ m^2
scintillator	1000	high energyresponse, $\gtrsim 100$ keV
semiconductor	3	imaging spectrophotometry, $E/\Delta E \sim 40$
superconductor	0.003	low energy imaging spectroscopy, $E/\Delta E \sim 200$
microcalorimeter	-	wide-band imaging spectroscopy, $E/\Delta E \sim 1500$

statistics, and is a property of each detection technique. For instance, for a gas scintillation proportional counter (see below), $F \sim 0.2$. In general, for the energy resolution, we obtain $\Delta E = 2.35 E \sigma_n/n = 2.35\sqrt{wFE}$.

In gas-filled proportional counters, the X-ray photon ionises an atom in the gas, which emits a photoelectron. This causes an avalanche of secondary ionisations, resulting in an electrical pulse with an amplitude proportional to the X-ray energy. The energy resolution is about 1 keV at 6 keV. By measuring the UV light that is produced in the primary ionisation, as is done in a gas scintillation proportional counter, the resolution is improved by a factor of $\sim$ 2–3. These detectors are only used nowadays for specific purposes requiring large areas and are mentioned here mainly for historical reasons.

X-ray scintillators operate by converting X-ray photons into visible light. This light is then measured with a photomultiplier tube. For the scintillator crystal material, NaI(Tl) or CsI(Na) is used. When an X-ray photon is absorbed, an electron is released through the photoelectric effect. This electron produces secondary electron/hole pairs which cause the Tl or Na impurities to emit visible light. The measured light pulse is proportional to the X-ray photon energy. The resolution of this type of spectrometer is $\sim$ 4 keV at 6 keV, which is not very good, but the advantage is that the bandwidth is very large ($\gtrsim 100$ keV).

Semiconductor spectrometers usually consist of a volume of cooled Si or Ge, to which an electric field is applied. When the absorption of an X-ray produces electron/hole pairs, these are separated by the electric field and pulled to the surface contacts. The accumulated charge is proportional to the X-ray energy and can be read out as a current. The detector is usually turned into a diode to avoid a 'leakage current'. The energy resolution of these devices at 6 keV is about 0.14 keV. They form the basis of the charge-coupled device (CCD), which is basically an array of semiconductor detectors. This technology has shown great capabilities for imaging work. If it is ensured that in every CCD read-out cycle there is never more than one X-ray photon absorbed per pixel, the spectral information is conserved. The CCD can then be used as an imaging spectrophotometer.

A rather novel type of spectrometer is the superconductive tunnel junction (STJ). This consists of two superconductive layers separated by a very thin insulator, forming

a Josephson junction. Absorption of an X-ray creates quasiparticles in the supercon-ductor. When the quasiparticles tunnel through the insulator, a charge is transferred from one electrode to the other. This can be read out as a current. The best energy resolution obtained at low energy with an STJ spectrometer is 2.4 eV at 0.5 keV [7]. It is expec-ted that this technique will lead to an imaging spectrometer that approaches the resolving power of WDS at low photon energies.

Another technique involving quasiparticles is the measurement of the change in kin-etic inductance of a superconductor when an X-ray is absorbed [8]. Using this technique for X-ray spectroscopy is very tentative at the moment, but it has the potential of being easily scalable to a large number of elements. This would allow for a high-resolution imaging spectrometer with a very large number of pixels.

The last type of spectrometer discussed here is the X-ray microcalorimeter. This technique involves measuring the temperature increase due to the absorption of an X-ray photon. There are several ways of performing this temperature measurement: ion-implanted Si thermistors have proven to work well. Another way is to measure the change in magnetisation of a paramagnetic material in a small magnetic field [9]. This magnetisa-tion is very sensitive to temperature changes. A third way is to use the steep temperature-dependence of the conductivity of a superconductor near its critical temperature, as does the transition edge sensor. The development of this technique is the subject of this thesis. Compared to other EDS devices, this type of sensor has the advantage of a good energy resolution, a high detection efficiency and a large dynamic range in both energy and in-tensity. It should also be noted that in principle, it can be applied to any interaction that creates heat. So, besides electromagnetic radiation, this detector type can be used for detection of neutrinos or exotic dark matter particles, or for mass spectroscopy. The next chapter will describe the operating principle of this sensor in detail.

CHAPTER 2

TRANSITION EDGE SENSOR

In this chapter, we will discuss some basic physics related to the transition edge sensor, and define some concepts for later use. We will discuss superconductivity and the phase transition, and the way that a voltage bias introduces electro-thermal feedback. Then, we will introduce the noise model and calculate the theoretical energy resolution for a voltage-biased TES-based detector.

2.1 Superconductivity

In this section, we will not go into the details of superconductivity but just mention some of the concepts involved. For a detailed treatment we refer to the literature.

Superconductivity, discovered in 1911 by Heike Kamerlingh Onnes at Leiden, is the phenomenon of a conductor losing all its electrical resistance when cooled below a certain critical temperature T_c. Another important property is that all magnetic field is expelled from the superconductor when it is cooled below T_c. The superconducting effect is removed when a magnetic field stronger than the critical field H_c is applied. This critical field is temperature-dependent. A current through a superconductor will induce a magnetic field, and so there is also a critical current I_c associated with the critical field. Currents higher than I_c will drive the superconductor normal.

There are two types of superconductors: elemental superconductors are generally of type I while alloys are of type II. Unlike type I, type II superconductors exhibit a so-called mixed state, in which there is a partial flux penetration above a field H_{c1}. They go normal at a field H_{c2} which can be much higher than the critical field of a type I superconductor. Thin films of elemental superconductor material can behave as type II, due to a mean free path that is short compared to the London penetration depth. This is the distance from the surface of a superconductor to the point inside at which the strength of an applied field is reduced with a factor $1/e$.
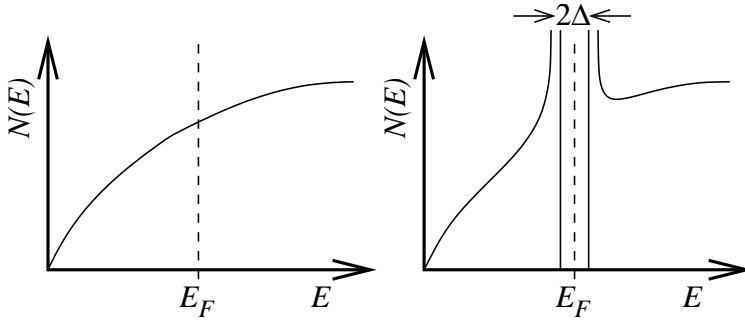
Figure 2.1: Sketch of the density of available electron states as a function of energy for electrons in the conduction band of a normal metal (left) and for a superconductor (right), showing the energy gap around the level of the Fermi energy E_F.

Superconductivity is based on attractive electron-electron interactions that lead to the formation of Cooper pairs of electrons which condense into the ground state. This results in a gap $\Delta = 3.5k_BT_c/2$ (at $T = 0$ K) in the excitation energy spectrum of the electrons. Therefore, electron states of certain energies are not available, as shown schematically in figure 2.1. The Cooper pairs have a much larger length scale than conduction electrons, and this prevents the interactions that cause resistivity in normal conductors. This is why a superconductor exhibits no electrical resistance. The gap size decreases with increasing temperature and disappears at $T = T_c$. The material then goes from the superconducting to the normal phase.

2.2   Phase transition and critical temperature

Now, we will describe some aspects of the phase transition. We will not perform detailed calculations, but will try to give an order of magnitude for the parameters involved and show in what way they interact. The transition from the superconducting to the normal phase takes place within a temperature range of a few mK. The resistance then changes from zero to a finite value, making a superconductor a very sensitive resistive thermometer. An example of such a transition is shown in figure 2.2. The shape of the transition depends on the purity of the material and, in the case of thin films, on the applied magnetic field. The critical temperature is a property of each superconducting element. For a desired T_c, a suitable elemental superconductor may not be available. Fortunately, the T_c of a material can be changed by using a combination of elements. When a normal metal and a superconductor are placed in contact with each other, some Cooper pairs may be exchanged with quasiparticles from the normal metal, effectively suppressing the T_c of the superconductor (and inducing some superconductivity in the normal metal). This is
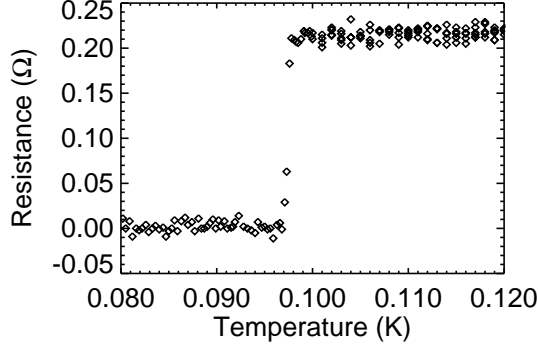
Figure 2.2: Example of the superconducting to normal transition of a Ti/Au bilayer. In bulk form, Ti has a critical temperature T_c of 0.40 K. By using a bilayer of 18 nm Ti and 30 nm Au, the T_c was suppressed to 0.097 K.

called the *proximity effect*. By changing the film thicknesses of the superconducting and the normal metal, the strength of this effect can be adjusted and the T_c of the bilayer can be tuned. For the Cooper pairs, a so-called intrinsic coherence length can be defined:

$$\xi_0 = \frac{\hbar v_F}{\pi \Delta} \tag{2.1}$$

$$\approx 0.18 \frac{\hbar v_F}{k_B T_c} \tag{2.2}$$

where v_F is the Fermi velocity. For a pure superconductor, there is almost no suppression of T_c when the thickness exceeds ξ_0. For thinner films, T_c is suppressed further with increasing normal metal thickness, until the coherence length of the normal metal is reached:

$$\xi_n = \sqrt{\frac{\hbar D}{2\pi k_B T}} \tag{2.3}$$

where $D = v_{Fn} l_n / 3$ is the diffusion constant of the normal metal, with v_{Fn} its Fermi velocity and l_n its electron mean free path [10]. For greater normal metal thicknesses, T_c stays constant. This is schematically illustrated in figure 2.3. In thin films at low temperature, the mean free path l_n will be limited by the film thickness. Therefore, normal metal films with thicknesses below $(\hbar v_F/(6\pi k_B T))^{1/3}$, will always be thinner than their coherence length.

These coherence lengths give an upper limit as to the required thicknesses for the desired suppression of T_c. In practice however, there appears to be quite a large margin
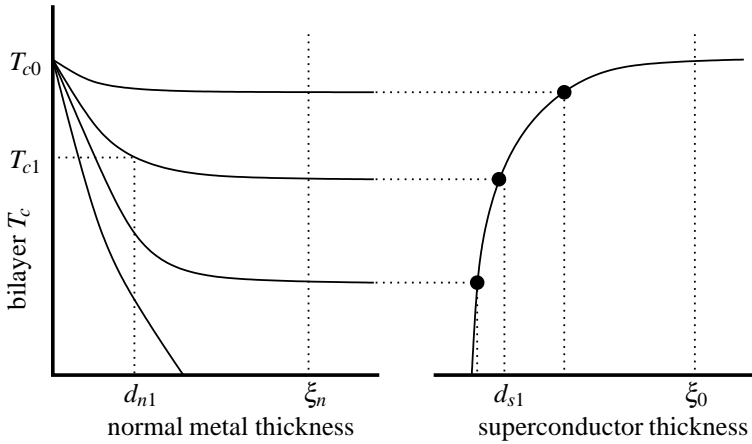
Figure 2.3: Schematic illustration of the influence of the proximity effect on the critical temperature of a superconductor/normal metal-bilayer. T_{c0} is the T_c of the bulk super-conductor. The curves in the left part correspond to different superconductor thicknesses, which are indicated in the right part. For instance, for a given superconductor thickness d_{s1} in the right part, one finds the corresponding curve by following the dotted line up-wards and then left into the left part. Then, for a certain normal metal thickness d_{n1}, the bilayer T_c can be read off from this curve and is found to be T_{c1}. The curve on the right describes the T_c of a bilayer with the normal metal layer thicker than its coherence length, as a funcion of the superconductor thickness. Adapted from [10].

in these thicknesses, and precise tuning is somewhat of a matter of trial and error. From the figure, it is clear that there are many combinations of thicknesses possible for a single T_c. The desired T_c is reached most easily by first adjusting the normal metal thickness to the desired resistivity and then varying the superconductor thickness. An important factor is also the quality of the interface between the layers, and this depends strongly on the deposition conditions. In principle it is possible to predict the T_c of a bilayer [11], but in practice the value will vary from one fabrication setup to another. For a reproducible T_c, a clean interface between the layers is very important.

The choice of materials will be very much dictated by practical considerations, such as available equipment and materials. The materials should be chemically stable. The normal metal is preferably a noble metal, so as to avoid degradation through oxidation. At the National Institute for Space Research (SRON), we have used bilayers of Ti ($T_c = 0.40$ K) and Au for a target T_c of 0.10 K. For 50 nm of Au, the normal metal coherence length is 0.53 μm, so the film has a thickness of about 10% of this value. The intrinsic coherence length for Ti is 5.9 μm, and the thickness needs to be well below that for the desired suppression of T_c. In this case, 14 nm of Ti has resulted in a T_c of 0.10 K. Other groups use bilayers with Mo, which has a T_c of 0.92 K; the group at the National Institute of Standards and Technology (NIST) uses 60 nm Mo/200 nm Cu while the group at NASA's Goddard Space Flight Center (GSFC) uses 50 nm Mo/270 nm Au for a T_c of 0.10 K. This T_c is chosen as low as possible to minimise noise, but such that the thermometer can be operated in the limit of extreme electro-thermal feedback using practical cooling. This will be explained in the next section.

2.3 Voltage bias and electro-thermal feedback

Before we explore the use of the TES thermometer further, we need to consider the principle of bolometric detection. 'Bolometric' refers to the measurement of radiation. We distinguish between the bolometer, which measures radiation flux (e.g. infrared) and the microcalorimeter, which measures the energy of individual radiation quanta (e.g. X-rays). In a conventional bolometer or microcalorimeter, an absorber with heat capacity C is kept at a certain temperature T_0 by means of a connection to a heat bath by a thermal conductance G, as shown in figure 2.4. The behaviour of the temperature $T(t)$ after an energy E is absorbed is described by the power balance equation

$$C\frac{dT(t)}{dt} + G(T(t) - T_0) = E\delta(t), \tag{2.4}$$

which has the solution

$$T(t) = T_0 + \frac{E}{C}e^{-t/\tau}\vartheta(t) \tag{2.5}$$

where $\tau \equiv C/G$ is the thermal time constant of the system and $\vartheta(t)$ the Heaviside step function. The temperature excursion is proportional to the incident energy and can be
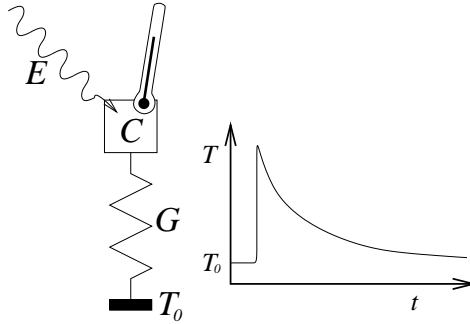
Figure 2.4: Schematic illustration of a conventional microcalorimeter. The absorber C is weakly coupled with a thermal conductance G to the bath, which is at a temperature T_0. After an event of energy E, the microcalorimeter temperature T behaves as shown in the graph on the right.

measured by a sensitive thermometer.

Although the transition edge thermometer is very sensitive, it has a very limited dynamic range. Operated as a current-biased bolometer, as described in e.g. [12], it requires a very well-controlled bath temperature. This limitation can be overcome by using voltage bias and a bath temperature well below T_c [13]. Joule heating ($P = V^2/R$) in the TES is used to raise the temperature to T_c, bringing the TES into its transition. With the operating temperature significantly above the bath temperature, the power flowing through the heat link to the bath is described by

$$P = K(T^n - T_b^n), \tag{2.6}$$

with T_b the temperature of the bath, K a material and geometry dependent parameter and n the power law exponent of the dominant mechanism responsible for the heat transport between thermometer and bath. For the heat transport to take place through phonon conduction, a value for n between 3 and 4 is expected, depending on whether specular or diffuse scattering occurs at the boundaries of the heat link material. For electron conduction in metals, the value is 2 and a heat link dominated by electron-phonon coupling has 5.

The power balance equation in the case of voltage bias, with the Joule heating term included, becomes:

$$C\frac{dT(t)}{dt} + K\left(T^n(t) - T_b^n\right) - \frac{V^2}{R(T(t))} = E\delta(t), \tag{2.7}$$

where the resistance function $R(T)$ describes the shape of the transition under bias conditions. In order to solve this equation analytically, we have to linearise it using these

first-order approximations:

$$K\left(T^n(t) - T_b^n\right) \approx P_0 + G(T(t) - T_0) \tag{2.8}$$

$$\frac{V^2}{R(T(t))} \approx P_0 - \frac{P_0\alpha}{T_0}(T(t) - T_0) \tag{2.9}$$

with

$$G \equiv \frac{dP}{dT} = nKT^{n-1} \tag{2.10}$$

the dynamic thermal conductance and

$$\alpha \equiv \frac{T}{R}\frac{dR}{dT} \tag{2.11}$$

a dimensionless characterisation of the steepness of the transition. In the first-order approximations above, the time-independent quantities P_0 and T_0 are the *equilibrium* values of power flowing to the bath and TES temperature, respectively. Using the approximations, we can write down the linearised equation:

$$C\frac{dT(t)}{dt} + G\left(1 + \frac{P_0\alpha}{GT_0}\right)(T(t) - T_0) = E\delta(t). \tag{2.12}$$

The solution is

$$T(t) = T_0 + \frac{E}{C}e^{-t/\tau_{\text{eff}}}\vartheta(t), \tag{2.13}$$

with the effective time constant

$$\tau_{\text{eff}} = \frac{C}{G(1 + L_0)}. \tag{2.14}$$

Here we have used the abbreviation

$$L_0 \equiv \frac{P_0\alpha}{GT_0} \tag{2.15}$$

$$= \frac{\alpha}{n}\left(1 - \left(\frac{T_b}{T_0}\right)^n\right). \tag{2.16}$$

The number L_0 is called the 'loop gain'. In the limit of extreme electro-thermal feedback ($T_0 \gg T_b$), we can approximate it by $L_0 \approx \alpha/n$. The time constant τ_{eff} is shortened, compared to the intrinsic time constant τ, by a factor $1 + L_0$ by means of *negative electro-thermal feedback* (ETF). This is the mechanism that drives the thermometer back to the same set point in the transition: A rise in temperature leads to an increase in resistance. This in turn decreases the current, which results in a decrease in Joule power. Because there is less power flowing into the thermometer, it cools down, compensating for the
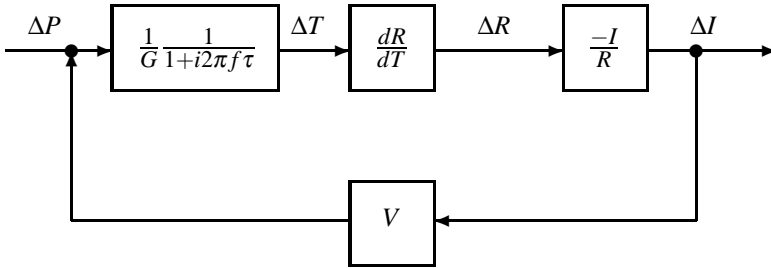
Figure 2.5: Schematic of the mechanism of negative electro-thermal feedback. In the boxes, the transfer functions between the various quantities are given. The thermal conductance forms a low-pass system with a time constant of $\tau = C/G$. Therefore, the transfer function from power to temperature is frequency-dependent.

original temperature rise. In this way, any temperature excursion is regulated back to the operating point by a change in Joule heating. This has the added advantage that the pulse decay time is shortened, allowing a higher count rate. A schematic of the feedback loop is shown in figure 2.5. The feedback diagram is very useful for understanding the response of the TES. For any feedback loop with a forward gain of A and a feedback gain of B, the total gain of the circuit is $A/(1-AB)$. In this way, the response of such a circuit can be easily calculated without having to solve differential equations. This principle is employed in the next section.

But before we go on, we will elaborate on the transition steepness parameter α. The TES resistance is a function of both temperature and current. The steepness of the resistance curve with respect to temperature $\partial R/\partial T$ can be measured using a small constant current while sweeping the temperature, as shown in figure 2.6 on the left. Conversely, the steepness with respect to current $\partial R/\partial I$ can be measured with the device well coupled to a constant temperature bath while sweeping the current. From these derivatives we can calculate $\alpha_T \equiv (T/R)(\partial R/\partial T)$ and $\alpha_I \equiv (I/R)(\partial R/\partial I)$.

Under bias conditions with a weak coupling to the bath, there will be a mixed situation: because of Joule heating, increasing the bias voltage will increase the temperature but also decrease the current. The system will move at an angle through the T-I-plane across the curve describing the transition, as shown in figure 2.6. On the right, the movement of the system through T-I-R space is shown for a change in the bias voltage. From the $I(V)$-curve that is measured in this way, an $R(T)$-curve can be calculated. This data can be used to determine the $\alpha \equiv (T/R)(\Delta R/\Delta T)$ under bias conditions at each set point, which will be smaller than α_T measured at low, constant current. The change in resistance due to a change in temperature and current is given by

$$\Delta R = \frac{R}{T}\alpha_T \Delta T + \frac{R}{I}\alpha_I \Delta I. \tag{2.17}$$
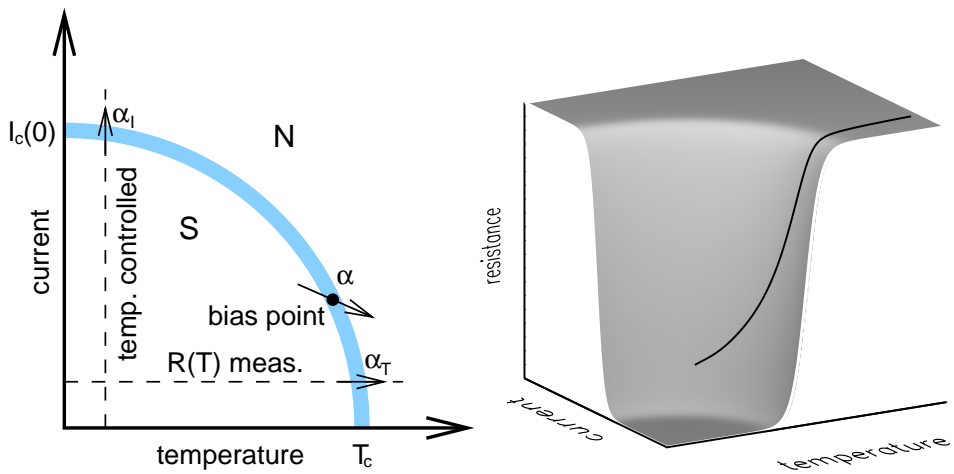
Figure 2.6: **Left**: The superconductive (S) and normal (N) regions of the transition edge thermometer in the plane of current and temperature. The dashed lines indicate an $R(T)$-measurement at constant current and an $R(I)$-measurement at constant temperature. The slanted arrow indicates the direction of movement through the transition under voltage bias conditions. **Right**: Cartoon of the resistance as a function of temperature and current. The curve indicates the position of the bias point as a function of bias voltage. The current component of the curve is very much exaggerated; in reality the typical bias current is much smaller than the critical current of the device.

Figure 2.7: Simplified version of the circuit diagram for operating a TES under voltage bias with current readout. A more complete version is given in figure 4.2. Here, a constant current I_b and a shunt resistor R_s are used to apply a constant voltage over the TES. The output is the current I through the TES.

If we substitute $\Delta I = (-I/R)\Delta R$ and do some rearrangement, we find the relation

$$\frac{T\Delta R}{R\Delta T} = \frac{\alpha_T}{1+\alpha_I}. \tag{2.18}$$

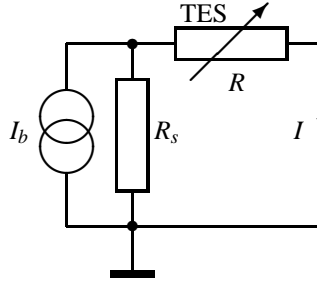The left-hand side is the definition of our 'effective' α under bias conditions. It is this effective α that should be substituted into the loop gain expression (2.16). Since this α is the one we can measure under bias conditions, we do not have to worry about the individual α_T and α_I. This will be slightly different when the voltage bias cannot be assumed to be ideal (see for instance [14]), but it remains a good approximation.

2.4 Noise model

Now that the principle of ETF has been explained, we can look at how it influences the noise and responsivity in the system. At the same time, we will extend the feedback diagram from the previous section to include a non-ideal voltage bias. Also, the noise sources that are predicted by theory are incorporated into the diagram. This will enable us to calculate the effect of the noise at the output of the system.

In practice, the voltage bias is implemented as a constant bias current I_b with a small shunt resistor R_s and the TES in parallel, as shown in figure 2.7. This scheme has an effect on the transfer functions from resistance to current and from current to power. These become:

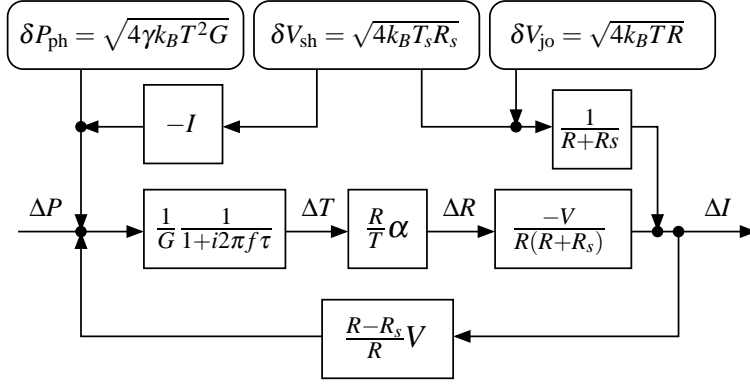$$\frac{dI}{dR} = \frac{-V}{R(R+R_s)} \tag{2.19}$$

Figure 2.8: Feedback diagram for signal conversion from input power to output current by a voltage-biased TES, with noise sources. Indicated at the top are spectral noise density values for phonon noise from the heat link to the bath (δP_{ph}), Johnson noise from the TES itself (δV_{jo}) and Johnson noise from the shunt resistor (δV_{sh}). The shunt noise enters the diagram in two locations to compensate for the fact that the shunt is not part of the thermal circuit. The advantage of this type of feedback diagram is that it is appropiate for many types of noise sources that enter the diagram in a natural way. After [15].

$$\frac{dP}{dI} = \frac{R - R_s}{R} V \tag{2.20}$$

In figure 2.8, the extended feedback diagram is shown, with the most important noise sources included. These are:

Phonon noise originating from the thermal fluctuations over the heat link to the bath. The spectral noise density is given by

$$\delta P_{\mathrm{ph}} = \sqrt{4 \gamma k_B T^2 G}, \tag{2.21}$$

with

$$\gamma \approx \frac{n}{2n + 1}, \tag{2.22}$$

a factor of ~ 0.5. This factor accounts for the fact that there is a temperature gradient over this heat link [16]. Because of the gradient, the magnitude of the noise is based on a temperature that lies between T_b and T. Phonon noise enters the system at the same location as the signal, at the input of the feedback diagram.

Johnson noise originating from random transport of charge over the TES resistor. The spectral noise density is

$$\delta V_{\mathrm{jo}} = \sqrt{4 k_B T R}. \tag{2.23}$$

This noise component is first converted to current and then enters the feedback circuit at the output.

Shunt noise, that is Johnson noise from fluctuations over the shunt resistor. The spectral noise density is

$$\delta V_{\text{sh}} = \sqrt{4k_B T_s R_s}, \tag{2.24}$$

with T_s the temperature of the shunt resistor, which is preferably at the bath temperature. This noise component enters the feedback circuit at the same location as Johnson noise from the TES. However, the shunt resistor is not part of the thermal circuit, so the power dissipated in that resistor by the Johnson noise should not be included in the feedback system. To correct the diagram for this, the dissipated power is subtracted from the thermal noise by means of an extra branch.

At the output, with the feedback taken into account, these three noise components will be observed as

$$i_{\text{ph}}(f) \quad = \quad \sqrt{4\gamma k_B T^2 G} \frac{\alpha I}{GT} \frac{R}{R+R_s} \frac{1}{1+\beta L_0} \frac{1}{\sqrt{1+4\pi^2 f^2 \tau_{\text{eff}}^2}} \tag{2.25}$$

$$i_{\text{jo}}(f) \quad = \quad \frac{\sqrt{4k_B T R}}{R+R_s} \frac{1}{1+\beta L_0} \sqrt{\frac{1+4\pi^2 f^2 \tau^2}{1+4\pi^2 f^2 \tau_{\text{eff}}^2}} \tag{2.26}$$

$$i_{\text{sh}}(f) \quad = \quad \frac{\sqrt{4k_B T_s R_s}}{R+R_s} \frac{1}{1+\beta L_0} \sqrt{\frac{(1-L_0)^2+4\pi^2 f^2 \tau^2}{1+4\pi^2 f^2 \tau_{\text{eff}}^2}} \tag{2.27}$$

with

$$\beta = \frac{R-R_s}{R+R_s} \tag{2.28}$$

and

$$\tau_{\text{eff}} = \frac{\tau}{1+\beta L_0}. \tag{2.29}$$

From the diagram, the total small-signal responsivity $S \equiv |\Delta I/\Delta P|$ is found to be

$$S(f) = \frac{\alpha I}{GT} \frac{R}{R+R_s} \frac{1}{1+\beta L_0} \frac{1}{\sqrt{1+4\pi^2 \tau_{\text{eff}}^2 f^2}}. \tag{2.30}$$

It should be noted that this expression is only valid for small signals. In section 6.5.2, a procedure for calculating the large-signal responsivity is presented. Using expression (2.30), the noise components can be transformed back to the input and the noise equivalent power (NEP$\equiv i_{\text{noise}}/S$) can be calculated:

$$\text{NEP}_{\text{ph}} \quad = \quad \sqrt{4\gamma k_B T^2 G} \tag{2.31}$$

$$\text{NEP}_{\text{jo}}(f) = \sqrt{4k_B T R \frac{GT}{V\alpha}} \sqrt{1 + 4\pi^2 f^2 \tau^2} \tag{2.32}$$

$$\text{NEP}_{\text{sh}}(f) = \sqrt{4k_B T_s R_s \frac{GT}{V\alpha}} \sqrt{(1-L_0)^2 + 4\pi^2 f^2 \tau^2} \tag{2.33}$$

The total NEP is simply the square root of these components added quadratically.

2.5 Energy resolution prediction

Using the NEP calculated in the previous section, we can find an expression for the theoretical energy resolution. To do so, we look at the signal transformed back to the input, that is as a power. When we look at the signal in the frequency domain, we assume that the amplitude in each frequency bin is an independent estimate of the original photon energy [12]. The best way to reconstruct this energy is to take a weighted average (integral) over all these frequency bins. The uncertainty in determining the power at a certain frequency is given by the NEP. Therefore, the weighting factor at frequency f is $1/\text{NEP}^2(f)$. The weighted average is given by

$$E_w = \frac{\int_0^\infty \overline{P}_{\text{in}}(f)/\text{NEP}^2(f)df}{\int_0^\infty 1/\text{NEP}^2(f)df}, \tag{2.34}$$

where $\overline{P}_{\text{in}}(f)$ is the input signal in the (single-sided) frequency domain. The RMS uncertainty in the weighted average is given by

$$\sqrt{\langle \Delta E_w^2 \rangle} = \sqrt{\frac{1}{\int_0^\infty 1/\text{NEP}^2(f)df}}. \tag{2.35}$$

We would like to know how accurate we can determine the original photon energy E. To get that number, we need to scale $\sqrt{\langle \Delta E_w^2 \rangle}$ with a factor E/E_w, so we need to evaluate (2.34). The input signal is modelled as a δ-pulse in the time domain: $P_{\text{in}}(t) = E\delta(t)$. Its Fourier transform is E, but because we work in the single-sided frequency domain (which means we only use positive frequencies), we must use the expression

$$\overline{P}_{\text{in}}(f) = 2E. \tag{2.36}$$

From (2.34), we see that $E/E_w = 1/2$. Therefore, we can write for the FWHM uncertainty in the original energy E:

$$\Delta E = 2.35 \frac{1}{\sqrt{\int_0^\infty \frac{4df}{\text{NEP}^2(f)}}} \tag{2.37}$$

In practice, the weighted integral should be accomplished by some sort of filtering. In appendix B we will describe our filter implementation.

Substituting for the NEP the quadratic sum of the theoretical expressions of the noise sources from the previous section and applying the approximation for extreme electro-thermal feedback ($n \approx P/GT$), we may write

$$\Delta E_{\text{theor}} = 2.35 \xi \sqrt{k_{\text{B}} T^2 C} \qquad (2.38)$$

with

$$\xi \quad = \quad \frac{2}{\alpha} \sqrt[4]{(\gamma n \alpha^2 + \alpha^2)q + (n^2 - \alpha^2)q^2} \qquad (2.39)$$

$$\approx \quad \frac{2}{\alpha} \sqrt[4]{\gamma n \alpha^2 + n^2} \qquad (2.40)$$

and

$$q = 1 + \frac{T_s R_s}{TR}, \qquad (2.41)$$

a factor very close to 1. Note that the parameter β is not present in this expression; the resolution is independent of the quality of the bias voltage. Equation (2.38) is an upper limit for the energy resolving power obtainable with a voltage biased TES-based bolometer or microcalorimeter. It is clear that there is a strong dependence on operating temperature, heat capacity and thermometer sensitivity, so those are the quantities to optimise.

CHAPTER 3

TES-BASED X-RAY MICROCALORIMETER

In this chapter, we will look at the parameters involved in designing an actual TES-based X-ray microcalorimeter. We will describe the requirements for the absorber and the coupling to the bath. Following the specifications for the NFI2 instrument on the XEUS satellite [17], we will determine some relevant parameters.

The basic properties we should aim for in a practical sensor are as follows:

- large filling factor;

- high efficiency;

- high count rate capability;

- good energy resolution (low noise).

These properties will be explained below.

Large filling factor   For imaging purposes, in which case a large number of detector elements are used side by side, it is desirable to have as small a gap as possible between the detectors. In other words: a high filling factor. The XEUS specifications quote a number of at least 95%. For this reason, we would like the absorbing area to cover the whole of the detector size, with no parts like wiring sticking out.

High efficiency   Since the intended applications include sources of low brightness, a high absorbing efficiency is important. Also, a high efficiency of the absorber reduces the effect of confusion of the spectrum due to unintentional absorption in other parts of the sensor. The XEUS specification is an absorption efficiency of at least 90% at 6 keV, as would be provided e.g. by 5 μm Bi, as shown in figure 3.1 [18].
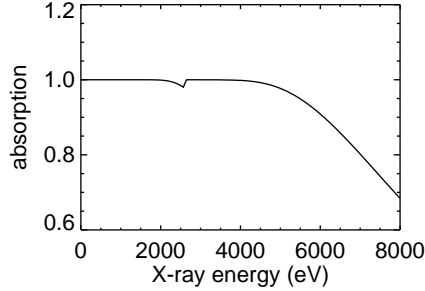
Figure 3.1: Absorption of 5 μm Bi as a function of X-ray energy. From data in [18].

High count rate capability   Although count rate is not a big issue for the intended application, less pile-up can be benficial to the resolution. For the XEUS specification of 100 counts per second per pixel, a pulse fall time of ~ 100 μs is appropiate.

Good energy resolution   In order to resolve weak, narrow spectral lines to a good line/continuum ratio, energy resolution is very important. The XEUS specification lists 2 eV FWHM at 1 keV and 5 eV at 7 keV. In a well-designed sensor and read-out system, the main limitation for the energy resolution is intrinsic noise. To get the best signal-to-noise ratio, the ideal design should have a high α, a low operating temperature and a low heat capacity.

3.1   Absorber and heat capacity

The function of the absorber is to convert the energy of an absorbed photon into heat. This heat then spreads out and raises the temperature of the absorber, which is measured by the thermometer. The choice of absorber materials and dimensions determine the absorption efficiency, detection area and dynamic range of the sensor and also the energy resolution, as we shall see. The absorption probability of X-ray photons in a material is given by

$$A = 1 - e^{-n\mu_a d} \tag{3.1}$$

with n the number of atoms per unit volume, μ_a the linear atomic photoabsorption cross-section and d the thickness. These parameters can be found in [18] for many elements and energies. For a few metals and a photon energy of 6 keV, they are copied in table 3.1.

Since the energy resolution deteriorates with increasing heat capacity, a material that combines high X-ray absorption efficiency with low heat capacity is best. The specific

Table 3.1: Parameters of importance for absorber material selection for some metals: absorption cross-section, atomic concentration, specific heat and the figure of merit for absorber material selection. (S) means superconductor, (N) means normal metal. From [18] and [19].

Element	μ_a @ 6 keV (10^{-24}m^2)	n $(10^{28}/\text{m}^3)$	c_V @ 0.1 K (J/K/m^3)	$n\mu_a/c_V$ $(10^{-21}\text{K m}^2/\text{J})$
Mo (S)	5.3	6.4	0.0023	15
Ti (S)	3.6	5.7	0.0025	8.2
Ta (S)	10	5.6	0.013	4.3
Sn (S)	13	2.9	0.012	3.3
Nb (S)	4.8	5.6	0.0086	3.1
Bi (N)	17	2.8	0.037	1.3
Al (S)	0.49	6.0	0.0025	1.2
Pb (S)	16	3.3	0.092	0.59
Au (N)	14	5.9	7.1	0.012
Ag (N)	8.2	5.9	6.3	0.0076
Cu (N)	1.2	8.5	9.8	0.0010

heat of normal metals at temperatures below 1 K is dominated by the electronic specific heat, given by

$$c_V^{\text{el}} = \frac{n\gamma T}{N_A},$$ (3.2)

where N_A is Avogadro's number and γ is the Sommerfeld parameter, a characteristic of the material, in $\text{J/K}^2/\text{mol}$ [19].

For superconductors below their T_c, the specific heat is dominated by the phonon specific heat. This is given by the Debye T^3 law:

$$c_V^{\text{ph}} = \frac{12\pi^4}{5} n k_B \left(\frac{T}{\Theta}\right)^3$$ (3.3)

where Θ is the Debye temperature which can also be found in [19]. For a few metals, data for electron (in the case of normal metals) and phonon heat capacity (for superconductors) are given in table 3.1. To make the trade-off between absorption efficiency and specific heat, we can define a figure of merit:

$$\lim_{d \to 0} \frac{A}{dc_V} = \frac{n\mu_a}{c_V}$$ (3.4)

Values for this figure of merit are given in table 3.1 (higher is better). Based on the figure of merit, we see that superconducting absorbers might be a good choice. However, in a

superconductor, part of the energy of an absorbed photon is used to break up Cooper pairs, creating quasiparticles. These need to recombine to produce phonons which can enter the thermometer. The time needed for this recombination may be very long due to trapping of the quasiparticles in the superconductor. The effect of this on the pulse shape is not well known. For reasons of simplicity, it might be preferable to stick to normal metals. Of these, the semi-metal Bi is the best. However, Bi has a low thermal conductivity. For fast thermalisation of the photon energy, a high thermal conductivity of the absorber material is also important. Therefore, a combination with a normal metal like Au, Ag or Cu is preferable. Thanks to the low specific heat of Bi there is some room left for a normal metal.

Given a requirement for absorption efficiency and a choice for the material or materials, the minimum thickness is fixed. The remaining free parameter then is the absorber area D. Bigger is nicer of course, but increases the heat capacity. There is a clear trade-off between detection area and energy resolution.

A last important item to consider is the dynamic energy range of the detector. The maximum photon energy E_{max} of the radiation to be measured and the allowable temperature change ΔT_{max} are directly related to the heat capacity:

$$C = \frac{E_{max}}{\Delta T_{max}} \tag{3.5}$$

If the operating range ΔR_{max} should remain within 10%–90% of the normal resistance R_n, the temperature range of the thermometer becomes

$$\Delta T_{max} = \frac{\langle T \rangle \Delta R_{max}}{\langle R \rangle \alpha} \tag{3.6}$$

$$= 1.6 \frac{T_c}{\alpha} \tag{3.7}$$

with the average values $\langle T \rangle = T_c$ and $\langle R \rangle = 0.5 R_n$. So, for a given dynamic range, we have for the minimum heat capacity.

$$C = 0.63 \frac{\alpha E_{max}}{T_c}. \tag{3.8}$$

Since the energy resolution depends on the heat capacity, there is also a clear trade-off between dynamic range and resolution of the sensor.

In this discussion, we have not yet included the heat capacity of the TES. Although it is generally small compared to the absorber heat capacity, it adds to the total heat capacity:

$$C = D d c_V + C_{TES} \tag{3.9}$$

We could now imagine a surface of equal heat capacity in a three-dimensional parameter space with the dimensions of absorption efficiency, detection area and dynamic range

(A-D-$E_{\max}$ space). This surface is described by the equation

$$D\frac{-\ln(1-A)}{n\mu_a}c_V + C_{\text{TES}} = 0.63\frac{\alpha E_{\max}}{T_c}. \tag{3.10}$$

The parameters can now be optimised through an interative process. The most practical approach is to start by fixing two parameters to preferred values and computing the third. Next, adjustments can be made to one or both of the input parameters until the specifications are reached.

3.2 Cooling and thermal conductance

After the heat capacity, another important design parameter is the coupling to the bath. In this section, we will derive upper and lower limits for the conductance of the heat link. The suitable magnitude of the cooling power and therefore the thermal conductance to the bath is dictated by the specified effective pulse fall time constant τ_{eff}. Due to electro-thermal feedback, the dynamic thermal conductance to the bath in the case of ideal voltage bias ($\beta = 1$) is given by

$$G = \frac{C}{\tau_{\text{eff}}(1 + L_0)} \tag{3.11}$$

$$\approx \frac{C}{\tau_{\text{eff}}(1 + \alpha/n)}. \tag{3.12}$$

So, given a maximum pulse fall time constant, we have with (3.12) an expression for the minimum thermal conductance. Since the resolution is independent of G, it might seem advantageous to use a higher value in order to get faster pulses. However, the need for electro-thermal stability imposes an upper limit to the allowable thermal conductivity [20]. In addition to the pulse fall time, there is another time constant in the system: the electrical time constant $\tau_{\text{elec}} = L/R$, with R the resistance and L the induction in the circuit. The ratio of these time constants determines the stability of the system. The condition for stability can be found by looking at a pole/zero diagram of the circuit impedance, as sketched in figure 3.2. The zeroes in the complex impedance describe a circular track in the complex plane. When they are located in the left half of the complex plane, oscillations caused by instabilities in the system are damped. In order to attain this, the (effective) thermal time constant and the electrical time constant should not be too close together. For the system to be critically damped, we have

$$\frac{\tau_{\text{eff}}}{\tau_{\text{elec}}} = 5.8. \tag{3.13}$$

For a sub-critically damped system, it is [21]

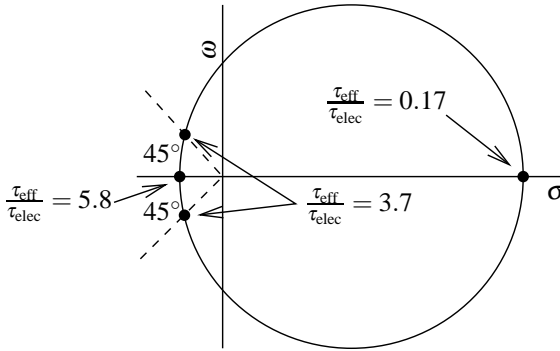$$\frac{\tau_{\text{eff}}}{\tau_{\text{elec}}} = 3.7. \tag{3.14}$$

Figure 3.2: Sketch of the position in the complex plane of the zeroes of the impedance $Z(\sigma + i\omega)$ of the TES bias circuit for different values of $\tau_{\mathrm{eff}}/\tau_{\mathrm{elec}}$. The dashed lines indicate the boundary of the area in which oscillations in the system are sub-critically damped. After [21].

We use the latter case, which is the lower limit for the $\tau_{\mathrm{eff}}/\tau_{\mathrm{elec}}$ ratio for stable operation of the circuit. The inductance L is determined by the inductance of the wiring and other components, such as a SQUID input coil, and is considered given. The upper limit for the thermal conductance is now given by

$$G < \frac{CR}{3.7L(1+\alpha/n)} \tag{3.15}$$

Thus, for a given set of parameters n, α, C, τ_{eff}, R and L the range of allowable values of G is fixed. The thermal conductance is often provided by a silicon nitride membrane onto which the microcalorimeter is positioned. The G can then be tuned by varying the thickness, shape and size of the membrane. For a circular membrane with thickness d, radius r_m, thermal conductivity κ and the microcalorimeter in the centre, the radial temperature gradient at a distance r from the centre is given by

$$\frac{dT(r)}{dr} = \frac{-P}{2\pi r d\kappa}. \tag{3.16}$$

Assuming as a boundary condition that $T(r_m) = T_b$, the solution for the temperature dependence is

$$T(r) = \frac{-P\ln(r/r_m)}{2\pi d\kappa} + T_b. \tag{3.17}$$

The singularity at $r = 0$ can be solved by realising that the temperature around the centre is kept constant by the presence of the microcalorimeter, up to its radius r_μ. At that point

$r = r_\mu$ we have

$$P = \frac{-2\pi d\kappa}{\ln(r_\mu/r_m)}(T - T_b). \tag{3.18}$$

Taking the derivative with respect to T, we find

$$G = \frac{-2\pi d\kappa}{\ln(r_\mu/r_m)}. \tag{3.19}$$

With this equation, we can determine the dimensions of a membrane that provides the desired G. It is valid for round membranes, but also a fair approximation for square membranes with a side of $2r_m$. For silicon nitride, values for the thermal conductivity κ have been measured to be $15T^{2.0} \times 10^{-3}$ W/m/K [22] or $8T^{2.2} \times 10^{-3}$ W/m/K [23]. The difference between these two measurements is probably caused by a different ratio of diffuse and specular scattering at the surface due to differences in thickness (200 nm and 1 μm, respectively) and roughness.

3.3 Practical sensor

Using the relations developed above, we can find the parameters for the ideal sensor for our application. SRON has developed superconducting Ti/Au bilayers with a transition temperature of $T_c \approx 0.1$ K. With a practical bath temperature of $T_b \approx 0.01$ K, the approximation for the loop gain in section 2.3 is valid for these films. In the normal state, these films have a square resistance of $R_n \approx 0.20$ Ω. Under bias conditions, the typical α of the bilayers is about 50. Assuming a maximum photon energy range of 10 keV[1], we find through (3.8) a minimum heat capacity of 0.50 pJ/K. The theoretical resolution, according to (2.38), is then ~ 1.2 eV FWHM.

From (3.12) and the XEUS specification we get a minimum thermal conductance of 0.28 nW/K. In our setup, the inductance of the SQUID and wiring is fixed at about 0.5 μH. A typical set point resistance is $0.1R_n = 0.02$ Ω, giving a τ_{elec} of 25 μs. According to (3.15), this limits G to 0.31 nW/K for a sub-critically damped system. The range between minimum and maximum G is in fact very small. With careful design of the wiring, it should be possible to lower the parasitic inductance and allow for faster signals. For a given membrane, G can be determined by measuring the bias power needed to heat the sensor to the transition temperature as a function of bath temperature. By fitting (2.6) to these measurements, n and K are found, from which G is calculated through (2.10). For the devices discussed in this thesis, a 3 mm $\times$ 3 mm $\times$ 1 μm Si$_3$N$_4$ membrane was used, as shown in figure 3.3, with $n = 3.2$ and $K = 1.5 \times 10^{-8}$ W/K^n. From these

---

[1]Although the XEUS specifications state a maximum energy of 15 keV, they do not require the best energy resolution to be obtained at those high energies. Therefore we can permit some saturation of the microcalorimeter at the highest energies and use a smaller maximum photon energy for the calculation here.
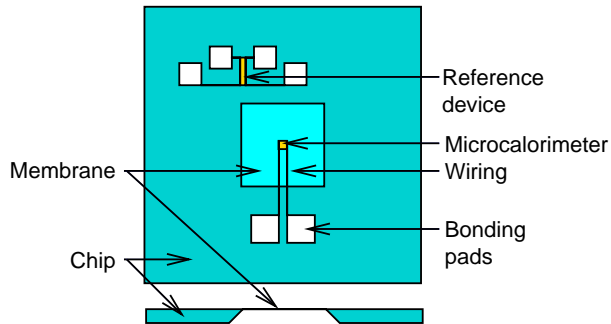
Figure 3.3: Schematic drawing (top and cross-section view) of the chip layout. The dimensions of the chip are 11×11 mm. The sensor under study is on the membrane in the centre. To allow for an independent check of the quality of the transition, a reference TES is processed on the chip.

numbers, a thermal conductivity of $\kappa = 12T^{2.2} \times 10^{-3}$ W/m/K is calculated. At 0.1 K, $G = 0.30$ nW/K.

With the values for heat capacity and membrane size known, the sensor can be fabricated. The fabrication of the sensors and the test setup are the subject of the next chapter.

CHAPTER 4

FABRICATION AND SET-UP

This chapter deals with the technical requirements for fabricating and testing the TES X-ray microcalorimeters. We will have a brief look at the critical issues involved in the lithographic process. Then, we will discuss the requirements for the test set-up and data processing.

4.1 Lithography

The sensors discussed in this thesis are fabricated in a cleanroom using SRON expertise and standard photolithographic techniques. We will not describe those here in detail, but instead have a brief look at the aspects of the process that are of specific relevance to the production of these sensors.

A complete sensor, such as shown schematically in figure 3.3, consists of a substrate, a TES, an absorber and electrical wiring. For the substrate, a 500 μm thick Si wafer is used with a 1 μm thick layer of Si_3N_4 on top that will form the membrane later on (step 1 in figure 4.1). At the location of the membrane, the Si is partially or completely etched away (step 2). Then, the Ti/Au bilayer is applied by means of e-beam evaporation. For a reproducible transition, a good interface between the two layers is necessary. It is therefore important that the two layers are deposited in quick succession. There should also be little interdiffusion between the two layers. When the temperature exceeds $\sim$ 120°C, interdiffusion starts to occur. Therefore, it is critical that the temperature does not become too high during the deposition. This can be a problem at the location of the membranes in the wafer, where the thermal conductance is limited. Two approaches have been applied to this problem. The first is to not etch away all the Si at the location of the membrane until the sensor is finished. However, etching the Si from underneath a completed sensor can be risky. The etchant may damage the sensor or wiring. The alternative route is to etch away all the Si before the bilayer deposition, and apply a 1 μm
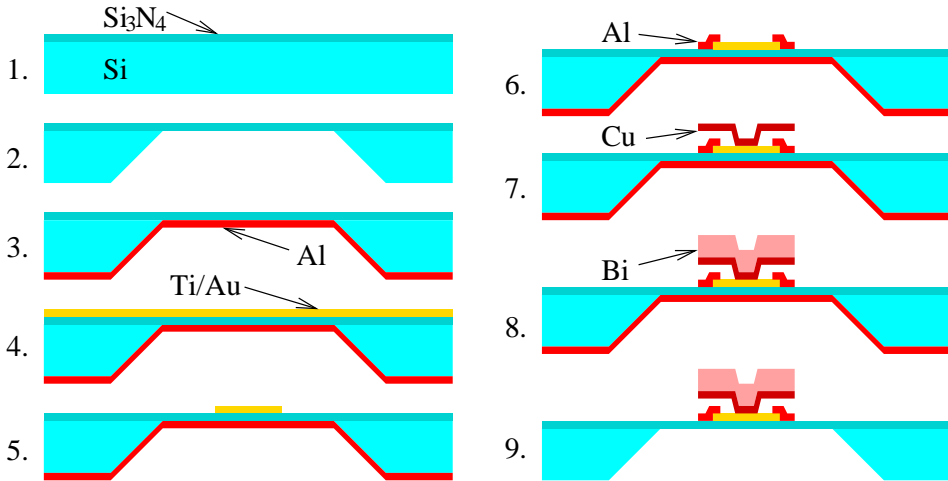
Figure 4.1: Schematic illustration of the fabrication process for a single-pixel TES micro-calorimeter (cross-section, not to scale). An explanation of the fabrication steps is given in the text.

thick Al or Cu cooling layer to the bottom of the wafer using sputter deposition (step 3). This provides the necessary conduction of heat away from the membrane and can be easily etched away when the sensor is finished. In this way, the temperature does not exceed $\sim 40°$C during deposition.

After the bilayer deposition (step 4), the wafer is diced into chips which are processed individually. The bilayer is patterned into a thermometer at the centre of the membrane and a reference device towards the edge (step 5). Then, a resist pattern is laid out for the Al wiring and bonding pads, which are applied using sputter deposition (step 6). As shown in figure 3.3, the reference device has two connections on either side to enable a four-point resistance measurement; the sensor has just one connection on either side.

Subsequently, the resist pattern for the absorber is laid out. If an overhanging absorber is to be produced (see section 5.2), a two-step process is used to create the mold for the mushroom shape. Two resist layers are used with a 150 nm Al or Cu separation layer in between to avoid double exposure of the bottom layer. The 'hat' of the absorber is patterned in the top resist layer. Then, the separation layer is etched away. For this step, it is important to protect the cooling layer on the back side of the membrane with resist, if present. Next, the base of the absorber is patterned in the second resist layer. Then the Cu part of the absorber is added by means of sputtering (step 7). If desired, a Bi layer is applied on top of the Cu using thermal evaporation (step 8).

Finally, the cooling layer or alternatively the remaining Si under the membrane is

etched away (step 9) and the sensor is completed. The backside of the chip is coated with a thin layer of vacuum grease and mounted on a Cu mounting plate with phosphor-bronze springs. The contacts are wire-bonded to a circuit board, to which electrical leads can be soldered.

The group at NIST has observed wide transitions in their Mo/Cu TESes [24]. This was attributed to imperfections along the edges of the devices. They solved this problem by creating well-defined edges by depositing normal metal strips along the edges. In the devices manufactured at SRON, no such edge effects were observed, and no normal metal strips were necessary to obtain steep transitions.

4.2 Cooling, bias and read-out

After the production process of the sensor is completed, it has to be incorporated in a proper test setup. This involves cooling the sensor, applying a voltage bias and reading out the current through the device. In this section, the requirements for the experimental setup are described.

4.2.1 Thermal requirements

For the electro-thermal feedback to function properly, the sensor should be cooled significantly below the transition temperature. For our 100 mK sensors, a bath temperature ≤ 20 mK is preferred. A dilution refrigerator or adiabatic demagnetisation refrigerator may be used for this purpose. At SRON, we use a Kelvinox 100 dilution refrigerator from Oxford Instruments, which provides ample cooling power. The necessary cooling power at the lowest temperature stage is limited to the power dissipated in the sensor and (mainly) the shunt resistor, typically a nanowatt or less. At a higher temperature stage (~ 2 K), there is the power dissipated by the SQUID, typically ~ 0.1 μW. These demands are not very challenging, but the bath temperature stability may be. Drift in the bath temperature T_b leads to gain drift through the responsivity S. If the drift is not adequately compensated, the measured spectrum will be smeared and the resolution degraded. When the bath temperature changes, the system shifts to another equilibrium set point. This changes a number of factors in the responsivity (2.30): current, resistance, temperature, α and thermal conductance are all set point-dependent. Of these, the changes in current, resistance and perhaps α are the most important. We will see how a change in bath temperature will affect the responsivity. A set point in the transition is characterised by its resistance, so we need to know how this parameter changes. From the feedback diagram in figure 2.8, we see that a change in resistance due to a change in power is given by

$$\frac{\Delta R}{R} = \frac{\alpha}{GT} \frac{1}{1 + \beta L_0} \Delta P.$$

(4.1)

This change of power caused by a change in bath temperature can be derived from (2.6):

$$\Delta P = \frac{dP}{dT_b}\Delta T_b = -nKT_b^{n-1}\Delta T_b \tag{4.2}$$

We now take the derivative of the responsivity $S = S(f = 0)$ with respect to R, see (2.30). We use the expression with $f = 0$ because we are interested in the change in pulse area. Keeping in mind the definitions of α, β and L_0, and assuming a constant slope of the $R(T)$-curve, we obtain

$$\frac{R}{S}\frac{dS}{dR} = -\frac{2R + R_s + L_0 R_s}{R + R_s}\frac{1}{1 + \beta L_0}. \tag{4.3}$$

For the relative change in responsivity we can then write

$$\begin{aligned}
\frac{\Delta S}{S} &= \frac{R}{S}\frac{dS}{dR} \times \frac{\Delta R}{R} \tag{4.4}\\
&= \frac{2R + R_s + L_0 R_s}{R + R_s}\frac{\alpha}{GT}\frac{1}{(1 + \beta L_0)^2}nKT_b^n\frac{\Delta T_b}{T_b}. \tag{4.5}
\end{aligned}$$

Using the numbers from section 3.3 and a value for R_s of 7 mΩ, we see that for a stability given by a maximum $\Delta S/S$ of 1/6000 (1 eV at the energy of the Mn Kα line, a widely used X-ray test line), the bath temperature drift ΔT_b should stay below 0.66 mK over the measurement period. For shorter exposure times, this requirement is met in our dilution refrigerator without temperature control. In 30 minutes, the peak-to-peak value of the bath temperature is only ~ 0.15 mK. For longer measurement times (hours), active temperature control may be necessary.

In principle, bath temperature fluctuations will also contribute to the current noise. However, since the time constant of the bath is generally much longer than that of the pulses due to the large mass of the cooler, this will have no effect on the energy resolution.

4.2.2 Electrical requirements

In this section we will examine the electrical requirements for operating the TES microcalorimeter with good energy resolution. These include a stable bias voltage, a low-noise readout and an environment with low electromagnetic radiation.

Voltage bias   A simplified schematic for the bias and read-out electronics is given in figure 4.2. The voltage bias is obtained by dividing a constant voltage V_b of the order of tens of mV by a wiring and filter resistance R_w of 130 Ω and a shunt resistor R_s of 7 mΩ. Fluctuations on the bias voltage can influence the energy resolution in two ways: through the responsivity and through the noise.
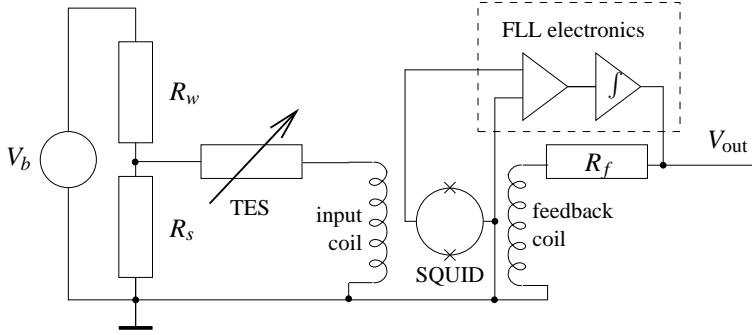
Figure 4.2: The read-out electronics for a TES microcalorimeter. The TES is voltage-biased through the wiring resistance R_w and the shunt resistor R_s. The current through the TES is converted to a magnetic field by the input coil and this is measured by the SQUID magnetometer. The flux-locked loop (FLL) electronics control the current through the feedback coil via the feedback resistor R_f so that the flux in the SQUID remains constant. The required feedback voltage V_{out} is proportional to the TES current and can be further amplified using room-temperature electronics.

First we will look at how drift in the bias voltage can cause gain drift. A fluctuation in the voltage over the TES will have two important effects on the responsivity (2.30): The expression is inversely proportional to the voltage, but it also contains the resistance, which depends on the set point and therefore on the voltage. Since the power flowing to the bath is constant for small set point changes, we can write

$$\frac{\Delta R}{R} = 2\frac{\Delta V}{V}. \tag{4.6}$$

The relative effect on the responsivity is the sum of the contributions from the voltage and the resistance effect:

$$\begin{aligned} \frac{\Delta S}{S} &= -\frac{\Delta V}{V} + \frac{R}{S}\frac{dS}{dR} \times \frac{\Delta R}{R} \tag{4.7} \\ &= -\left(1 + 2\frac{2R + R_s + L_0 R_s}{R + R_s}\frac{1}{1 + \beta L_0}\right)\frac{\Delta V}{V} \tag{4.8} \end{aligned}$$

Hence, using again the values from section 3.3, for a responsivity stability of 1/6000, the stability of the bias source over the course of the measurement needs to be better than 1/14000. This can be achieved using a stable voltage supply.

Noise on the bias supply can influence the current noise in the TES. We can model the

noise from the bias generator as white up to a cut-off frequency f_V:

$$\langle V_b^2(f)\rangle = \delta V_b^2 \frac{1}{1+f^2/f_V^2} \tag{4.9}$$

where δV_b is the spectral density of the noise from the voltage generator. Noise on the TES voltage couples into the circuit the same way as Johnson noise from the shunt resistor (see the diagram in figure 2.8), so the contribution to the NEP is

$$
\begin{aligned}
\mathrm{NEP}_V(f) &= \delta V_b \frac{dV}{dV_b} \frac{GT}{V\alpha} \sqrt{\frac{(1-L_0)^2 + 4\pi^2 f^2 \tau^2}{1+f^2/f_V^2}} \tag{4.10} \\
&= \delta V_b \frac{RR_sGT}{(R+R_s)R_wV\alpha} \sqrt{\frac{(1-L_0)^2 + 4\pi^2 f^2 \tau^2}{1+f^2/f_V^2}} \tag{4.11}
\end{aligned}
$$

This can be made very small by using a low-pass filter with a very low cut-off frequency f_V in the bias line. In this way, the contribution to the energy resolution was made negligible.

(Electro)magnetic susceptibility   Susceptibility to electromagnetic radiation and magnetic fields may cause the sensor to behave differently than expected. Therefore, the samples are mounted in the cryostat inside a superconducting Al canister which provides good shielding from these effects. The wires going into the canister pass through filters, shielding the inside from high-frequency noise.

Read-out   The combination of SQUID, input coil and feedback circuit provides a very accurate current amplifier. In order not to deteriorate the energy resolution, its noise should of course be significantly lower than the TES noise, in our case ~ 5 pA/$\sqrt{\mathrm{Hz}}$. Depending on the value of the feedback resistor R_f and the ratio between the number of turns of the input and feedback coils (in our case 1 kΩ and 1:8, respectively), the desired noise level at the output of the SQUID will be in the order of 10 nV/$\sqrt{\mathrm{Hz}}$. We have used such a SQUID made available by the University of Colorado at Denver.

Data-acquisition   For further processing (filtering), the signal may be sampled using a digital system. To avoid ground loops, we have used an optocoupler to galvanically separate the computer from the SQUID electronics. For the data acquisition, it is important to avoid aliasing (see also appendix B). This is done by using a low-pass anti-aliasing filter and sufficient oversampling. The cut-off frequency of the anti-aliasing filter should be chosen in such a way that the signal is not affected. The fastest part of the signal is the pulse rise time of ~ 10 μs. To be on the safe side, we should therefore use an anti-aliasing filter with a time constant of ~ 5 μs. We use a 2$^{\mathrm{nd}}$ order Butterworth filter. The filter
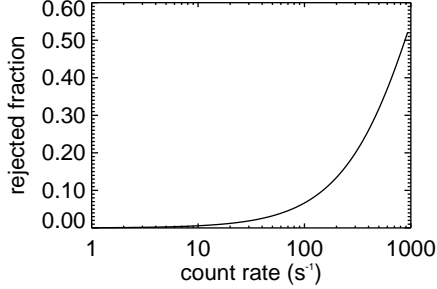
Figure 4.3: Fraction of rejected pulses due to pile-up rejection as a function of count rate for a 1 eV resolution contribution at 5.9 keV and a fall time of 100 μs, for pulses of equal energy.

does not have an infinitely steep cut-off, so in order to avoid any aliasing we need to leave some room between the filter cut-off frequency and the sampling frequency. Therefore, we need a sampling interval of ~ 1 μs. We would like to sample a pulse for a length of $\sim 10\tau_{\text{eff}}$, so for a 100 μs fall time, this means about 1000 samples/event. When the signal is integrated, this will reduce the quantisation noise by a factor $\sqrt{1000} = 32$. Since our average signal level for exponential pulses is $\int_0^{10} \exp(-x)dx/10 = 1/10$ of the maximum amplitude, for a 1 eV FWHM contribution at 6 keV we need $2.35 \times 10 \times 6000/32 \approx 4000$ quantisation levels, i.e. a 12-bit ADC board.

In addition to this sampling system, we use a pulse height analyser in combination with analog pulse shaping electronics as a quick-look facility. This enables a real-time look at a pulse height spectrum as it builds up. For measurement of $I(V)$-characteristics, a high-resolution (16-bit) ADC board is available.

Pile-up rejection Resolution degradation may arise through one pulse influencing the next. This is called pile-up. The implication of this effect on the energy resolution is calculated analytically in the appendix in section B.3.2. Resolution degradation through pile-up can be prevented by rejecting pulses that are too close to their precursor. In figure 4.3, the rejected fraction (dead time) is shown as a function of count rate for a 1 eV resolution contribution and a fall time of 100 μs. As can be seen from the figure, up to a few hundred counts per second, the dead time fraction is acceptable, but for higher count rates it deteriorates quickly.

Filtering The digital filtering that we have used is described in detail in appendix B. It basically consists of multiplying each pulse with an average pulse and integrating it.

Our implementation was tested using simulated pulses onto which artificial white noise was superimposed. In these simulations, the filter performed as expected. In appendix B, some causes of resolution degradation in filtering are examined. However, these effects are only responsible for a few percent in degradation of the theoretical value. Also, the fact that our filtering procedure incorrectly assumes a white noise distribution should not contribute significantly to the resolution degradation.

With the possible exception of the SQUID readout, these thermal and electrical requirements can be met using commercially available equipment and should therefore not be an obstacle for obtaining high spectral resolutions with these microcalorimeters.

To test the whole system of cooler, bias voltage generator, SQUID, amplifiers, opto-coupler, filters and data-acquisition system, a normal resistor (in this case, the TES in the normal state) can be hooked up in the circuit. A low-noise exponential pulse can then be superimposed on the bias voltage. The pulse is adjusted so that the amplitude and fall time on the output match the X-ray pulses. If the setup is sufficiently quiet, the resolution of the spectrum that is measured in this way should only be limited by the Johnson noise in the resistor. When we scaled the spectrum to 5.9 keV, we found a resolution of 1–2 eV FWHM. For a target resolution of 5 eV, we conclude that the measurement setup will have no significant contribution to the measured resolution.

CHAPTER 5

TOWARDS A XEUS PIXEL

In this chapter, we will look at the preformance of different sensor layouts in terms of energy resolution at 5.9 keV. A number of designs leading towards a XEUS-compatible pixel were investigated. Working from a simple square absorber, we developed a sensor with a mushroom-shaped overhanging Cu/Bi absorber for increased filling factor and absorption efficiency. The results will be described below.

For most experiments, a square TES with sides of 310 μm was used, consisting of a bilayer of 50 nm Au on top of 14 nm Ti. It should be noted that a superconductor just below its T_c has a specific heat of 2.43 times the electronic specific heat at that temperature. Using values for the specific heat from [19], we have for the heat capacity of the TES at 0.1 K $C_{\text{TES}} = 0.14$ pJ/K. Keeping in mind the total heat capacity of 0.50 pJ/K from section 3.3, this leaves for the absorber $C_{\text{abs}} = 0.36$ pJ/K. In the various absorber designs that will be considered, this heat capacity was kept constant to ensure comparable energy resolution and time constant.

5.1 Square absorber

To be able to contain an X-ray event, the sensor needs a certain minimum heat capacity. This can be attained by using a thick TES which combines the functions of absorber and thermometer, as is done by groups at NIST and GSFC. Since a high filling factor is desired, care must be taken to create room in the design for the electrical wiring. At NIST, an elevated sensor design with wiring running underneath is developed. At GSFC, people are working on creating vias through the wafer in order to have the wiring on the backside. SRON is working towards overhanging absorbers, which leave room for the wiring to run underneath. Therefore, the thermometer and the absorber are not combined but seperate. For a fast response of the sensor, a good thermal conductance of the absorber is necessary and it has to be well-coupled to the TES. This can be achieved by using a

normal metal absorber and ensuring that the electron systems of TES and absorber are in contact. However, with a normal metal absorber, the T_c of a thin TES will be suppressed in the contact area due to the proximity effect. Therefore, it is impractical to cover the whole TES with the absorber, since it would be entirely driven to normal resistivity. A solution to this problem is to cover only part of the TES with the absorber.

This was done with sensor X038, which consisted of a square TES with a square absorber on top with sides of about one third of those of the TES. For further details of this sensor, we refer to the table in appendix A. The calculated heat capacity of the total sensor is 0.59 pJ/K at 100 mK. Through (2.38), this yields a theoretical resolution based on the small-signal model of $\xi \times 4.2$ eV FWHM, where ξ depends on the value of α at a particular setpoint. This value can be experimentally determined: by sweeping the bias voltage, an $I(V)$-characteristic was measured. Note that for the voltage on the sensor, we have $V \approx R_s(V_b/R_w - I)$, with V_b the measured voltage at the bias input. From the $I(V)$-curve, a number of parameters can be calculated at each set point: $R = V/I$, $P = VI$, $T = (P/K + T_b^n)^{1/n}$, $G = nKT^{n-1}$ and $\alpha = (T/R)(dR/dT)$, as shown in figure 5.1. The derivative dR/dT is found by taking the average slope of the $R(T)$-curve (under bias conditions, as calculated from the $I(V)$-curve) over a very small bias voltage interval. Alternatively, we can use $\alpha = (GT/P)(I/V - dI/dV)/(I/V + dI/dV)$, where $GT/P \approx n$. This last approximation is less exact, but does not require knowledge of the parameters T_b or K.

It should be noted that the α plotted here describes the temperature sensitivity at each set point in an *equilibrium* situation. This is the case when the sensor passes through a range of set points as the result of a change in the bias voltage. However, when it passes through a range of set points due to a *thermal* effect, such as an X-ray event, it will no longer be in an equilibrium situation. At the same set point in terms of resistance, the current will be lower compared to the equilibrium situation. Since α depends on the TES current, the values of α that the sensor encounters will differ slightly from the ones plotted here.

Based on the α measured here, the theoretical resolution in a practical set point (lower part of the transition, ~ 1 μV) can be as good as 1.7 eV for $\alpha \sim 30$. How does this number compare with real measurements? Figure 5.2 shows an energy spectrum measured with this sensor biased at $V = 0.97$ μV with an exposure time of 51 minutes. The spectrum was obtained from digitized X-ray pulses which were digitally filtered using the 'optimum' filter as described in appendix B, which included base line restoration, timing correction and drift correction. The fitted resolution of 4.5 eV is fairly typical for this sensor. With shorter exposure times (5 minutes) resolutions down to 3.9 eV were measured. The observed fall time was ~ 80 μs. This is consistent with (2.14), since we find through (2.16) a loop gain of $L_0 = 20$ in this setpoint.

This design meets the XEUS requirements for fall time and resolution at 5.9 keV, though there are still a number of issues to be pursued:
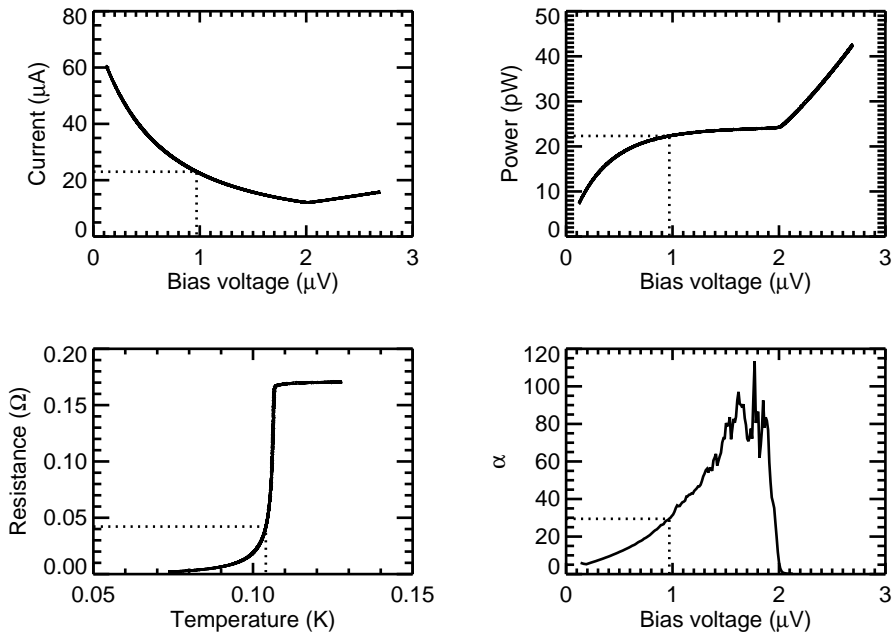
- How reproducible is this result?

Figure 5.1: **Top left:** $I(V)$-characteristic of sensor X038 with square absorber. **Top right:** $P(V)$-curve calculated from the $I(V)$-curve. The power plateau is at 24 pW. **Bottom left:** $R(T)$-curve calculated from the $P(V)$ and $I(V)$ curves. **Bottom right:** $\alpha(V)$-curve calculated from $R(T)$. The dotted lines indicate the values of the parameters associated with a bias set point of $V = 0.97 \ \mu V$.
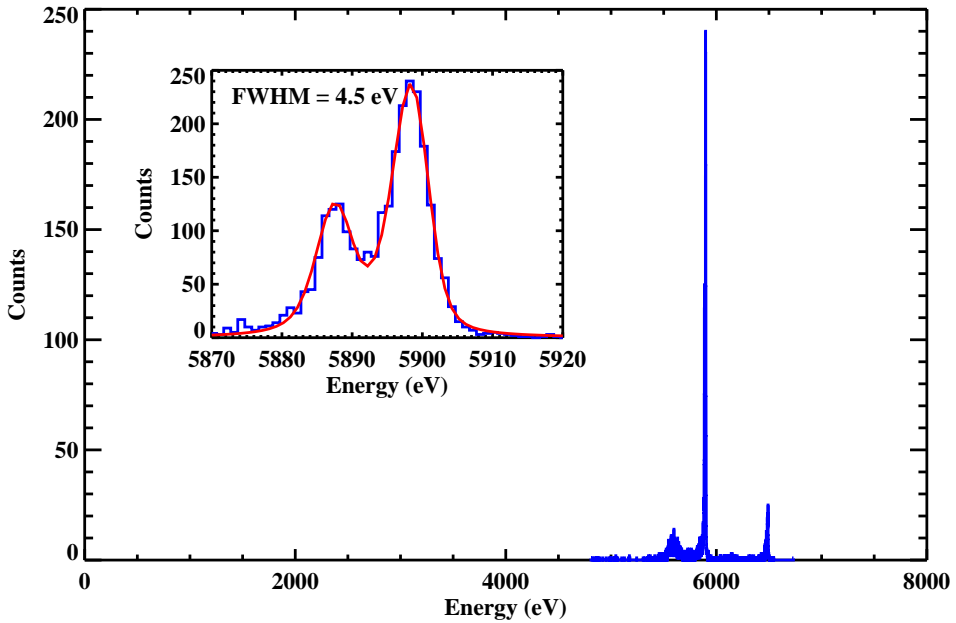
Figure 5.2: Energy spectrum of a ^{55}Fe test source measured with sensor X038 with a square absorber. Visible are the Mn Kα and Kβ lines at 5899 eV and 6490 eV, respectively. The counts to the left of the main peak are attributed to photons absorbed by the membrane. The inset shows an enlargement of the Kα-peak. The drawn line is a weighted fit to the data made by convolving the line profile from [25] with a Gaussian instrument response. The width of the best-fit Gaussian was 4.5 eV FWHM with a reduced χ^2 of 1.2.
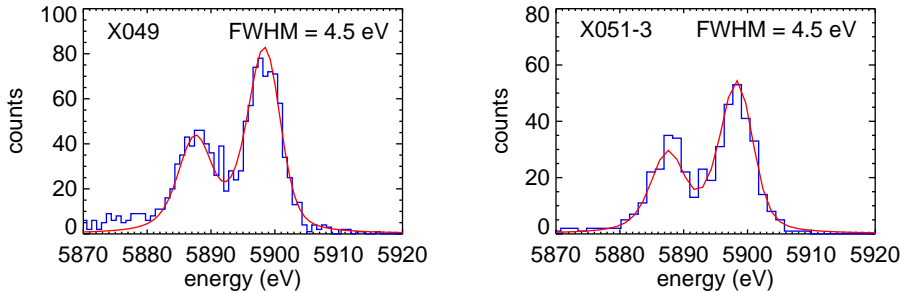
Figure 5.3: Measured ^{55}Fe Kα spectra with fitted model spectrum for sensors X049 (left) and X051-3 (right).

- Can the absorber size and efficiency be improved?

- What is the performance at lower X-ray energies?

- Can the energy resolution be improved?

These questions will be addressed in what follows.

Reproducibility To check the reproduciblity, a copy of X038 was made on a chip from a new wafer, called X048 (see appendix A for details). The new wafer had slightly different layer thicknesses from X038's, but they provided the same bilayer T_c of 100 mK. The Cu absorber had a thickness of 4.1 μm. This resulted in a slight decrease of heat capacity compared to X038: $C = 0.54$ pJ/K. However, the theoretically expected performance does not change significantly. During tests, this sensor had an energy resolution of 4.7 eV at 5.9 keV, comparable with the earlier X038. The fall time of the pulses was ~ 100 μs. This indicates that the performance is not dependent on a specific wafer. It also shows that the lithographic process is under control. This sensor will serve as a reference sensor for the variations in absorber as described below.

Absorption efficiency In order to improve the absorption efficiency, a new sensor labelled X049 was made, identical to X048 but with 3.4 μm Bi on top of the Cu absorber. This increased the efficiency at 6 keV from 39% to 88% without significantly increasing the heat capacity. Further details on this sensor are in appendix A. Pulse fall times for this sensor were again about 100 μs. The energy resolution was 4.5 eV, as shown in figure 5.3 (left). There appeared to be a low-energy tail present with the peaks in the spectrum. When the tail was ignored and the fit was made to the part that is dominated by the peaks,
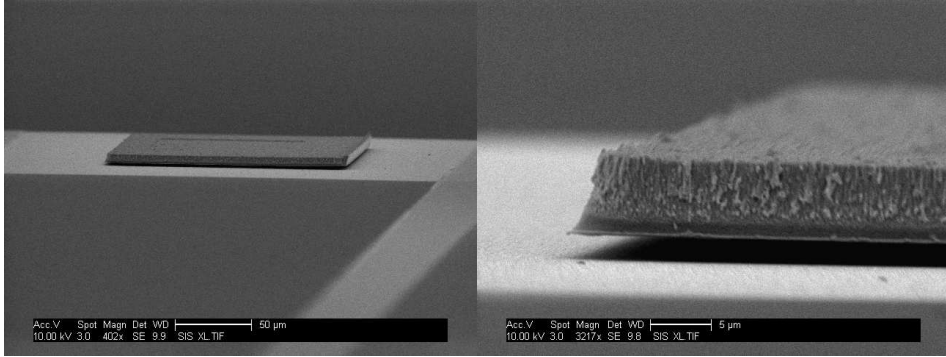
Figure 5.4: SEM images of sensor X051-3 with overhanging absorber, as a step towards a XEUS pixel with a high filling factor. **Left**: Overview of the sensor showing the absorber on top of the TES with the wiring on the side. **Right**: Detail of the overhanging absorber showing the Cu bottom layer and the Bi top layer. There is 1.3 μm space between the TES and the overhanging part of the absorber.

the reduced χ^2 was 1.1. The low-energy tail might be the result of differences between pulses in thermalisation in the absorber. While this issue is not completely resolved, we decided to move on towards a layout more compatible with the XEUS demands.

5.2   Mushroom absorber

This section is concerned with increasing the absorber size so as to optimise the filling factor, while keeping the TES the same. This can be done by creating a design in which the absorber overhangs the TES and wiring. As a starting point, a sensor (X051-3) was made with an absorber base identical to the sensors discussed previously, but with a 'hat' that overhangs the TES. Details are in appendix A. An image of the overhang is shown in figure 5.4. The absorber consisted a Cu layer covered with Bi. In this sensor, the Bi provides the stopping power while the Cu provides the heat capacity and thermal conductance. The area of the TES covered by the absorber is increased from 10% to 27%. For the final XEUS design, a smaller TES and a larger overhang will be used, covering the whole TES and the wiring. The absorption efficiency is calculated to be 93% at 6 keV.

The effective time constant was found to be around 140 μs. The resolution was typically 5–6 eV, but in one short-exposure case, 4.5 eV was measured, as shown in figure 5.3 (right). This was a 22 s acquisition with only ~ 450 counts in the Kα peak. The reduced χ^2 of the fit was 0.7. It is not clear why the fall time and typical resolution did not reproduce compared to earlier sensors. There may be some problems in the Bi/Cu
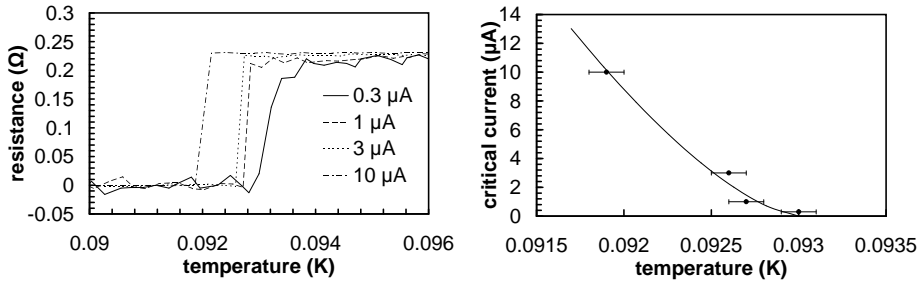
Figure 5.5: **Left**: 4-wire measurements of resistance as a function of temperature for a device with a type I superconducting ground plane with several low, constant measurement currents. **Right**: Critical current as a function of temperature (dots with error bars) derived from the figure on the left, with a theoretical curve (solid line) based on a critical current at zero temperature of 2 mA.

interface relating to the deposition conditions and the formation of an oxide layer on the Cu. Groups at NIST and GSFC working on similar devices also reported problems with Bi absorbers at higher ($\gg 1$ keV) X-ray energies [26]. This problem might be further investigated by using an X-ray test source at a lower energy.

5.3 Magnetic effects

Due to its superconducting nature, the TES is very sensitive to magnetic fields. This means that shielding the TES from magnetic fields is important, but a field can also be turned to an advantage. Since α is dependent on the set point, it may be that at some set points, the constraint of (3.15) is not satisfied. This results in instabilities in the circuit that cause oscillations on the output, which were sometimes observed. Since the intrinsic α of a bilayer is hard to adjust and must often be considered as given, an external magnetic field may be used to tune the transition steepness. Using a field of ~ 0.1 G, α is sufficiently suppressed to remove these instabilities.

Because the current through the TES also generates a magnetic field, α is always somewhat suppressed. In order to get a higher α and thus be able to use a higher heat capacity for the same energy resolution, the induced magnetic field might be suppressed by a superconducting ground plane. This is a layer of superconducting material close to the TES, but electrically insulated. If a type I superconductor is used for the ground plane, all magnetic field will be expelled. To see how the transition is affected by such a ground plane, a device was made with a 1 μm Al layer on the backside of the silicon nitride membrane (X052-1, see appendix A). $R(T)$ measurements were performed with different measurement currents, as shown in figure 5.5 on the left. In the case of a TES without the

Al ground plane, close to T_c there will already be a partial flux penetration, even when the current is smaller than the critical current, causing the TES to become resistive. With the Al ground plane, the TES will remain superconducting until the critical current is reached. In this case, the measurement current is equal to the critical current associated with the temperature at which the TES becomes resistive. These critical currents are plotted in figure 5.5 on the right. To this data, the theoretical relation

$$I_c(T) = I_c(0) \left(1 - \left(\frac{T}{T_c} \right)^2 \right) \sqrt{1 - \left(\frac{T}{T_c} \right)^4} \qquad (5.1)$$

was fitted [27]. This resulted in a value of the critical current at zero temperature of $I_c(0) = 2$ mA. With a TES cross-section area of 20 μm^2, the critical current density is 0.1 GA/m^2. This is useful information for determining the current necessary to bring a TES into the normal state, which is necessary to start the operation under voltage bias. Since the magnetic field is screened, the transition under bias conditions will be steeper than in a sensor without ground plane. With a higher α the same energy resolution can be obtained with a higher heat capacity, which is of interest for applications that require a larger detector size. However, the sensor X052-1 described here had the same heat capacity as the sensors without a ground plane. Due to the higher α, its effective thermal time constant will be shorter and it will be difficult to bias without oscillations caused by electro-thermal instabilities.

5.4   Conclusions

In conclusion, we can say that with the type of detector discussed here, an energy resolution below 5 eV at 5.9 keV is well possible. The effective fall time allows for a count rate of the order of 100 counts per second, with little resolution degradation and pulse rejection. The required absorption efficiency has been attained and a start has been made towards a geometry that fulfills the filling factor requirement.

The measured resolution was not as good as predicted by theory. The cause for this discrepancy is the subject of the next chapter.

CHAPTER 6

ENERGY RESOLUTION: GEOMETRY AND NOISE ASSESSMENT

In the previous chapter it was shown that the TES microcalorimeter has an energy resolution that is adequate for the intended application, but that it does not perform as well as theoretically predicted. In chapter 2, we have calculated a theoretical resolution based on expressions for phonon and Johnson noise and a small-signal responsivity model. This was compared to a resolution obtained from a measured spectrum of a ^{55}Fe radioactive source and a major discrepancy was found:

Resolution based on small-signal theory: 1.7 eV
Measured resolution at 5.9 keV: 4.5 eV

This chapter investigates a number of possible causes for this discrepancy. We will perform a quick check for aborption position dependence and then discuss a source of excess noise and its dependence on the geometry by means of a numerical simulation. Finally, we will look at the validity of the responsivity model.

6.1 Position dependence

An effect that could degrade the energy resolution is that of the dependence of the detected energy on the position of the photon absorption in the absorber. In a sensor such as X038 (see appendix A), the TES might react faster to energy deposited at the edge of the absorber, close to the TES, than to energy deposited in the centre of the absorber, which needs time to spread out to reach the TES. This would result in a difference in rise time of

the pulse. Since the same filter, with a single rise time, is used for both cases, a difference in deduced energy might arise. However, the read-out cannot detect changes faster than the electrical time constant L/R. So, if the heat diffusion occurs faster than this time constant, there is no way to register any difference between absorption locations. We can compare L/R to the diffusion time constant C_{abs}/G_{abs} by substituting some typical values:

$$
\left.
\begin{array}{rcl}
C_{abs} & = & 0.40 \,\mathrm{pJ/K} \\
G_{abs} & = & 0.12 \,\mu\mathrm{W/K}
\end{array}
\right\} \quad \Rightarrow \quad C_{abs}/G_{abs} = 3.3 \,\mu\mathrm{s}
$$

$$
\left.
\begin{array}{rcl}
L & = & 0.50 \,\mu\mathrm{H} \\
R & = & 0.020 \,\Omega
\end{array}
\right\} \quad \Rightarrow \quad L/R = 25 \,\mu\mathrm{s}
$$

The thermal conductance is obtained from the electrical resistance of the Cu absorber using the Wiedemann-Franz law. The fact that the diffusion time is faster than the electrical time constant suggests that any position-dependent effects will not be detectable and thus not contribute to the energy resolution.

For the overhanging Cu/Bi absorber of sensor X051-3, the situation is much the same. Although the Bi has a low thermal conductance, the Cu layer ensures sufficiently fast thermalisation to avoid position-dependence. For this configuration, no problems are to be expected, but care should be taken that this remains the case also when the absorber size is increased further and the Cu layer is made even thinner.

6.2   Excess noise

An important cause of the discrepancy between theoretical and measured energy resolution is the presence of excess noise, that is noise in the detector other than described in section 2.4. To see whether this is present, the noise can be measured as a function of frequency at a specific set point with a spectrum analyser. Using the parameters obtained from the $I(V)$-curve, the theoretical noise as described in section 2.4 can be calculated and compared to the measured noise. Figure 6.1 (left) shows a typical measured noise spectrum with the calculted noise components of section 2.4 indicated. It is clear that there is a large discrepancy at frequencies above 1 kHz. From the measured noise, the NEP can be calculated by dividing it by the responsivity (2.30), which is calculated from the parameters obtained from the $I(V)$-curve. From the NEP, the expected resolution based on the measured noise can be calculated through (2.37) and compared to the theoretical resolution. For the sensor X038 discussed previously, the resolution based on the noise comes to 3.0 eV. To summarise, we have:

Resolution based on small signal theory: 1.7 eV
Resolution calculated from measured noise and small-signal responsivity: 3.0 eV
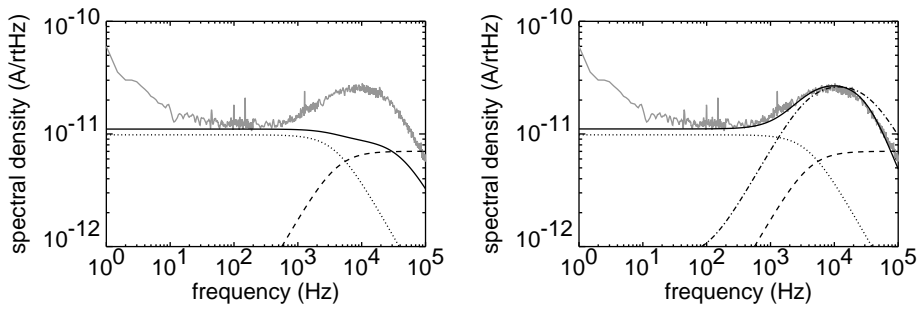Measured resolution at 5.9 keV: 4.5 eV

Figure 6.1: **Left**: Measured noise spectrum of sensor X049 at set point $V = 1.2$ μV (grey), together with theoretical noise spectra of phonon noise (dotted), Johnson noise (dashed) and total noise (solid). Unlike the other curves, the curve for the total noise includes the cut-off at ~ 20 kHz caused by the electrical time constant in the system, so that it may be compared with the measured curve. The $1/f$ component in the measured curve is assumed to originate from the SQUID, but the noise bump at frequencies above 1 kHz is from the sensor. Clearly the noise cannot be described just by phonon and Johnson noise. **Right**: The same noise spectrum, but with internal thermal fluctuation noise (dash-dotted) included in the theoretical curves. This gives a good description of the noise above 100 Hz.

From the first two numbers and figure 6.1 (left), it is clear that excess noise is present, having a significant contribution to the energy resolution. But comparison with the third number shows that this is not the complete explanation for the discrepancy. In what follows, the excess noise will be examined further. Later, we will look at the remaining discrepancy.

Flux flow noise   One possible source of excess noise is flux flow noise [28]. This is noise caused by voltage pulses that are the result of the movement of magnetic flux vortices in the superconductor under the influence of the Lorentz force. The presence of this type of noise may cause degradation of the resolution. To see whether this effect is present in our devices, a sensor was made with a Nb ground plane on the backside of the Si_3N_4 membrane (X055-6, see appendix A). Nb is a type II superconductor, which will allow flux to penetrate but make it harder for the vortices to move, effectively pinning them. This should decrease the effect of flux flow noise, if present. Of this sensor, the noise was measured and compared to that of earlier sensors. No significant reduction in current noise was found, so we conclude that the effect of flux flow noise on the current noise in our devices must be less than 20 pA/$\sqrt{\text{Hz}}$.

Superconductivity fluctuation noise   Flux flow noise is associated with the creation and destruction of flux vortices at the edges of the TES. A way to avoid such edge effects is to use an edgeless geometry. This has been tried by Luukanen et al. in a so-called Corbino geometry [29]. This is a round TES with a circular outer contact. The current flows from the outside through a superconducting disc to a centre contact and radially back through the TES. There are no edges parallel to the direction of the current, excluding any edge effects. Unfortunately, this geometry showed a lot of excess noise, and the energy resolution was degraded compared to earlier devices. The excess noise was explained as fluctuations in the location of the boundary between the superconducting and normal regions. This boundary is very sharp in this geometry because of the radial current distribution. The current density is the highest in the centre, and this area will be normal when the sensor is biased in the transition. The normal area is surrounded by a superconducting area. Fluctuations in the location of the boundary result in resistance fluctuations which are observed as current noise. In the square sensor geometry as used by SRON, the distribution of superconducting and normal regions is less well-defined and the superconductivity fluctuation noise is not dominant.

Internal thermal fluctuation noise   In any closed thermodynamical system at non-zero temperature, there is a random movement of energy, but the total amount of energy is conserved. The magnitude of the fluctuations depends on the temperature and the heat capacity of the system. When two such systems of equal temperature are placed into contact with each other, energy transfer occurs across the boundary. In this situation, the
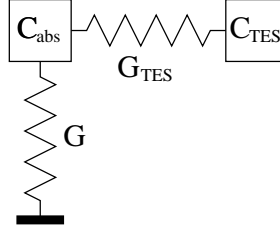
Figure 6.2: Thermal schematic for the model of energy fluctuations over the heat link G_{TES} between the TES and the absorber in a lateral sensor. The link to the bath G is shown to connect to the absorber because it dominates the electron-phonon coupling due to its larger volume.

amount of energy in a single subsystem is not constant. This physical principle underlies the model that follows.

Hoevers et al. have shown that excess noise in a lateral TES/absorber combination can be described by a model based on thermal fluctuations in the TES itself [30]. In this model, the TES and the absorber are placed side by side, as shown in figure 6.2. There is a heat link between the two, dominated by the finite thermal conductance of the TES itself. Random energy fluctuations over this heat link cause the TES temperature to fluctuate. This temperature noise has a white spectrum up to a certain cut-off frequency, determined by the heat capacity and thermal conductance of the TES. The total integrated temperature fluctuations are normalised to $\sqrt{k_B T^2 / C_{\text{TES}}}$. The temperature fluctuations result in fluctuations of the TES resistance, which are observed as current noise.

This model of internal thermal fluctuation noise (ITFN) introduces a current noise component that can be written as

$$i_{\text{ITFN}} = \delta T_{\text{TES}} \frac{\alpha I}{T} \frac{R}{R+R_s} \frac{1}{1+\beta L_0} \sqrt{\frac{1+4\pi^2\tau^2 f^2}{1+4\pi^2\tau_{\text{eff}}^2 f^2}} \frac{1}{\sqrt{1+(f/f_{\text{TES}})^2}} \qquad (6.1)$$

with δT_{TES} the density of the temperature fluctuations in the TES, given by

$$\delta T_{\text{TES}} = \sqrt{\frac{4k_B T^2}{G_{\text{TES}}}} \qquad (6.2)$$

and f_{TES} the cut-off frequency of the fluctuations, given by

$$f_{\text{TES}} = \frac{G_{\text{TES}}}{2\pi C_{\text{TES}}}. \qquad (6.3)$$

Here, G_{TES} is the thermal conductance inside the TES and C_{TES} the heat capacity of the TES. G_{TES} can be estimated using the Wiedemann-Franz law:

$$G_{\text{TES}} = \frac{L_n T}{R_n} \tag{6.4}$$

with L_n the Lorenz number 2.45×10^{-8} WΩ/K^2 and R_n the normal resistance of the TES. Although the geometry is different in the case of the central absorber, it is likely that a similar noise component is present. After all, we are still dealing with two systems in contact with each other. However, the value we should assume for G_{TES} is probably higher than in the case of a TES without absorber on top, since the central absorber partially short-circuits the TES thermally. In figure 6.1 (right), this noise component is included in the theoretical noise curves, using a best-fit value for δT_{TES} of 2.3 nK/$\sqrt{\text{Hz}}$. The total theoretical noise shows a good match with the measured noise.

The most distinctive property of this noise component is its dependence on $\alpha I / T$, a factor which, in turn, depends on the bias set point. In order to see whether it is indeed this type of noise that is present in this type of sensor, we can plot the measured and calculated noise as a function of set point. Using an RMS voltmeter, the noise integrated over the whole bandwidth was measured as a function of set point. Filters were used to limit the measurement band to well-known values, typically 100 Hz–20 kHz. The result is shown in figure 6.3. The curve which incorporates the ITFN component describes the noise well at bias levels above 1.3 μV, but deviates at lower bias voltage set points. This is probably due to problems with determining α at these set points. As the expression for α contains the resistance in the denominator, it is highly sensitive to the resistance value at set points low in the transition. The resistance is determined from a measured $I(V)$-curve. A small offset in this measurement can cause up to a factor of ~ 2 uncertainty in α. The strong correlation of the excess noise with α means that it must be of a thermal origin. This strengthens the case for the ITFN model.

For the curve in figure 6.3, a value of 3.0 nK/$\sqrt{\text{Hz}}$ is used for δT_{TES} in (6.1). Through (6.2), this results in a calculated G_{TES} of 68 nW/K. This is very high compared to the value from the Wiedemann-Franz law, 6.0 nW/K, differing by a factor of ~ 11. In [30], this factor was found to be ~ 4. Evidently, the presence of the central absorber reduces the sensor's sensitivity to this type of noise. The role of the absorber with respect to the ITFN level is explored in depth in the next sections.

6.3   Zebra absorber

In the previous section it has been established that the excess noise in devices with a central absorber can be described with a model of thermal fluctuations inside the TES, albeit with a lower value of δT_{TES} than in the case of a configuration with TES and absorber side by side. We therefore assumed that the magnitude of ITFN component was
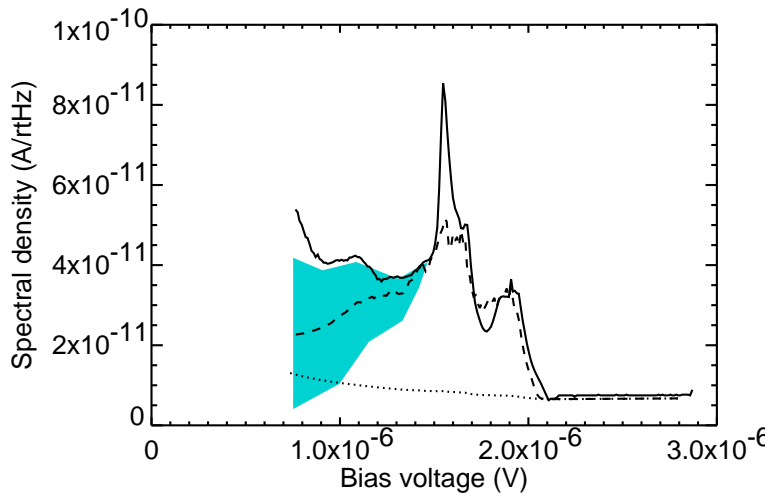
Figure 6.3: Current noise averaged from 100 Hz to 20 kHz as a function of bias voltage for sensor X038. Plotted are the measured noise (solid), the calculated noise consisting of phonon and Johnson noise (dotted) and the calculated noise including an ITFN component with $\delta T_{\text{TES}} = 3.0$ nK/$\sqrt{\text{Hz}}$ (dashed). The shaded area indicates the estimated standard deviation of the dashed curve, which becomes large at low set points due to difficulties in determining α there.

dependent on the absorber geometry. This section describes the experiments that were performed to test this assumption.

Thermal fluctuations are always present in any system with a non-zero temperature. They can be thought of as random movements of (thermal) energy from one location to another, causing a temperature fall in the first location and a temperature rise in the other. In a TES, these temperature fluctuations are translated into resistance fluctuations, which in turn may be visible as fluctuations in the current through the voltage-biased TES. However, in a sensor without an absorber, an increase in resistance in one location will be compensated by a decrease in resistance in another, effectively cancelling out any current fluctuations. In other words, if energy is conserved within the TES, the temperature averaged over the TES is constant and so is the total resistance. The magnitude of current noise caused by thermal fluctuations in such a TES will be negligible. This does not hold for a sensor that includes an absorber, since it is no longer homogeneous. The absorber geometry makes the internal thermal fluctuation noise (ITFN) visible in three ways:

Heat capacity distribution Energy fluctuations between areas with different heat capacity cause different temperature variations in those areas. As the heat capacity of the absorber is large compared to that of the TES, a temperature rise in the absorber will be smaller than the corresponding temperature fall in the TES.

Temperature sensitivity distribution Temperature fluctuations in areas with different temperature sensitivity (α) cause different resistance fluctuations in those areas. The absorber resistance is not sensitive to temperature ($\alpha = 0$), so an increase in resistance in the TES will not be compensated by a corresponding decrease in resistance in the absorber.

Current density distribution Resistance fluctuations in areas with different current density cause different fluctuations in the TES current. The presence of a low-resistance absorber may cause a non-uniform current density distribution. The decrease in the total current caused by a resistance increase in an area with low current density will be smaller than the increase in total current caused by a resistance decrease in an area with high current density.

To test this, devices with so-called zebra-stripe absorbers were fabricated: X043 with a single stripe and X047 with four stripes. These stripes are rectangular absorbers extending over the whole width of the TES, perpendicular to the direction of the current. Details are given in the table in appendix A. Again, the heat capacities were kept the same as the reference device. The idea behind the stripes is that, unlike in the case of the central absorber, the current density in these devices is completely uniform. This eliminates the effect that a non-uniform current density distribution has on the ITFN. The effects of the heat capacity distribution and temperature sensitivity distribution are still in place. The different number of stripes provide a different number of areas of those parameters. Of these sensors, noise spectra were measured at various bias points. Two examples are
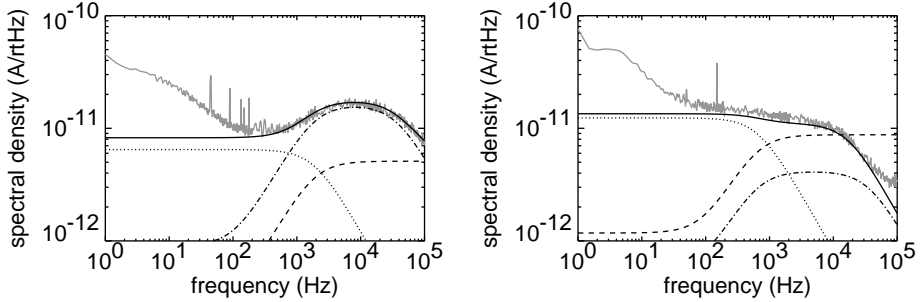
Figure 6.4: Current noise spectra of sensors X043 (one stripe, left graph) and X047 (four stripes, right graph). The grey curve is the measured noise while the black curves are theoretical noise spectra based on parameters obtained from the $I(V)$-curves: phonon noise (dotted), Johnson noise (dashed), ITFN (dash-dotted) and total noise (solid). The ITFN curves are fitted by adjusting the parameter δT_{TES} to the values of $4.0\,\text{nK}/\sqrt{\text{Hz}}$ (one stripe) and $1.3\,\text{nK}/\sqrt{\text{Hz}}$ (four stripes). The curve for the total noise includes the cut-off caused by the electrical time constant at $\sim 20\,\text{kHz}$.

shown in figure 6.4. The spectra have a $1/f$-component that is also present in spectra taken with the sensor in the normal state. This component is assumed to originate from the SQUID and not from the sensor. The spectrum of the single-stripe sensor is dominated by the ITFN component, just like the sensors with a central absorber discussed earlier. However, the spectrum of the four-stripe sensor can almost be described by phonon and Johnson noise alone. Only a small ITFN component is nescessary. Clearly the geometry plays a role in the magnitude of the ITFN parameter δT_{TES}. To investigate this geometry dependence in more detail, a numerical noise simulation of these devices was performed.

6.4 Numerical noise simulation

In this section, we will discuss the details and results of the numerical simulation used to gain insight into the geometry-dependence of the noise. First, the method and verification of the simulation is described. Then, a one-dimensional array of elements is simulated. In this way, only sensors that have a uniform cross-section can be simulated. The simulation is later extended to a two-dimensional grid, which does not restrict the simulated sensors to uniform cross-sections.

6.4.1   Method

Noise is a small-signal effect, and can be calculated using the small-signal equations in section 2.4, which are expected to yield the correct results. These equations however, assume the sensor to be a single element. To investigate the influence of a sensor geometry consisting of different elements on the spectral noise from the microcalorimeter, a numerical simulation was used. The simulation consisted of a system of equations which were solved simultaneously using the Saber simulator from Synopsys Inc.

The process of the simulation involves a description of the system in terms that the simulator can understand. The sensor is divided into a number of discrete elements with their own temperature, electrical resistance, noise sources etc. These elements are then allowed to exchange energy according to heat flow equations. Starting from some initial conditions, the equilibrium state can be calculated. In that state, the effect of the noise sources on the output signal can be calculated and the noise spectra can be plotted. The Saber program includes facilities for probing the system in different locations and for generating all kinds of graphs. Technical details on the simulation are given in appendix C.

6.4.2   Verification

With the components described in the appendix, a simple single-element biased TES model can be built, as shown in figure 6.5. As the current noise levels for phonon and Johnson noise are known analytically in this simple case (see section 2.4), we can use this model as a verification of the simulation. To do so, the simulation was run using realistic parameters (table 6.1) and a spectrum of the current noise through the inductor was plotted, shown in figure 6.6. The theoretical noise levels are also given in table 6.1. The theory and the simulation are in good agreement. Because our basic building block adheres to the analytically expected results, we are confident that more complicated simulations will also yield meaningful results. We will now use this simulation to investigate the dependence of the noise on the geometry.

6.4.3   One-dimensional array

Using the building block consisting of a TES thermometer and a heat capacity, we can construct a more complicated sensor geometry. To start with, we will look at a one-dimensional array of sensor elements coupled by thermal conductors to each other (G_{int}) and to the bath (G_b). This is illustrated in figure 6.7. Since the array is one-dimensional, only sensors with a cross-section that is identical over the whole width can be simulated. Five one-dimensional designs were simulated. Along with the descriptions below, a little cartoon of the cross-section is given. In these pictures, a thicker part represents an area of higher heat capacity and thermal conductivity. The shaded areas are insensitive to
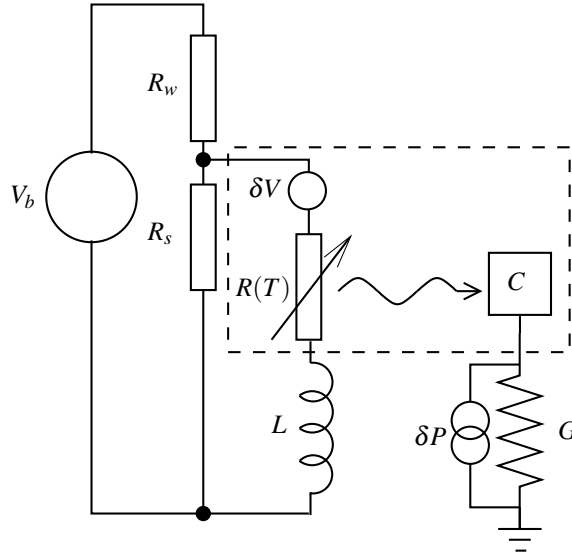
Figure 6.5: Simple biased TES model: the temperature-dependent, power-dissipating TES resistor is thermally coupled to a heat capacity linked to a bath. Noise sources are present in series with the TES resistor and across the thermal link. The components within the dashed rectangle form a basic building block for a more complex model.

Table 6.1: Parameters used in the verification of the TES simulation using a single element, and the analytical noise levels.

| Parameter	Symbol	Value
Bias voltage	V_b	20 mV
Wiring resistance	R_w	130 Ω
Shunt resistance	R_s	7 mΩ
Inductance	L	0.5 μH
Steepness of transition	α	10
Normal resistance	R_n	0.1 Ω
Critical temperature	T_c	0.1 K
Bath temperature	T_b	0.02 K
Heat capacity	C	0.5 pJ/K
Thermal conductance	G	0.33 nW/K
Johnson noise (suppressed)	$i_{\mathrm{jo}}(f=0)$	1.6 pA/$\sqrt{\mathrm{Hz}}$
Johnson noise (unsuppressed)	$i_{\mathrm{jo}}(f\to\infty)$	9.9 pA/$\sqrt{\mathrm{Hz}}$
Phonon noise	$i_{\mathrm{ph}}(f=0)$	9.3 pA/$\sqrt{\mathrm{Hz}}$
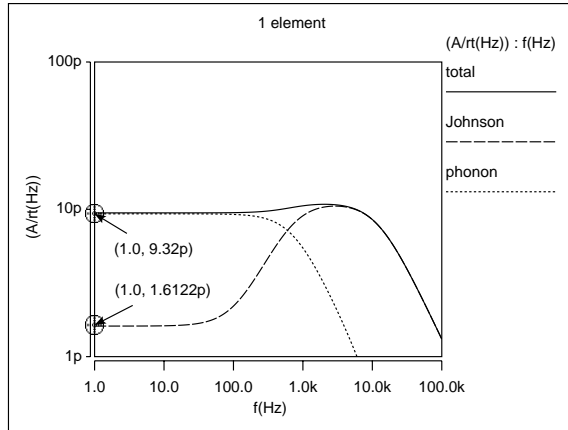
Figure 6.6: Example of the output of the Saber program: simulated noise spectra of phonon and Johnson noise in the case of a single element. The levels and corner frequencies agree with the theoretical values.
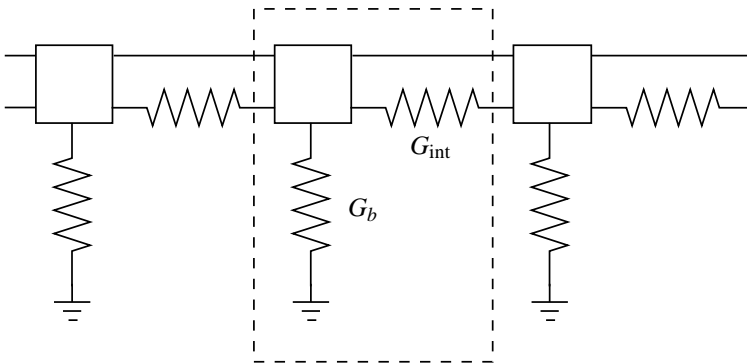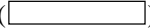

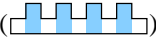**Figure 6.7**: Part of an one-dimensional array of simulation elements. The square boxes contain the components inside the dashed rectangle in figure 6.5. Each has electrical connections to its neighbours (horizontal lines). It is also connected by thermal conductances to its neighbours (G_{int}) and to the bath (G_b). A single element of this array is indicated by a dashed rectangle.

Table 6.2: Total values of the simulation parameters. The values per simulation element are obtained by dividing (or in the case of the internal conductances: multiplying) the values in the table by the number of elements.

TES normal state resistance	0.20 Ω
TES internal thermal conductance	12 nW/K
TES heat capacity	0.14 pJ/K
Absorber resistance	20 mΩ
Absorber internal thermal conductance	0.12 μW/K
Absorber heat capacity	0.40 pJ/K
Total thermal conductance to bath	0.33 nW/K

temperature changes, while the unshaded areas represent temperature-sensitive TES parts. The following designs were simulated:

1. A homogeneous design with all the heat capacity distributed evenly throughout the sensor (▭).

2. A design with the heat capacity concentrated mostly in the middle third of the sensor (▭). In this part, the thermal conductivity is also increased, the electrical resistance is low and the sensor is not sensitive to temperature change ($\alpha = 0$). This design simulates the single-stripe zebra absorber from the previous section.

3. A similar design but with the absorber part in 4 seperate sections (▭), simulating the four-stripe zebra absorber.

4. A design with higher heat capacity and thermal conductivity in the centre but with a TES extending over the whole sensor (not suppressed by the absorber) (▭). This is a test to see how the noise is influenced by the distribution of heat capacity, independent of the TES.

5. A design with a homogeneous heat capacity distribution but with the TES insensitive to temperature in the centre (▭). This is a test to see how the noise is influenced by the TES, independent of the distribution of heat capacity.

Each simulated design consisted of 27 elements. This number was chosen to allow for a large number of different designs to be simulated with the same number of elements. The elements could be absorber ($\alpha = 0$) or TES ($\alpha > 0$) elements. The heat capacity, thermal conductance and electrical resistance, as given in table 6.2, were divided as follows over the elements. The TES parameters were divided by the total number of elements, while the absorber parameters were divided by the number of absorber elements.
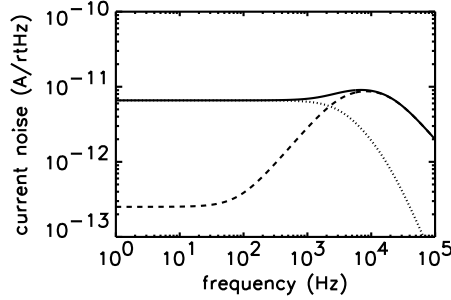
Figure 6.8: Current noise spectra obtained from the numerical simulation of a one-dimensional homogeneous array (design 1) with $\alpha = 40$. Dashed curve: Johnson noise; dotted curve: noise from the link to the bath; solid curve: total noise.

For an absorber element, the TES and absorber parameters were added. For example, with 27 elements of which 9 are absorber elements, the heat capacity of a single TES element is $0.14/27 = 0.0052$ pJ/K. The heat capacity of a single absorber element is $0.40/9 + 0.14/27 = 0.050$ pJ/K. The total heat capacity was kept constant to allow comparisons between the designs. The thermal conductance to the bath is distributed evenly over the sensor. This is not strictly correct since a component of the thermal conductance is the electron-phonon coupling, which scales with the volume of a sensor element. But since $G_{int} \gg G_b$, the difference in thermal conductance to the bath is insignificant and an even distribution is a good approximation.

We are particularly interested in the behaviour of the noise produced by the internal thermal conductances (G_{int} in figure 6.7), as these are responsible for the ITFN. In the homogeneous case (1), this noise component is absent, as visible from figure 6.8. In design 2 (figure 6.9, left), this component is clearly present. Apparently it originates from the inhomogeneous distribution of heat capacity and temperature sensitivity in this design. In the case of the four-striped absorber (3), the ITFN component is much less prominently present (figure 6.9, right). This can be seen more clearly if we increase α, since this noise component scales with $\alpha I/T$. In figure 6.10 the noise from designs 2 and 3 is plotted with $\alpha = 120$. In the single-stripe case (design 2), the ITFN introduces a significant bump at frequencies above 10 kHz, while this is much less pronounced in the four-stripe case (design 3). This clearly demonstrates the geometry dependence of the ITFN component.

Designs 4 and 5 were intended to separate the effects of the heat capacity distribution and the temperature sensitivity distribution. In figure 6.11, the noise spectra for those cases are shown. Clearly, the inhomogenity in the heat capacity and thermal conductivity are more important than that in the temperature sensitivity. However, when we compare

Figure 6.9: Current noise spectra obtained from the numerical simulation of a one-dimensional array with $\alpha = 40$. The curves are coded in the same manner as in figure 6.8, with the addition of the dash-dotted curve: noise from internal thermal link. **Left**: Design 2, single-stripe zebra absorber. **Right**: Design 3, four-stripe zebra absorber.

Figure 6.10: Current noise spectra obtained from the numerical simulation of one-dimensional array with $\alpha = 120$. The curves are coded in the same manner as in figure 6.9. **Left**: Design 2, single-stripe zebra absorber. **Right**: Design 3, four-stripe zebra absorber.
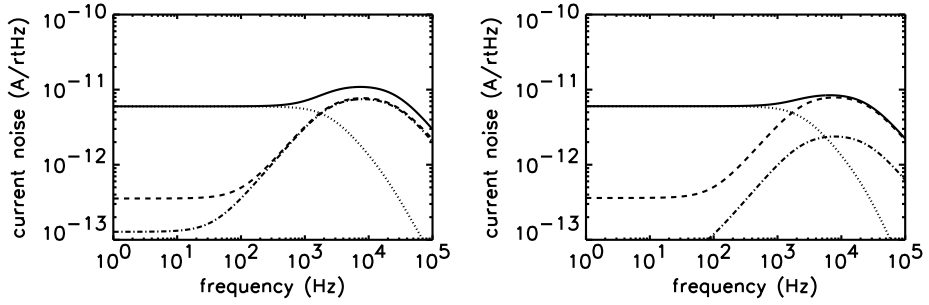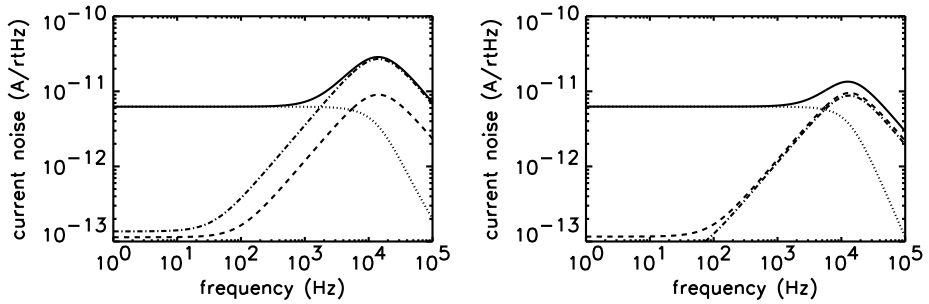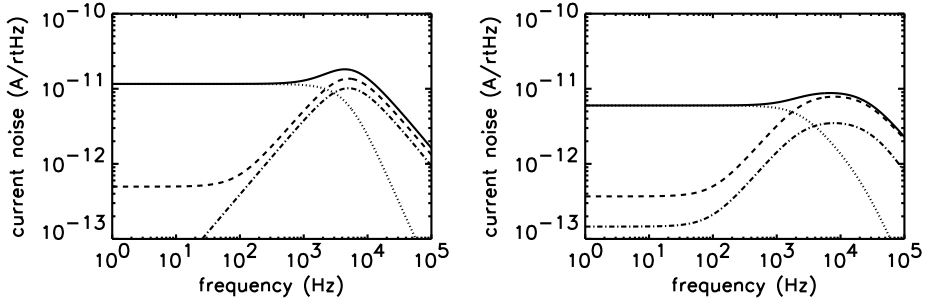
Figure 6.11: Current noise spectra obtained from the numerical simulation of the 1-dimensional array with $\alpha = 40$. The curves are coded in the same manner as in figure 6.9. **Left**: Design 4, central absorber with the TES covering the whole sensor. **Right**: Design 5, homogeneous heat capacity with the TES suppressed in the centre. The 'bumps' in the Johnson and ITFN spectra in the left plot look sharper because the L/R cut-off is at a lower frequency than in the right plot, due to a lower value of the total resistance.

figures 6.8 and 6.11 (right), we see that the inhomogenity in the temperature sensitivity also accounts for some contribution to the total noise.

By plotting the contribution of the single noise source at a time, it was revealed that the contributions to the ITFN were the largest from the elements close to the boundaries between absorber and TES, and small from the parts far away from those boundaries. For both designs 4 and 5, this is shown in figure 6.12. This can be understood as follows: As discussed earlier, the ITFN arises from energy fluctuations across a boundary. The closer a noise source is to such a boundary, the more energy is transported across. A larger energy difference between either side of the boundary creates a larger deviation in electrical current, which means a higher noise level.

The asymmetry in figure 6.12 (left) is caused by the asymmetry in the chosen simulation element, as shown in figure 6.7. The internal thermal conductance G_{int} is always to the right of the heat capacity C with which it forms an element, so the region of higher heat capacity does not completely overlap with the region of higher thermal conductance.

In a microcalorimeter with a discrete absorber and TES side-by-side, the ITFN spectrum can be described by (6.1). This equation also turns out to describe fairly accurately the total ITFN spectrum from the simulated multi-element sensor, with the parameter δT_{TES} substituted with a parameter δT_n, which is specific to a particular design. To check if δT_n only depends on the sensor geometry, the maximum in the ITFN spectrum was determined from the simulation for a number of set points (different values of I) and values
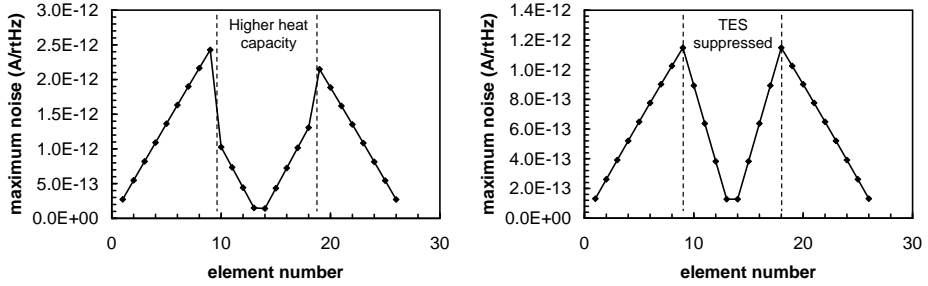
Figure 6.12: Maximum level in the noise spectra of the ITFN contribution per simulation element as a function of element number. **Left**: Design 4, with higher heat capacity and thermal conductivity in the centre region. **Right**: Design 5, with the thermometer suppressed in the centre.

of α. This maximum should be given by

$$i_{\text{ITFN,max}} = \delta T_n \frac{\alpha I}{T} \frac{\beta + 1}{2}. \tag{6.5}$$

To simplify things, the inductance L in the circuit was chosen very small so that the L/R cut-off does not play a role. As an example, in figure 6.13 the maximum ITFN from the simulation is plotted as a function of bias current with a fixed α and as a function of α with a fixed bias voltage in the case of the single-stripe sensor (design 2). As can be seen from the figure, for all these situations the maximum ITFN agrees with (6.5) using a single value of δT_n. This value was determined using a fit by eye. Also from designs with 2, 3, 4 and 13 stripes, plots were made of the maximum ITFN as a function of α and values for δT_n for these geometries were determined. These are shown in figure 6.14 (left). These values are a function of the number n of stripes in a sensor. This can be explained as follows:

The ITFN arises from thermal fluctuations across the boundary between absorber stripes and TES parts. In the frequency domain, the magnitude of these fluctuations will be frequency-independent up to a certain cut-off frequency. This frequency is mainly determined by the internal thermal conductance of the sensor, because this thermal conductance is much larger than the thermal conductance from the sensor to the bath. When the stripes get narrower, the time constant of the fluctuations gets shorter and the cut-off frequency will go up. Since the total integrated amount of thermal fluctuations inside the TES is fixed by the heat capacity, a higher cut-off frequency will result in a lower ITFN level.

Consider a one-dimensional TES with a heat capacity C_{TES} and an internal thermal conductance G_{TES}. On top of the TES are n absorber stripes, suppressing the temperature sensitivity of the TES in those places, as shown in figure 6.14 (right). The absorber
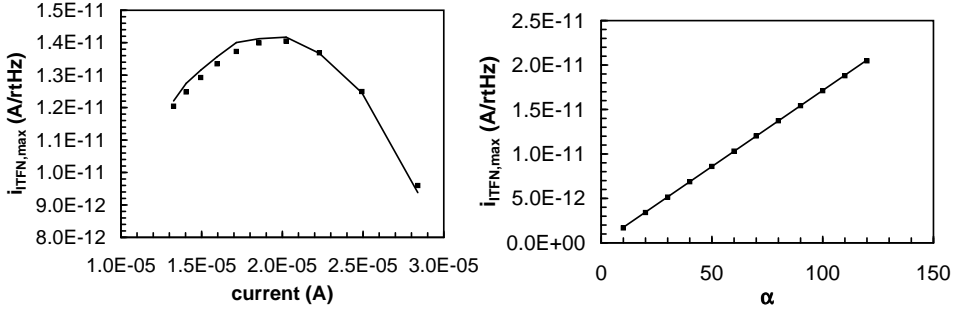
Figure 6.13: Maximum ITFN from a simulation of a single-stripe sensor (design 2) (squares), together with the theoretical values based on a value for δT_n of 1.4 nK/$\sqrt{\text{Hz}}$ (solid line). **Left**: The ITFN as a function of bias current with $\alpha = 80$. The parabolic shape is due to the fact that a higher I is associated with a lower resistive set point and therefore a lower β, so β decreases with increasing I. **Right**: The ITFN as a function of α with $V_b = 30$ mV.
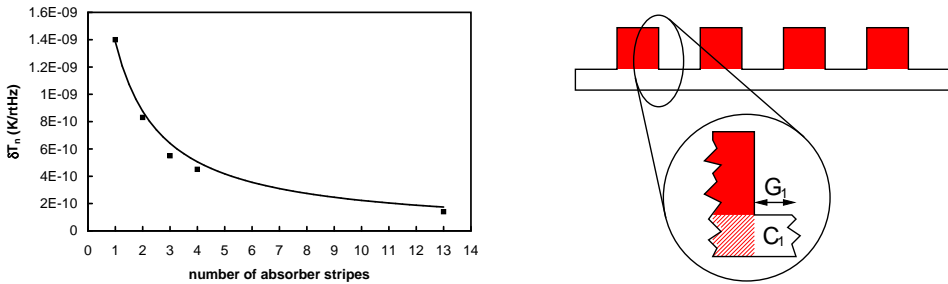
Figure 6.14: **Left**: Values of the parameter δT_n as a function of the number of absorber stripes in the sensor design (squares). The solid line is the theoretical relation as discussed in the text. Of course, there is no such thing as fractional stripes but a continuous curve is used to make the trend more clear. **Right**: Sketch of the cross-section of a 4-stripe sensor. The enlargement shows a TES piece on the right side of an absorber stripe. The hatched area indicates where the temperature sensitivity of the TES is suppressed.

stripes form local heat baths, with a TES piece the width of half a stripe on either side. This TES piece has a heat capacity $C_1 = C_{\text{TES}}/(4n+2)$ and a thermal conductance $G_1 = (4n+2)G_{\text{TES}}$, as indicated in figure 6.14 (right). Therefore, the cut-off frequency of the thermal fluctuations in one piece is

$$
\begin{aligned}
f_1 &= \frac{G_1}{2\pi C_1} &&(6.6)\\
&= (4n+2)^2 \frac{G_{\text{TES}}}{2\pi C_{\text{TES}}}. &&(6.7)
\end{aligned}
$$

Since all pieces are identical, the spectral shape of the temperature fluctuations in the whole TES is the same as that in one piece. It has the form

$$
\langle \Delta T^2(f) \rangle = \delta T_n^2 \frac{1}{1 + f^2/f_1^2}. \tag{6.8}
$$

Because the absorber heat capacity is large compared to the TES heat capacity, we can treat the absorber parts in the sensor as a local heat bath. Integrated over all frequencies, $\langle \Delta T^2(f) \rangle$ should be normalised to the total amount of thermal fluctuations in all TES pieces *not* covered by an absorber. This is equal to $(2n+1)k_B T^2/(n+1)C_{\text{TES}}$. In [31], a similar normalisation procedure was used for temperature fluctuations. We can write:

$$
\begin{aligned}
\frac{2n+1}{n+1}\frac{k_B T^2}{C_{\text{TES}}} &= \int_0^\infty \delta T_n^2 \frac{1}{1 + f^2/f_1^2} df &&(6.9)\\
&= \delta T_n^2 \frac{\pi}{2} f_1 &&(6.10)\\
&= (2n+1)^2 \delta T_n^2 \frac{G_{\text{TES}}}{C_{\text{TES}}} &&(6.11)
\end{aligned}
$$

This yields a value for the density of the visible temperature fluctuations of

$$
\delta T_n = \sqrt{\frac{1}{(n+1)(2n+1)}\frac{k_B T^2}{G_{\text{TES}}}}. \tag{6.12}
$$

This theoretical relation is also plotted in figure 6.14 (left), using the value for G_{TES} that was put into the simulation. It is clear that there is a good agreement between theory and simulation.
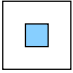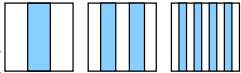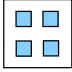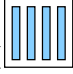
Summarising, we can say that the theory and the simulations indicate that having narrow TES segments decreases the contribution from the ITFN in the signal band. However, it is questionable that these striped TESes would make practical sensors. Because the absorption coefficient of the TES and the absorber differ by a factor of more than 3, the stripes introduce a position-dependent absorption efficiency. If the stripes were covered by a connecting absorber, this drawback could be overcome. However, using a normal

metal for this would short out the sensor, making it less sensitive. Adding an electrical insulator between the stripes and the absorber would remedy this, but also limit the thermal connection between absorber and TES. A possible solution would be a low-heat capacity mushroom absorber attached to a one of the stripes, but this has not yet been tried.

6.4.4 Two-dimensional array

In order to study the noise behaviour in more complex, though realistic, geometries, the simulation was done with a two-dimensional grid of elements. Each element consisted of a temperature-sensitive resistor and a thermal conductor in both the lateral and longitudinal direction, a heat capacity and a thermal conductor to the bath.

Models were built for the following geometries (with a cartoon of the top view of the sensor; the current flows from left to right):

1. A homogeneous TES (   ), as a base line.

2. A TES with a central absorber (   ), such as used in a practical sensor.

3. TESes with 1, 2 or 4 zebra stripe absorbers (   ), as a comparison with the simulations using a one-dimensional array.

4. A TES with four absorber segments arranged in a 2×2 fashion (   ).

5. A TES with 4 stripes that do not extend all the way to the edge, so as to leave a superconducting path through the TES and not introduce series resistance (   ).

Again, for each design a value for δT_n was fitted to the maximum of the ITFN component. These are indicated in figure 6.15. As expected, the ITFN in the homogeneous TES (design 1) was found to be negligible and is not plotted in the graph. In the one-dimensional case, the current density is the same in all elements. In the present two-dimensional case, this need not be so. In addition to the two mechanisms for making ITFN visible that were discussed above, this non-uniform current density introduces a third mechanism. The temperature fluctuations cause resistance fluctuations in different locations in the TES. The effect that these resistance fluctuations have on the TES current is weighted with the current density in the different locations. After all, we wouldn't
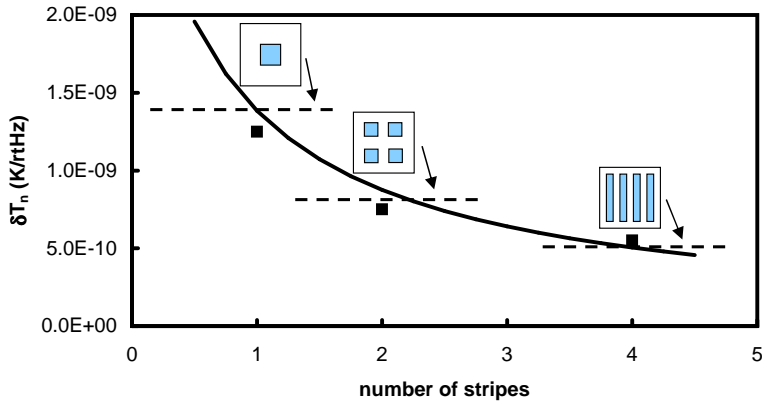
Figure 6.15: Values of the parameter δT_n for some 2-dimensional designs. The zebra designs with 1, 2 and 4 stripes are plotted with squares, while the values for the other designs are indicated by horizontal dashed lines for comparison. The curve is the theoretical relation (6.12) for the striped designs.

notice a change in resistance in an element that has no current flowing through it. Because of this, the change in resistance caused by heat exchange between two elements that have the same temperature sensitivity and heat capacity might not be cancelled out if the elements have a different current density. In figure 6.16 the simulated current density in design 3 (central absorber) is plotted. Under typical bias conditions, the TES has a higher resistivity than the absorber in the centre, so the largest part of the current will flow through the absorber, creating a non-uniform current distribution. Heat fluctuations between areas of different current density are possible in this geometry. In the single-stripe sensor, the current distribution will be uniform. There can be no heat fluctuations between areas of different current density. This explains why the ITFN is less visible in the single-stripe design than in the central absorber design, as shown in figure 6.15. This mechanism based on current distribution doesn't play a large role compared to the other two because in general there is a smooth gradient in the current density while the heat capacity and temperature sensitivity can change abruptly.

From the results of the simulation, we can conclude that thermal fluctuations in a sensor are made visible as ITFN by the presence of areas of different heat capacity and temperature sensitivity (α), and to a lesser extent by a non-homogeneous current density distribution. We have seen experimentally and in simulation that the ITFN can be manipulated by changing the width of the TES parts between the absorber parts. The design with four stripes not extending to the edge (design 5) shows the same low ITFN level as the design with the stripes extending to the edge, but presumably without the negative effects of having series resistance in the TES.
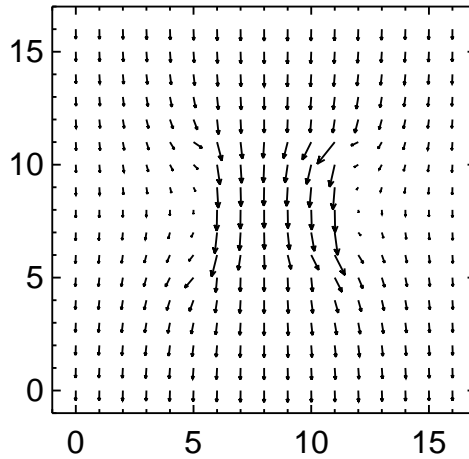
Figure 6.16: Current density distribution in a sensor with central absorber. The numbers on the axes indicate the position of the elements in the grid. The length of the arrows is proportional to the magnitude of the current through an element.

6.5 Responsivity model

In the previous sections we have seen that a noise model that includes ITFN could successfully describe the measured noise in the sensor. With a good understanding of the noise in the microcalorimeter, the discrepancy between theoretical resolution and resolution calculated from the measured noise has been resolved. However, we are still facing the discrepancy of a factor of ~ 2 between this resolution and the one measured using 5.9 keV X-rays. The answer to this lies in the small-signal approximation that has been made in the microcalorimeter model. This approximation is valid for the noise, which is a small-signal phenomenon, but can not be applied to 5.9 keV X-ray pulses, which are large-signal events.

6.5.1 Non-ideal pulse shape

In (2.37), the theoretical energy resolution is given in the case of optimum filtering and stationary noise, that is noise that does not change during the passage of a pulse. Our filtering, as described in appendix B, is not entirely optimum in the sense that it assumes a white spectrum for the noise. In reality, the noise is not exactly white, but it comes very close. As shown in section B.3.1 in the appendix, the assumption of white noise does account for a few percent in resolution degradation, but can not explain a factor of ~ 2. Furthermore, the noise is not completely stationary. This can be seen by calculating the

noise spectrum using parameter values as they are in the non-equilibrium situation during the passage of a pulse. Because the current becomes smaller when the sensor is heated by the absorption of a photon, the noise spectrum is in fact *lower* than in the set point. So, if the non-stationary character of the noise were taken into account, the theory would predict an even better resolution. It is clear that the effect of non-stationary noise cannot explain the discrepancy between theoretical and measured resolution.

The effect that *can* is that the responsivity (2.30), used to calculate the NEP, assumes an exponential pulse shape, whereas the real pulse shape differs significantly from this ideal shape. To make a more realistic prediction of the energy resolution, we need to look at the way the signal is filtered: it is multiplied by the pulse shape and integrated. In a general way, without assuming a particular signal shape, we can describe the effect of the filter on the signal $I(t)$ and the noise $i_n(f)$ as follows. The filtered signal output is

$$O = \int_0^\infty F(t)I(t)dt \tag{6.13}$$

where the filter $F(t)$ is identical to the signal but normalised to unit area:

$$F(t) = \frac{I(t)}{\int_0^\infty I(t)dt} \tag{6.14}$$

The noise passes through the same filter, but it has to be treated in the frequency domain and is multiplied quadratically by the Fourier transform of the time domain filter: $\overline{F}(f) = |\mathscr{F}(F(t))|$. The energy resolution is equal to the filtered noise transformed to units of energy. This is done through multiplication by the slope of the calibration curve, which is the derivative of the original energy E with respect to the signal output O:

$$\Delta E = 2.35 \frac{dE}{dO}\sqrt{\int_0^\infty \overline{F}^2(f)i_n^2(f)df} \tag{6.15}$$

As a check, we can look at a simple example. We will substitute white noise $i_n(f) = i_n$ and an exponential signal pulse $I(t) = ES(0)\exp(-t/\tau_{\mathrm{eff}})/\tau_{\mathrm{eff}}$, where $S(0)$ is the responsivity at zero frequency. The filter in the time domain is

$$F_{\mathrm{white,exp}}(t) = \frac{\exp(-t/\tau_{\mathrm{eff}})}{\tau_{\mathrm{eff}}} \tag{6.16}$$

so for the output signal we get

$$O_{\mathrm{white,exp}} = \frac{ES(0)}{2\tau_{\mathrm{eff}}}. \tag{6.17}$$

This gives us the factor dE/dO. The filter in the frequency domain is

$$\overline{F}_{\mathrm{white,exp}}(f) = \frac{1}{\sqrt{1 + 4\pi^2\tau_{\mathrm{eff}}^2 f^2}} \tag{6.18}$$

Table 6.3: Measured and calculated energy resolutions at 5.9 keV for different devices. The 'small-signal' numbers are obtained using the theoretical equation (2.38), while the 'large-signal' numbers come from (6.15) with measured pulse shapes and noise spectra. The uncertainty in the calculated large-signal numbers is estimated to be about 10%.

Device	Measured (eV)	Calculated (eV)	
		Small-signal	Large-signal
X037-2	4.2	2.1	4.4
X038	4.1	1.5	4.3
X043	4.7	3.0	3.9
X047	15.7	1.9	15.8
X049	5.3	2.4	4.7
X055-6	4.5	1.3	3.3

so for the energy resolution we obtain

$$\Delta E_{\text{white,exp}} = 2.35 \frac{2\tau_{\text{eff}}}{S(0)} \sqrt{\int_0^\infty \frac{i_n^2 df}{1 + 4\pi^2 \tau_{\text{eff}}}} \tag{6.19}$$

$$= 2.35 \frac{2\tau_{\text{eff}}}{S(0)} \frac{i_n}{2\sqrt{\tau_{\text{eff}}}} \tag{6.20}$$

$$= 2.35 \text{NEP}(0) \sqrt{\tau_{\text{eff}}}. \tag{6.21}$$

This is identical to what we get when we make the assumption of white noise in (2.37) [12].

For a practical use, we can substitute measured pulse shapes and noise spectra in (6.15) to calculate the energy resolution we should expect to obtain. To do so, we assume that $dE/dO = E/O$, that is a linear calibration relation between input energy and output signal. This assumption is justified when the signal pulses do not saturate in the detector nor in the read-out. The results from measured data for a few sensors are given in table 6.3. In most cases, there is an agreement between measured and calculated resolution that is better than 1 eV, or $< 20\%$. This shows that the discrepancy between theoretical and measured resolution is to be attributed to the limitations of the small-signal responsivity model. This can be understood by looking at figure 6.17. In the figure, the responsivity is shown for two pulse shapes: the exponential shape for the small-signal model and a more realistic shape for the large-signal model. (The original pulse shapes are shown in figure 6.18). They are normalised so as to provide the same output signal value when they are used as a filter. On the right is shown how a typical noise spectrum looks after filtering in these two models. It is clear that in the large-signal model, more noise passes through the filter which means that this model will predict a worse (but more realistic) energy resolution.
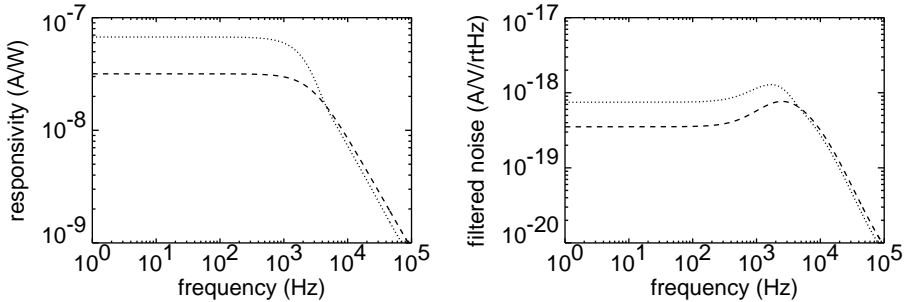
Figure 6.17: **Left**: simulated responsivity curves as a function of frequency for the theoretical small-signal model (dashed) and a numerical large-signal model (dotted), normalised to equal filtered-signal output. **Right**: A simulated noise spectrum filtered by the responsivity curves in the left-hand plot, dashed for the small-signal model and dotted for the large-signal model.

From the above, we can conclude that we will not be able to obtain the energy resolution predicted by (2.38) since it is based on a responsivity model that is inappropiate for large signals. So, what *can* we get? To answer this, we can use (6.15) with analytical noise spectra given by (2.25)–(2.27) and (6.1) and pulse shapes calculated from a numerical simulation. We will use the simulation to obtain the responsivity for a number of different set points and photon energies. The next section will explain the simulation.

6.5.2 Large-signal responsivity simulation

In this simulation, we will iteratively calculate the response of the sensor to an X-ray event. We will assume the circuit diagram as given in figure 2.7. The bias current I_b is fixed. We will allow the TES current to change instantaneously. Since we are now not concerned with just a single set point, the constant-α expression for the temperature dependence of the TES resistance, used in section 6.4, is not appropiate here. For most sensors, a linear $R(T)$-curve will be a fairly accurate description of the transition:

$$R(T) = \begin{cases} R_n + \frac{dR}{dT}(T - T_c) & \text{for } T \leq T_c \\ R_n & \text{for } T > T_c \end{cases} \qquad (6.22)$$

The state of the system is given by the TES temperature T. If initially this is not the equilibrium temperature, it should be allowed to stabilise for a few iterations. At a certain time t_γ, a photon is absorbed. In this algorithm, the symbol $\rightarrow$ means "becomes". The following computations should be performed for each time step:
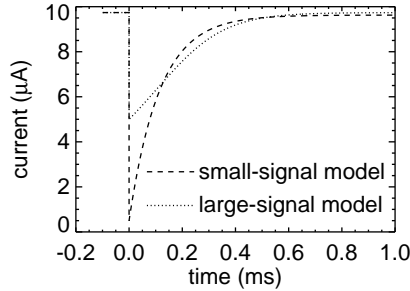
Figure 6.18: Impulse response of a modelled sensor based on small-signal theory (dashed) and on a large-signal numerical calculation using a linear $R(T)$-curve (dotted).

1. If $t = t_\gamma$, deposit the photon energy E in the TES:
   $T \rightarrow T + E/C$

2. Calculate the TES current:
   $I = I_b R_s / (R(T) + R_s)$

3. Calculate the net power:
   $P_{\text{net}} = I^2 R(T) - K(T^n - T_b^n)$

4. Calculate the new temperature:
   $T \rightarrow T + P_{\text{net}} \Delta t / C$

5. Repeat from step 1.

The duration of a time step Δt is chosen small compared to the time constant of the system. The current $I(t)$ now describes the impulse response of the system. Depending on the shape of the chosen $R(T)$-curve, this will be a pulse with an initially slow decay that speeds up when the current comes closer to the equilibrium current, as shown in figure 6.18. The shape is due to the fact that when the X-ray hits, the loop gain drops sharply and the time constant approaches the intrinsic time constant. After a while, it returns to the effective time constant in the set point.

Using this simple model, a fairly accurate pulse shape can be calculated. By Fourier-transforming the current curve, a frequency-dependent responsivity curve is obtained, to replace the analytical expression of equation (2.30).

Using the procedure described above with a linear $R(T)$-curve with a slope of 50 Ω/K, a normal resistance of 0.2 Ω and a critical temperature of 0.1 K, pulse shapes have been calculated for a few photon energies at different set points in the transition. Combined

Figure 6.19: **Left**: Energy resolution as a function of bias voltage set point obtained from simulated pulse shapes and analytical noise spectra for (top to bottom) 6 keV, 3 keV and 600 eV photons. For the dotted part of the curves, the pulses were clipped because the sensor was driven into the normal state and started to saturate. In this regime, measurement is still possible but the detector becomes highly non-linear and an accurate calibration is 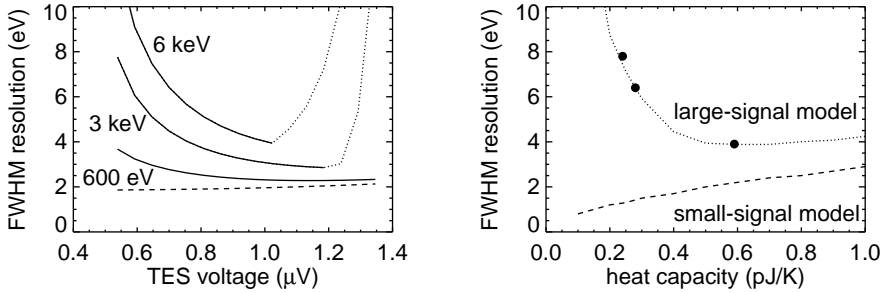necessary. The dashed curve is the energy resolution based on the small-signal model. **Right**: Comparison of the energy resolution for 6 keV pulses as a function of sensor heat capacity, calculated from the large-signal simulation (dotted) and the small-signal model (dashed). The filled circles are 5.9 keV X-ray measurements with X039 ($C = 0.59$ pJ/K) and two devices with smaller heat capacities [32].

with the calculated noise spectra at those set points, the expected energy resolution is calculated and plotted in figure 6.19 (left). The factor dE/dO is obtained from simulating two pulses very close in energy and noting the difference in output signal. The best resolution possible at 6 keV with these device parameters and filtering algorithm is calculated at 3.9 eV, as can be seen in the figure. With lower photon energies, better resolutions should be possible. This has not yet been demonstrated at SRON, but GSFC has shown 2.4 eV at 1.5 keV with a device with a similar heat capacity (0.5 pJ/K) as the devices discussed here [33]. This is consistent with the simulation.

When an $R(T)$-curve is used with a constant α, the calculated resolution is less dependent on the set point. For 6 keV X-rays and $\alpha = 50$, a best resolution of 3.2 eV is calculated. This shows that the figure for the best resolution calculated with this large-signal model does not depend greatly on the precise shape of the $R(T)$-curve that is chosen.

The large-signal model also tells us that increasing α and decreasing the heat capacity is not always advantageous for the resolution, as was suggested by the small signal model of section 2.4. For large pulses of 6 keV, the sensor is driven further towards the normal state and starts to saturate when the heat capacity is made smaller than 0.5 pJ/K, deteriorating the energy resolution. This is illustrated in figure 6.19 (right). In this plot, the energy resolution calculated from a simulation with a linear $R(T)$-curve of 50 Ω/K and

6 keV pulses is compared to the figures obtained from the small-signal model. While the small-signal resolution improves continually with smaller heat capacity, the large-signal resolution shows a clear optimum. The measured energy resolution at 5.9 keV for three sensors with different heat capacities is also plotted in the graph. They show a good agreement with the simple numerical model. This shows that the large-signal model can be used as a tool for finding the optimum design parameters for a microcalorimeter.

6.6   Conclusions

We conclude that the noise sources in this type of TES microcalorimeter are well understood. In addition to phonon and Johnson noise, an internal thermal fluctuation noise component adds a significant contribution to the current noise. This noise component can be manipulated and reduced by a change in geometry. It has not yet been established whether an improvement in resolution can be obtained in this manner. The measured energy resolution for 5.9 keV X-rays is understood in terms of the measured noise spectra and pulse shapes. Moreover, a numerical simulation has shown that the best obtainable resolution is about 3.9 eV at 6 keV, which has also been demonstrated experimentally. This model can be used to predict the energy resolution of a microcalorimeter from the device parameters. The simulation also indicates that for low energies (< 1 keV), a resolution of ~ 2.5 eV is feasible.

We can say that the physics of these devices is now sufficiently developed to consider using them in a real instrument. The implications of this are the topic of the following chapter.

CHAPTER 7

LOOKING AHEAD

Now that the TES microcalorimeter has shown to meet the requirements for the XEUS spectrometer, there are other issues to consider for using this technology in a space-borne instrument. In this chapter, we will look at a few of these in order to identify the criticalities involved in using a TES microcalorimeter in space.

7.1 Degradation over time

An effect that may occur in prolonged operation is degradation of the sensors over time. The bilayer materials, Ti and Au, may interdiffuse into each other, which could affect the superconduction transition. To see the magnitude of this effect, measurement of the transition was repeated after a long period of time for a few devices. One bilayer sample had been stored at room temperature under atmospheric conditions for more than 40 months and showed no degradation of the superconducting transition. Also, the transition of a complete sensor showed no adverse effects after storage for 18 months at room temperature: the transition temperature remained 0.1 K and the steepness did not decrease. Because they are thermally driven, it is expected that any interdiffusion effects will take place at a much slower rate if the devices are kept cold. Since this is the case in an instrument, we do not expect any degradation of the TES microcalorimeter over a reasonable instrument lifetime.

7.2 Proton radiation test

One of the problems with operating instrumentation in space is the exposure to cosmic radiation. Collision with cosmic particles may damage sensitive devices by causing interstitial defects. To test the radiation hardness of the TES microcalorimeter, device X048

was exposed to 6.4 MeV proton radiation at Birmingham University. The dose was equivalent to 20 times the expected irradiation of the EPIC instrument aboard XMM-Newton for ten years. No change was observed in the shape of the superconducting transition, so it is expected that the device incurred no permanent damage and that the performance is unaffected. However, the power plateau seemed to be slightly lower, which indicates a higher bath temperature or a worse coupling to the bath. A change in coupling to the bath could be caused by a damaged membrane, but it is unlikely that this is the case due to the small scattering cross-section of the silicon nitride. Therefore we think that the change in power plateau is not due to the proton irradiation. Since the superconducting transition has not changed, we can draw the preliminary conclusion that the TES microcalorimeter can be used in space without the risk of radiation degradation.

7.3   Towards an instrument

With the intrinsic requirements of stability and radiation hardness for using the TES microcalorimeter in a space-borne instrument likely to be met, we can look at the surrounding requirements for such an instrument. Of these, the most challenging are likely to be the use of an array of microcalorimeters, reading out such an array and the cryogenics involved in reaching the required low temperatures.

7.3.1   Microcalorimeter array

An array of microcalorimeters is desireable because it provides spatial information in addition to spectral information. For imaging purposes, an array of at least ~ 1000 pixels would be required. The difficulties with such an array are the uniform coupling to the heat bath of all pixels, the routing of the wiring to the pixels and the prevention of thermal and electrical cross-talk. If all pixels were placed on a single membrane, the pixels in the centre would have a lower thermal conductance to the bath than those closer to the edge. This non-uniformity in thermal conductance would create problems with the time constant and stability requirements of section 3.2. Also, since the energy of an absorbed photon is not completely compensated by electro-thermal feedback, the absorption of a photon in one pixel could be observed in neighbouring pixels, resulting in false counts. It is therefore desireable to have every pixel on its own, small membrane. Several schemes have been suggested to accomplish this, such as a membrane suspended over a small chamber in the silicon wafer [34], a membrane above the wafer supported by legs [35] or a row of membranes suspended between silicon bars [36]. These methods are currently under developement and it is not yet clear what the advantages and disadvantages of each are.

For the wiring, the challenge is to route wires for all the pixels over the wafer to the outside world. The wiring could be embedded in the substrate or, with overhanging

absorbers, underneath these along the surface. But for large arrays, there would probably still not be enough room for all the wiring. Alternatively, connections through the wafer to the back side, so-called micro-vias, have been suggested [37]. The contacts can then be bonded to a separate fan-out wafer, where there is enough space to route the wiring.

7.3.2 Multiplexing

If every pixel in an array were read out separately, this would require a very large number of SQUIDs and accompanying electronics. Moreover, all the separate wires connecting the cold stage to the room temperature electronics would cause a very high heat load on the cooler. Therefore, it is preferable to employ some sort of multiplexing scheme, reducing the number of wires and the amount of electronics. The most common schemes are time-division multiplexing (TDM) and frequency division multiplexing (FDM) [38, 39].

In TDM, different detector read-out channels are switched on and off, one after the other in quick succession. In this way, the signals of up to 32 microcalorimeters can be transported through a single line [40]. However, the switching produces fast-changing signals, so a large bandwidth is required. Bandwidth limitations in the electronics limit the switching rate, which means that for the fast pulses of the XEUS specification, the required sample rate will be hard to attain using TDM.

FDM does not have this drawback. This multiplexing scheme works by shifting the detector signals in the frequency domain to different carrier frequencies. The signals can then be transported through a single line and demodulated outside the cryostat. This scheme, however, requires the detectors to be operated under AC bias, which introduces problems of its own [41]. The TES is biased with an AC voltage with a period much faster than the time constant of the TES. This causes it to stay in a single set point with a certain temperature. However, because the current through the TES is constantly changing, α is changing as well. This makes the responsivity dependent on the phase of the bias voltage, which causes resolution degradation. This effect should become less pronounced with increasing bias frequency. Efforts are currently underway at SRON to attain the same energy resolution under AC bias as under DC.

7.3.3 Cooling

Although space is pretty cold, the operation of a cryogenic microcalorimeter there still requires extra cooling. Taking a dilution refrigerator up on a satellite is not practical, but there are alternatives. There is experience with using an ADR on a rocket in the XQC project [42]. This ADR, coupled to a liquid He bath, provides a stable ($\Delta T < 1 \ \mu K$) temperature of 60 mK for up to 12 hours. Although the duration of the rocket flight was only 10 minutes, the cooler performed well, and the technology can also be used on a satellite platform. When the hold time has run out, the ADR magnet can be recycled but the liquid He still runs out. ADR technology has been used for a longer duration on the

MAXIMA balloon-borne cosmic microwave background experiment [43]. For the ASTRO-E(2) satellite, an ADR has been developed as well [44]. Because it is surrounded by a block of solid Ne (17 K), its liquid He supply should last for two years. The satellite is scheduled for launch in February 2005.

An ADR employs a magnet generating a field typically of the order of 5 T. If this is not sufficiently shielded (below $\sim$ 1 G), the field might make the $R(T)$-curve of the TES less steep. The lower effective α which is the result will degrade the energy resolution and response time of the sensor. Also, since the field is changing in time, it will result in a time-dependent responsivity, which can also degrade the resolution. Therefore, it is important that the field is sufficiently attenuated using compensating coils and μ-metal shields.

The problem of having to recycle the ADR magnet every so often can be overcome by using a multiple-stage ADR in continuous operation. When one stage is providing the cooling power, another can be recycled, providing uninterrupted cooling. At GSFC, a three-stage continuous ADR is being developed for use in space [45]. The heat bath is provided by a mechanical cryocooler, so it can operate entirely without cryogenic substances. Provided that the magnetic fields are sufficiently shielded, this type of cooler would be ideal for operating an X-ray spectrometer based on TES microcalorimeters in space.

It looks as though the technology for fabricating, reading out and cooling microcalorimeter arrays is moving forward at a fast pace. We should expect to see this technology maturing in the next few years, enabling instruments based on TES microcalorimeters to be built and operated in space. This should open up a new chapter in X-ray astronomy, providing new insights into the beginning and the evolution of the universe.

APPENDIX A

SENSOR OVERVIEW

In this appendix, the characteristics of all the sensors mentioned in the text are summarised. A schematic top and section view of each sensor is shown, and the dimensions of TES and absorber are given, as well as the critical temperature T_c, the normal resistance R_n, the heat capacity C at T_c, the absorption efficiency A at 6 keV of the absorber/TES combination, the typical α under bias conditions as obtained from the $I(V)$-curve, the effective time constant τ_{eff} as obtained from observed X-ray pulses and the best measured energy resolution ΔE at 5.9 keV. Since all sensors were positioned on similar membranes, for each the G to the bath is 300–330 pW/K.

X037-2

TES	310 μm $\times$ 310 μm $\times$ 18 nm Ti/30 nm Au
Absorber	150 μm $\times$ 150 μm $\times$ 2.2 μm Cu
T_c	0.097 K
R_n	0.35 Ω
C	0.59 pJ/K
A	0.22
α	~ 100
$\tau_{\mathbf{eff}}$	200 μs
ΔE	4.2 eV

X038

TES	310 μm × 310 μm × 18 nm Ti/30 nm Au
Absorber	100 μm × 100 μm × 4.5 μm Cu
T_c	0.105 K
R_n	0.43 Ω
C	0.59 pJ/K
A	0.39
α	~ 80
$\tau_{\mathbf{eff}}$	85 μs
ΔE	3.9 eV

X043

TES	310 μm × 310 μm × 14 nm Ti/50 nm Au
Absorber	103 μm × 310 μm × 1.4 μm Cu
T_c	0.098 K
R_n	0.35 Ω
C	0.58 pJ/K
A	0.17
α	~ 40
$\tau_{\mathbf{eff}}$	85 μs
ΔE	4.9 eV

X047

TES	310 μm × 310 μm × 14 nm Ti/50 nm Au
Absorber	4 × 34 μm × 320 μm × 1.0 μm Cu
T_c	0.098 K
R_n	0.26 Ω
C	0.56 pJ/K
A	0.14
α	~ 20
$\tau_{\mathbf{eff}}$	270 μs
ΔE	8–9 eV

X048

TES	310 μm $\times$ 310 μm $\times$ 14 nm Ti/50 nm Au
Absorber	100 μm $\times$ 100 μm $\times$ 4.1 μm Cu
T_c	0.098 K
R_n	0.22 Ω
C	0.54 pJ/K
A	0.37
α	N/A
τ_{eff}	80 μs
ΔE	4.7 eV

X049

TES	310 μm $\times$ 310 μm $\times$ 14 nm Ti/50 nm Au
Absorber	100 μm $\times$ 100 μm $\times$ 4.1 μm Cu
	100 μm $\times$ 100 μm $\times$ 3.4 μm Bi
T_c	0.102 K
R_n	0.20 Ω
C	0.55 pJ/K
A	0.88
α	~ 100
τ_{eff}	100 μs
ΔE	4.5 eV

X051-3

TES	310 μm $\times$ 310 μm $\times$ 14 nm Ti/50 nm Au
Absorber	160 μm $\times$ 160 μm $\times$ 1.8 μm Cu
	160 μm $\times$ 160 μm $\times$ 5.1 μm Bi
	(base 100 μm $\times$ 100 μm)
T_c	0.081 K
R_n	0.20 Ω
C	0.64 pJ/K
A	0.93
α	N/A
τ_{eff}	110 μs
ΔE	5.7 eV

X052-1

TES	310 μm $\times$ 310 μm $\times$ 14 nm Ti/50 nm Au
Absorber	100 μm $\times$ 100 μm $\times$ 4 μm Cu
Ground plane	500 μm $\times$ 500 μm $\times$ 1.0 μm Al
T_c	0.092 K
R_n	0.22 Ω
C	0.53 pJ/K
A	0.36
α	N/A
τ_{eff}	N/A
ΔE	N/A

X055-6

TES	310 μm $\times$ 310 μm $\times$ 14 nm Ti/50 nm Au
Absorber	100 μm $\times$ 100 μm $\times$ 4.5 μm Cu
Ground plane	500 μm $\times$ 500 μm $\times$ 0.7 μm Nb
T_c	0.084 K
R_n	0.27 Ω
C	0.58 pJ/K
A	0.40
α	~ 30
τ_{eff}	260 μs
ΔE	4.7 eV

Appendix B

Filtering

The signal from our X-ray microcalorimeter consists of pulses that are contaminated by noise. From these pulses, we want to estimate the energy of the X-rays that produced them as accurately as possible. For an optimum detector resolution, the signal-to-noise ratio should be maximized. This can be accomplished by means of filtering which is therefore an essential part in the analysis of these X-ray pulses.

In what follows, we review the principles of filtering and compare the performance of real-time analog filtering and 'optimum' (digital) filtering. Digital filtering has the advantage of being able to use an non-causal filter, that is a filter that obtains a better signal-to-noise ratio because it uses information not only from the present and the past signal, but the total signal. The effect of filtering is demonstrated in a general way assuming exponential pulses with zero rise time.

B.1 Principles of filtering

The purpose of filtering is to optimise the signal-to-noise ratio of the measured data. For this purpose, a number of techniques have been developed. Using analog electronic circuits with a frequency response that is tuned to the type of signal and noise to be filtered, good results can be obtained in real time. An example of this is the analog shaping described in section B.2. More elaborate data manipulation is possible using off-line processing. This requires the signal to be digitized using a data-acquisition system. In doing so, a number of issues deserve attention.

First of all, the Nyquist-criterion states that a sampled signal contains meaningful information up to a frequency f_c that is half the sampling frequency f_s. The sampling frequency should therefore be at least double the highest frequency present in our signal.

Secondly, a signal with frequency $f > f_c$ will be folded around f_c and introduce an alias signal at frequency $|f_s - f|$. So, in order to prevent higher frequencies from contam-

inating the sampled data, an anti-aliasing filter should be used with a corner frequency lower than $f_c = f_s/2$.

Thirdly, to characterise the frequency dependence of a signal or noise the power spectral density is used. Knowing the power spectral density of the noise for example, enables us to correct for this noise and improve the signal-to-noise ratio. To get our data in the frequency domain, we use the discrete Fourier transform [46] for n sampled data points c_j:

$$C_k = \sum_{j=0}^{n-1} c_j e^{-2\pi i jk/n} \quad k = 0,\ldots,n-1 \tag{B.1}$$

Information about how much power there is at a certain frequency $f_k = k/(n\Delta)$, with Δ the sampling interval, is given by the single-sided power spectral density:

$$\text{PSD}(f_k) = \frac{\Delta}{n} \left(|C_k|^2 + |C_{n-k}|^2 \right) \quad k = 1, 2, \ldots, \frac{n}{2} - 1 \tag{B.2}$$

Single-sided means that the signal or noise is only defined for positive frequencies. Note that noise levels are often given in terms of the square root of $\text{PSD}(f)$, in units of, for example V/$\sqrt{\text{Hz}}$.

In general, we consider a signal $S(t) = A \cdot S_0(t)$ in time, of which the shape $S_0(t)$ is known, but the amplitude A is not. In frequency space, the Fourier transform $\overline{S}(f)$ is used. As an example, we assume that the signal is expressed in Volts. Added to the signal is noise, with a single-sided power spectral density of $N^2(f)$ [V^2/Hz]. The noise is usually given only in the frequency domain, because of its random characteristic in the time domain. Now, in general a filter $F(t)$ (or $\overline{F}(f)$ in the frequency domain) works both on the signal and the noise [47]:

$$\begin{array}{ccc} S_{\text{in}}(t),\ \overline{S}_{\text{in}}(f) & \boxed{\begin{array}{c} F(t) \\ \hline \overline{F}(f) \end{array}} & S_{\text{out}}(t),\ \overline{S}_{\text{out}}(f) \\ N_{\text{in}}(f) & \longrightarrow \qquad \longrightarrow & N_{\text{out}}(f) \end{array}$$

In the time domain, the filter is convolved with the signal, which is equivalent to a multiplication in the frequency domain. The filtered signal at time t is the input signal multiplied by the filter in the frequency domain and Fourier transformed back to the time domain:

$$S_{\text{out}}(t) = \int_{-\infty}^{\infty} \overline{S}_{\text{in}}(f)\overline{F}(f)e^{2\pi i ft}df, \tag{B.3}$$

The noise is multiplied in the frequency domain by the same filter. The total noise power integrated over all positive frequencies, which is stationary in time, is by virtue of Parseval's theorem given by

$$N_{\text{out}}^2 = \int_0^{\infty} |\overline{F}(f)|^2 N_{\text{in}}^2(f)df. \tag{B.4}$$

Note that N_{out} is not a noise density, but a root-mean-square (RMS) value, in units of Volts in our example. Noise *power* (noise squared) is used here because the noise itself
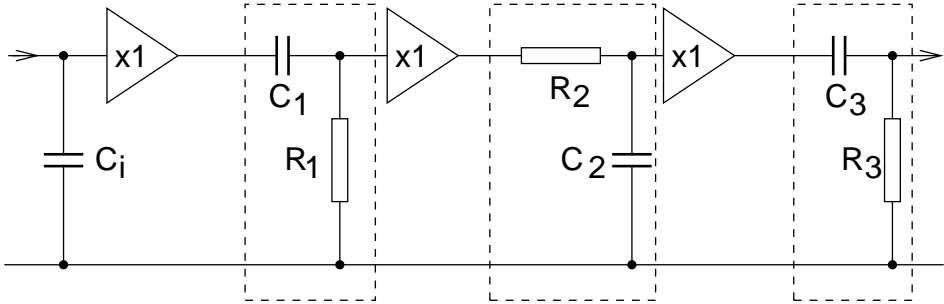
Figure B.1: Equivalent circuit for $(CR)^2RC$ filtering. The circuit consists of an input integrator and a highpass filter, a lowpass filter and another highpass filter, as indicated by the dashed boxes. The time constant for each part is the product of its resistance and capacitance.

scatters around zero, so integrating it would yield zero. For the purpose of calculating the signal-to-noise ratio, the square root of this integral is used. So, for the signal-to-noise ratio S/N after filtering at a certain time t we have

$$\left(\frac{S}{N}\right)(t) = \frac{\int_{-\infty}^{\infty} \overline{S}_{\text{in}}(f)\overline{F}(f)e^{2\pi i f t}df}{\sqrt{\int_{0}^{\infty} |\overline{F}(f)|^2 N_{\text{in}}^2(f)df}}. \tag{B.5}$$

This result is valid independent of the type of filtering used. Based on this relation we will consider the performance of two types of filter: The analog $(CR)^2RC$ filter and the digital 'optimum' (Wiener) filter.

B.2 $(CR)^2RC$ filtering

The first type of filtering that is considered is $(CR)^2RC$ shaping [48], or 'double RC differentiation', which consists of an input integrator, two highpass filters and a lowpass filter, as shown in figure B.1. This system combines a reasonable performance with a quick return to the base line. If the filters all have the same time constant τ, the transfer function of this system has the form

$$\overline{F}(f) = \frac{2\pi i f \tau}{(1 + 2\pi i f \tau)^3}. \tag{B.6}$$

We will calculate the response of this filter to an exponential pulse $I(t) = I_0 \exp(-t/\tau)$, as shown in figure B.2 (left). The Laplace transform of this pulse is
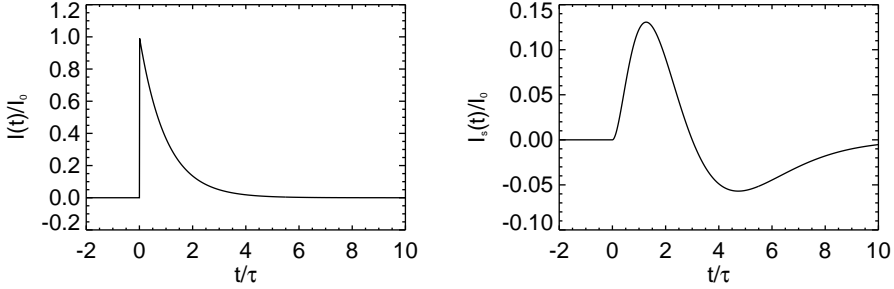
Figure B.2: **Left**: exponential pulse with normalised amplitude and fall time. **Right**: response of the $(CR)^2RC$ filter to the exponential pulse. The maximum and minimum are at $t/\tau = 3 \pm \sqrt{3}$ and the zero crossing is at $t/\tau = 3$

$$\bar{I}(s) = \frac{I_0\tau}{1+s\tau}, \tag{B.7}$$

with $s = \sigma + 2\pi i f$. The Laplace transform is used here because the signal is zero for $t < 0$. If we neglect the damping and use the convention $s = 2\pi i f$, then the Laplace transform of a function can be considered equivalent to its Fourier transform, except that the Laplace transform can deal with functions that are zero for $t < 0$. The pulse in the frequency domain is then

$$\bar{I}(f) = \frac{I_0\tau}{1+2\pi i f\tau}. \tag{B.8}$$

Applying the filter, we get

$$\bar{F}(f)\bar{I}(f) = \frac{I_0 2\pi i f\tau^2}{(1+2\pi i f\tau)^4} \tag{B.9}$$

$$= \frac{I_0}{\tau^2}\frac{2\pi i f}{(1/\tau+2\pi i f)^4}. \tag{B.10}$$

This can be transformed back to the time domain to a shaped pulse $I_s(t)$:

$$I_s(t) = \frac{I_0}{\tau^2}\left(\frac{-1}{\tau}\frac{t^3}{6}e^{-t/\tau} + \frac{t^2}{2}e^{-t/\tau}\right). \tag{B.11}$$

The output of the filter is shown in figure B.2 (right). The maximum of this shaped pulse is used as a measure for the integral of the original pulse. Setting $dI_s(t)/dt = 0$ gives the solutions $t/\tau = 3 \pm \sqrt{3}$ (and $t = 0$). This yields for the maximum of the shaped pulse

$S = I_s \left(\left(3 - \sqrt{3}\right) \tau \right) = \left(2\sqrt{3} - 3\right) I_0 e^{\sqrt{3}-3} \approx 0.1306 I_0$. For the total noise power we have, assuming a white noise level N_{white},

$$N^2 = \int_0^\infty N_{\text{white}}^2 |\overline{F}(f)|^2 df \tag{B.12}$$

$$= N_{\text{white}}^2 \int_0^\infty \left| \frac{2\pi i f \tau}{(1 + 2\pi i f \tau)^3} \right|^2 df \tag{B.13}$$

$$= \frac{N_{\text{white}}^2}{32\tau} \tag{B.14}$$

For the signal-to-noise ratio, we obtain

$$\frac{S}{N} = \frac{0.7388 I_0 \sqrt{\tau}}{N_{\text{white}}}. \tag{B.15}$$

This expression can be used to compare this filter to others.

B.3   'Optimum' filtering

The second method of filtering we will look into makes use of the so-called 'optimum' or Wiener filter, described in [46]. This is actually a whole class of filters that share the property that they are constructed for a certain signal shape by finding the maximum of a specific quantity, for instance the signal-to-noise ratio.

When the noise is not frequency-independent, in order to use 'optimum' filtering we must take this noise into account when constructing our filter. Therefore, the filter must be constructed in the frequency domain and transformed back to the time domain using the inverse discrete Fourier transform. In the frequency domain, the filter has the form [49]

$$\overline{F}(f) = \frac{\overline{S}^*(f)}{(N(f))^2} \tag{B.16}$$

where $\overline{S}^*(f)$ is the complex conjugate of the Fourier transform of the pulse shape and $(N(f))^2$ is the power spectral density of the noise. To find this PSD, a number of records should be sampled that have only noise in them. The PSD can then be found as given by (B.2) for these noise records and averaged. The expression (B.16) is different from the one given in [46], in the sense that the expression in [46] tries to reconstruct the original signal as well as possible, while the expression given here maximizes the signal-to-noise ratio.

B.3.1   Optimum filter with white noise

Though the optimum filter is generally constructed in the frequency domain, it is easily seen that if the noise is assumed to be frequency-independent, then the filter in the time

domain is exactly the same shape as the signal pulse, but time-reversed. In the case of exponential pulses, the maximum of the convolution integral is at $t = 0$, where it is simply equal to the integral of the product of filter and pulse. Thus, under the assumption of white noise and exponential pulses, 'optimum' filtering just involves multiplying the signal with a function $F(t) = \exp(-t/\tau)$ and integrating. In practice, the average of a set of pulses is used for the filter template.

It is attractive to construct the filter in the time domain even when the noise may not be white, because no information about the noise spectrum is required. In order to get an idea of the resolution degradation that is the result of the assumption of white noise, we will compare the signal-to-noise ratio of the 'optimum' filter with and without taking the noise into account, for a typical noise spectrum such as shown in figure 6.1. On the one hand, the signal-to-noise ratio is calculated using a filter based on an exponential pulse with a 150 μs time constant and a fit to the noise spectrum of figure 6.1. On the other hand, the signal-to-noise ratio is calculated using a filter that is based just on the exponential pulse and assumes white noise. The ratio of these signal-to-noise ratios was 0.85, which means a 15% degradation in resolution when white noise is assumed compared to a proper optimum filter. This is a significant loss, but the noise data necessary for a true optimum filter is hard to come by during X-ray resolution measurements. Therefore, in general the 'optimum' filter that assumes white noise is used.

To compare this filter with the $(CR)^2RC$ filter, we will calculate the signal-to-noise ratio using exponential pulses and white noise. The integrated signal is

$$S = \int_0^\infty I_0 e^{-t/\tau} e^{-t/\tau} dt = \frac{I_0 \tau}{2} \tag{B.17}$$

The noise power still has to be calculated in frequency space. Therefore, we use the complex conjugate of the Laplace transform of the ideal pulse:

$$\overline{F}(f) = \frac{\tau}{1 - 2\pi i f \tau} \tag{B.18}$$

The noise then yields:

$$N^2 = \int_0^\infty N_{\text{white}}^2 |\overline{F}(f)|^2 df \tag{B.19}$$

$$= N_{\text{white}}^2 \int_0^\infty \left| \frac{\tau}{1 - 2\pi i f \tau} \right|^2 df \tag{B.20}$$

$$= \frac{N_{\text{white}}^2 \tau}{4} \tag{B.21}$$

Then, the signal-to-noise ratio of the filtered signal becomes

$$\frac{S}{N} = \frac{2 I_0 \tau}{2 N_{\text{white}} \sqrt{\tau}} = \frac{I_0 \sqrt{\tau}}{N_{\text{white}}}, \tag{B.22}$$

which is a factor ~ 1.35 better than $(CR)^2RC$ filtering. It is clear that digital processing offers a large advantage. The drawback is that it does not provide information during the measurement, only afterwards. Therefore, we often use the analog $(CR)^2RC$ processing as a 'quick-look' facility, and make a final measurement for digital processing.

In what follows, a number of algorithms are described that are used to obtain the best possible resolution in practical, non-ideal conditions.

B.3.2 Pile-up rejection

Pile-up is the effect of one pulse influencing the next. This may cause resolution degradation . The magnitude of this effect can be calculated analytically. For simplicity, we will consider only pulses of equal energy. A pulse normalised to amplitude and fall time can be described by

$$p(t) = e^{-t}. \tag{B.23}$$

A pulse $q(t)$ occuring Δt earlier in time is described by

$$q(t) = p(t + \Delta t). \tag{B.24}$$

Pulse p will be superimposed on the tail of q, so the integral of their sum after filtering will be slightly larger compared to a pulse without a precursor. Since this addition to the integral depends on the time elapsed since the previous pulse, it will cause a smearing of the spectrum. Here, the filter is assumed to be equal to an ideal pulse $p(t)$, so the integral becomes

$$\int_0^\infty p(t)(p(t) + q(t))dt = 0.5\left(1 + e^{-\Delta t}\right), \tag{B.25}$$

whereas the integral of a single pulse after filtering is just 0.5. Therefore, the relative contribution to the integral is

$$c(\Delta t) = e^{-\Delta t}. \tag{B.26}$$

Now, a pile-up rejection system makes sure that there is a minimum Δt between two pulses by rejecting pulses that are too close to their precursor. With a typical chosen interval of 10 fall times, the relative contribution to the pulse integral will lie between zero and $\exp(-10)$. The absolute contribution for 5.9 keV X-rays will be between zero and 0.27 eV. It is clear that the energy resolution will not be impaired.

But what fraction of the pulses are rejected in this way? To answer that, we need to look at the distribution of time intervals Δt. This distribution follows from the Poisson distribution of random events:

$$P(x, \Delta t) = e^{-\Delta t \lambda} \frac{(\Delta t \lambda)^x}{x!} \tag{B.27}$$

is the probability of x events occuring in a time interval Δt, when the average number of events per time interval equals λ. Now, we are looking for the distribution of time intervals *between* two pulses; in other words the probability of finding *zero* events in the time interval:

$$P(0, \Delta t) = e^{-\Delta t \lambda} \tag{B.28}$$

With the proper normalisation this becomes

$$P(\Delta t) = \lambda e^{-\Delta t \lambda}. \tag{B.29}$$

So, the fraction of rejected pulses using a minimum time interval $\Delta t_{\min}$ is

$$\int_0^{\Delta t_{\min}} P(\Delta t) d\Delta t = 1 - e^{-\Delta t_{\min} \lambda}. \tag{B.30}$$

Substituting the $\Delta t_{\min}$ of 10 fall times that we mentioned above, this is about 2% for a typical count rate of 20 s^{-1} and a 100 μs fall time, which is no problem for our test setup. However, for a count rate of 100 s^{-1}, the rejected fraction is 10%, already a sizeable portion. Therefore, for higher count rates, we would like to use a smaller value of $\Delta t_{\min}$. To see how small we can make $\Delta t_{\min}$ without impairing the energy resolution, we need to find the distribution of contributions $c(\Delta t)$ to the measured energy. This is done by solving Δt from (B.26) and substituting it into the time interval distribution function (B.29):

$$P(c) = -P(\Delta t(c)) \frac{d\Delta t}{dc} \tag{B.31}$$

$$= \lambda c^{\lambda - 1}, \tag{B.32}$$

where the minus sign is due to the fact that a large Δt corresponds to a small c, and that therefore the integration limits are switched. Integration over c from 0 contribution (pulses infinitely far apart) to 1 (pulses exactly on top of each other) shows that the distribution is properly normalised. The maximum contribution to the pulse integral that corresponds to the minimum time interval $\Delta t_{\min}$ is $c_{\max} = e^{-\Delta t_{\min}}$. This is where the distribution is cut off by the pile-up rejection system.

We now have the distribution of contributions as a function of count rate. The average contribution is

$$\langle c \rangle = \frac{\int_0^{c_{\max}} c P(c) dc}{\int_0^{c_{\max}} P(c) dc} \tag{B.33}$$

$$= \frac{\lambda}{\lambda + 1} e^{-\Delta t_{\min}}. \tag{B.34}$$

But a contribution to the pulse integral in itself does not cause resolution degradation. It is the *spread* in the contributions that causes the degradation. Therefore, the standard

deviation of this distribution is a measure of the magnitude of this effect. The standard deviation is

$$\sigma = \sqrt{\frac{\int_0^{c_{max}}(c - \langle c \rangle)^2 P(c)dc}{\int_0^{c_{max}} P(c)dc}} \tag{B.35}$$

$$= \sqrt{\frac{\lambda}{(\lambda+1)^2(\lambda+2)}e^{-\Delta t_{min}}}. \tag{B.36}$$

This should be scaled to the energy of the pulses and multiplied by 2.35 to get a FWHM contribution to the resolution; for Mn Kα_1 pulses:

$$\Delta E_{pile-up} = 2.35 \times 5899 \times \sigma \tag{B.37}$$

Note that the count rate λ should be expressed in terms of the reciprocal fall time while the minimum time between pulses Δt_{min} should be expressed in terms of the fall time. There is a clear trade-off between count rate, rejected fraction and resolution contribution. An example for a 1 eV resolution contribution at 5.9 keV was shown in figure 4.3 in the main text.

It should be noted that when the shape and the arrival time of the previous pulse is known exactly, the effect of pile-up can be completely removed and no pulse rejection is necessary. This, however, requires a very detailed pulse model and advanced signal processing. The method using a minimum time interval is much simpler.

The pile-up rejection is accomplished in practice by including in the event record a number of samples acquired just before the pulse starts, so-called 'pretrigger samples'. The duration of this pretrigger phase should be adjusted to the desired minimum time between pulses. Event records that contain a pulse in the pretrigger phase are rejected, as well as records that contain a second pulse after the one that triggered the acquisition. This ensures that every event included in the spectrum is a 'clean' one, not contaminated by other pulses.

B.3.3 Base line restoration

Due to slow changes in amplifier offsets or other effects, the quiescent signal level may not be constant. Since the $(CR)^2RC$ filter is AC-coupled, it is not very sensitive to these 'base line shifts', but if we use the 'optimum' filter they degrade the resolution and should be corrected. This can be done by subtracting a constant value from the filter before applying. The filter then becomes

$$F(t) = e^{-t/\tau} - c \tag{B.38}$$

where c is the subtracted constant. This value should be chosen in such a way that the integral of the filter vanishes. In that case, any base line shifts are corrected. If we work

with a record length t_l that is a couple of times longer than τ, we see that:

$$\int_0^{t_l} e^{-t/\tau} dt - c t_l \;\; = \;\; 0 \tag{B.39}$$

$$c \;\; \approx \;\; \frac{\tau}{t_l} \tag{B.40}$$

In practice, the value c is computed using

$$c = \frac{1}{n} \sum_{j=0}^{n-1} c_j \tag{B.41}$$

from n samples denoted $c_0 \ldots c_{n-1}$. The pulse is modelled as

$$I(t) = I_0 e^{-t/\tau} + b \tag{B.42}$$

where b is the unknown base line shift. When the filter is applied, we get

$$S_{\text{blr}} \;\; = \;\; \int_0^{t_l} F(t) I(t) dt \tag{B.43}$$

$$= \;\; \int_0^{t_l} \left(I_0 e^{-2t/\tau} + (b - c I_0) e^{-t/\tau} - bc \right) dt \tag{B.44}$$

$$\approx \;\; \frac{I_0 \tau}{2} - \frac{I_0 \tau^2}{t_l} \tag{B.45}$$

The unknown b has indeed vanished, but the integral is smaller by a factor of $1 - 2\tau/t_l$. For the noise, we use the complex conjugate Laplace transform of the shifted filter:

$$\overline{F}(f) = \frac{\tau}{1 + 2\pi i f \tau} + \frac{c}{2\pi i f} \tag{B.46}$$

With a record length of t_l, the lowest frequency present in the signal is $1/2\pi t_l$. We now calculate

$$N_{\text{blr}}^2 \;\; = \;\; \int_{1/2\pi t_l}^{\infty} N_{\text{white}}^2 |\overline{F}(f)|^2 df \tag{B.47}$$

$$= \;\; N_{\text{white}}^2 \int_{1/2\pi t_l}^{\infty} \left| \frac{\tau}{1 - 2\pi i f \tau} + \frac{c}{2\pi i f} \right|^2 df \tag{B.48}$$

$$\approx \;\; \frac{N_{\text{white}}^2 \tau}{4} \left(1 - \frac{2}{\pi} \arctan \frac{\tau}{t_l} - \frac{2\tau}{t_l} + \frac{4\tau}{\pi t_l} \arctan \frac{\tau}{t_l} + \frac{2\tau}{\pi t_l} \right) \tag{B.49}$$

$$= \;\; \frac{N_{\text{white}}^2 \tau}{4} \cdot d, \tag{B.50}$$

with d the expression in brackets in (B.49). This yields for the signal-to-noise ratio

$$\left(\frac{S}{N}\right)_{\text{blr}} = \left(\frac{I_0\sqrt{\tau}}{N_{\text{white}}} - \frac{2I_0\tau^{3/2}}{N_{\text{white}}t_l}\right)\frac{1}{\sqrt{d}} \tag{B.51}$$

$$= \frac{S}{N} \cdot \left(1 - \frac{2\tau}{t_l}\right)\frac{1}{\sqrt{d}}. \tag{B.52}$$

This expression gives the factor with which the resolution is degraded when this type of base line restoration is used. For typical values of $\tau = 200\ \mu$s and $t_l = 4096\ \mu$s, it results in a degradation of the resolution of $\sim 5\%$. This method should therefore only be used when the expected degradation by base line shifts is more than 5%.

B.3.4 Timing correction

A problem with using the 'optimum' filter in the time domain is that it is quite sensitive to how well the filter is lined up with the pulse. Due to a finite sampling interval in the data-acquisition, the arrival time of each pulse is slightly different with respect to the time bin divisions. To correct for this, we would like to shift the filter slightly in time before applying it to the pulse, so that it lines up well and the integral of the filtered pulse yields a maximum. However, since the filter is constructed from the sampled pulses, it too has a finite time resolution. Shifting the filter less than the duration of one time bin requires interpolating between the points, which might be complicated. Another possibility is to repetitively shift the filter an integer number of time bins and use a least-squares approximation to estimate the integrals of the shifts in-between. For example, the filter is applied 5 times, shifted -2, -1, 0, 1, and 2 time bins, respectively. Then, a parabola $y = a_2x^2 + a_1x + a_0$ is fitted through the integrals, as shown in figure B.3. The top of the parabola, as given by $y_{\text{max}} = -a_1^2/4a_2 + a_0$, is a good approximation of the integral with a filter that is properly lined up.

B.3.5 Gain drift correction

Gain drift arises when the amplifier gain is changing over time during the measurement. This causes the spectrum to be smeared and the resolution to be degraded. It can be compensated by selecting events that belong to a narrow spectral line and calculating a moving average of their energy as function of time. When the moving average is normalised to the total average, it can be used as a correction factor for all events. In this way, most of the gain drift can be eliminated. For the spectral line, a calibration line in the measured spectrum or a line due to a heat pulser can be used. The measured energies in this spectral line have a certain error, so applying the gain correction introduces some extra resolution degradation. If the gain correction is to help more than it hurts, sufficient averaging is necessary. This reduces the error in the correction factor with the square root
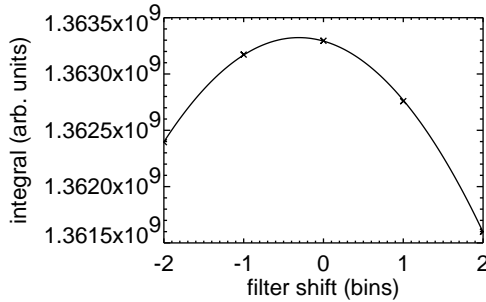
Figure B.3: Integrals of shifted filter applied to X-ray pulse ($\times$) with fitted parabola (solid line).

of the number of points to be averaged. The minimum number of points is dictated by the width of the spectral line used. If the line has a very narrow intrinsic width (as with a heat pulser line), its width in the spectrum is equal to the energy resolution. For the gain drift correction to contribute no more than 20% to the resolution, we need to average over at least $1/0.2^2 = 25$ points. When the spectral line has a larger instrisic width ΔE_{int}, the minimum number of points for a 20% contribution is

$$n = 25 + 25 \frac{\Delta E_{\text{int}}^2}{\Delta E^2}. \tag{B.53}$$

So, when the Mn Kα complex is used for the gain drift correction, with an intrinsic line width of ~ 15 eV, then for a 20% contribution to a 5 eV resolution, a moving average over 250 points is necessary. Of course, when the gain varies on a shorter time scale, it may well be that using a lower number of points is preferred. Some experimentation is necessary to find the optimum number of points for a given dataset.

B.4   Peak fitting

After filtering, the calculated photon energies are plotted in a histogram. In order to calculate the measured resolution, it is necessary to compare the measured spectrum with the intrinsic spectral shape. To do so, the intrinsic spectrum (as obtained from e.g. a very-high-resolution crystal spectrometer) is convolved with an instrument response that is assumed to be Gaussian. The convolved spectrum is then fitted to the measurements, and the width of the Gaussian that produced the best fit is the energy resolution of the spectrometer. For the fitting, a weighted least-squares procedure is used. The weights are $1/\sigma^2$ with σ the error in the data. For the Poisson statistics of our histogram, the error

is the square root of the number of counts, so the weight of a bin is the inverse of the number of counts in that bin. The fitting is performed in two stages: in the first stage, the weights are based on the measured number of counts. Bins with zero counts get a weight of 1. In the second stage, the weights are based on the fitted curve from the first stage. This ensures that the weighting is based on the spectrum as it should be, given a certain instrument response width, and not as it was measured. The energy resolution obtained in this way is a good measure for comparing the quality of spectrometers.

APPENDIX C

TES SIMULATION WITH SABER

This appendix describes the technical details of the TES noise simulation using the Saber program from Synopsys, Inc. The program requires input in the form of text files called *templates*. These templates are written in the MAST language. A hierarchical structure of components can be described and equations governing the behaviour of each component can be specified. Each component has a number of connections to other components called *pins*. These pins all have a specific type, for instance electrical or thermal. The equations should specify the "flow" from one pin to another (so-called "through" variables) in terms of the "potential" between those pins (so-called "across" variables). For example, a thermal conductance has two pins, labelled *a* and *b*. The through variable for this component is power (P) and the across variable is temperature (T). Each pin has its own temperature, and the equation describing the power flow from pin *a* to pin *b* is:

$$P_{a \to b} = G(T_a - T_b), \tag{C.1}$$

where G is the value for the thermal conductance. In some cases, the through variable cannot be expressed directly, and another equation is necessary. For instance in an ideal voltage source, the through variabele current (I) is not known as it depends on the load. The simulator has to solve the system of equations to find the current. This is specified as follows:

$$I_{a \to b} = I \tag{C.2}$$
$$I : V_a - V_b = V_s \tag{C.3}$$

This means that the simulator should find the I that makes the voltage between the two pins equal to the specified source voltage V_s.

Noise can be specified as a spectral density level for either a through variable (e.g. current noise between two pins) or an across variable (e.g. voltage noise). In each simulation element, noise sources are included. The simulator can then calculate and plot the

Table C.1: Components used in the numerical noise simulation.

Component	Parameters	Electrical pins	Thermal pins	Equations
Voltage source	V_s	p, m		$V_p - V_m = V_s$
Resistor	R	p, m		$I_{p \to m} = (V_p - V_m)/R$
Inductor	L	p, m		$V_p - V_m = L\, dI/dt$
Temperature source	T_s		p, m	$T_p - T_m = T_s$
Heat capacity	C, T_{init}		p	$P_p = C\, dT/dt$
Thermal conductor	G		p, m	$P_{p \to m} = G(T_p - T_m)$ $\delta P_{p \to m} = \sqrt{4 k_B G}(T_p + T_m)/2$
Thermal conductor with gradient	G		p, m	$P_{p \to m} = G(T_p - T_m)$ $\delta P_{p \to m} = \sqrt{4 \gamma k_B G T_p}$
TES thermometer	α, R_n, T_c	p, m	t	$R = R_n (T_t/T_c)^{\alpha}$ $I_{p \to m} = (V_p - V_m)/R$ $P_t = -(V_p - V_m)^2/R$ $\delta V_m = \sqrt{4 k_B T_t R}$

contribution of each noise source to a selected quantity, e.g. current or power. Also, the current noise spectrum of the total sensor can be plotted.

For the TES simulation, the components specified in table C.1 were designed. The actual MAST code is given at the end of this appendix. The basis for the TES thermometer component is the expression for the temperature dependence of the resistance. For reasons of simplicity, an expression has been chosen in which the value of the parameter α is independent of the set point in the transition:

$$R(T) = \begin{cases} R_n \left(\dfrac{T}{T_c} \right)^{\alpha} & \text{for } T \leq T_c \\ R_n & \text{for } T > T_c \end{cases} \tag{C.4}$$

The fact that in reality, α is generally not constant over the whole transition, is of little concern since we are only looking at the noise in a single set point. A constant α allows easy comparison of the noise in different sensor layouts.

The thermal conductor is implemented in two ways: The first has the noise based on the average temperature on both ends and should be used when there is only a small temperature difference across the link, as is the case inside the microcalorimeter. The

other should be used when there is a large temperature gradient across the heat link, for example in the membrane. Its noise is based on the temperature on the warm end, but contains a factor γ which corrects for the effect of the temperature gradient. Since $n \approx 3.2$, we get $\gamma \approx n/(2n+1) \approx 0.43$.

The Johnson noise in the TES has two effects: it adds directly to the noise in the electrical system which dissipates in the TES resistor and adds power to the thermal system, but the work done by the noise source itself also removes power from the thermal system. To implement this in a correct manner, the TES thermometer component was split into two parts: a noiseless, temperature-dependent resistor generating a power of $P_1 = I^2 R(T)$ in series with a noise source generating $P_2 = \Delta V_2 I$, where ΔV_2 is the voltage across the noise source. Variations in these powers have an opposite sign. The sum of these two powers being put into the thermal system results in the correct current noise spectrum in the electrical system.

Since we are interested in the noise from the microcalorimeter itself, the shunt resistor is kept noiseless.

Below, the program code for the MAST templates used in the numerical noise simulation as described in section 6.4 is included. A multi-element one-dimensional simulation consisted of a number of `tes` instances in series, terminated by a `teselement` instance, together with the components for providing the non-ideal bias voltage (`voltage` and two `resistors`) and an `inductor` to simulate the SQUID inductance. For the two-dimensional simulations, a grid of `tes2d` instances was used, terminated by `tes` instances and one `teselement`.

```
# Thermal conductivity with power noise based on the average
# temperature of the two pins.
element template thermcond p m = g
thermal_k p,m
number g                    # thermal conductivity coefficient
{
  number k = 1.3807e-23    # Boltzmann's constant
  val nw noise              # power noise
  values {
    noise = sqrt(4.0*k*g)*(tk(p)+tk(m))/2.0
  }
  control_section {
    noise_source (noise, p, m)
  }
  equations {
    p(p->m)+=g*(tk(p)-tk(m))
  }
}
```

```
# Thermal conductivity with temperature gradient. Noise based on
# temperature of p pin.
element template thermcond_gradient p m = g
thermal_k p,m
number g                      # thermal conductivity coefficient
{
  number k = 1.3807e-23    # Boltzmann's constant
  val nw noise              # power noise
  values {
    noise = sqrt(0.43*4.0*k*g)*tk(p)
  }
  control_section {
    noise_source (noise, p, m)
  }
  equations {
    p(p->m)+=g*(tk(p)-tk(m))
  }
}
```

```
# Heat capacity with initial temperature
element template heatcap p = c, ti
thermal_k p          # just one pin, the other always to ground
number c             # heat capacity
number ti = undef    # initial temperature
{
  val tk t           # temperature
  values {
    t = tk(p)
  }
  control_section {
    initial_condition(t,ti)
  }
  equations {
    p(p)+=d_by_dt(c*t)
  }
}
```

```
# Constant temperature source to be used as heat bath
element template tempsource p m = t
thermal_k p,m
number t          # temperature difference
```

```
{
  var p x
  equations {
    p(p->m)+=x
    x: tk(p)-tk(m)=t
  }
}
```

```
# Ideal inductor
element template inductor p m = l
electrical p, m
number l        # inductance
{
  var i il
  equations {
    i(p->m)+=il
    il: v(p)-v(m)=d_by_dt(l*il)
  }
}
```

```
# Ideal electrical resistor
element template resistor p m = r
electrical p,m
number r          # resistance
{
  equations {
    i(p->m)+=(v(p)-v(m))/r
  }
}
```

```
# Ideal constant voltage source
element template voltage p m = vs
electrical p,m
number vs           # voltage
{
  var i x
  equations {
    i(p->m)+=x
    x: v(p)-v(m)=vs
  }
}
```

```
# TES thermometer; temperature dependent, dissipates heat and
# generates Johnson noise.
element template testherm p m t = alpha, rn, tc
electrical p,m
thermal_k t                # thermal connection
number alpha               # coefficient of steepness
number rn                  # normal resistance
number tc                  # critical temperature
{
  number k = 1.3807e-23    # Boltzmann's constant
  val r res                # resistance
  val nv noise             # Johnson noise
  var i i                  # current
  var i j                  # extra current
  electrical c             # extra centre pin
  values {
    if ((tk(t)>tc)|(alpha==0)) res = rn
    else res = rn*(tk(t)/tc)**alpha
    noise = sqrt(4*k*tk(t)*res)
  }
  control_section {
    noise_source(noise,j)
  }
  equations {
    i(p->c)+=i
    i: v(p)-v(m) = i*res
    i(c->m)+=j
    j: v(c)-v(m) = 0
    p(t)-=i*i*res+(v(c)-v(m))*j
  }
}
```

```
# TES thermometer, heat capacity and thermal conductance to bath
# combined.
element template teselement p m a b = alpha, rn, tc, c, gb, ti
  electrical p,m
  thermal_k a      # thermal connection to neighbour
  thermal_k b      # connection to bath
  number alpha     # steepness of transition
  number rn        # normal resistance
```

```
  number tc          # critical temperature
  number c           # heat capacity
  number gb          # thermal conductivity to bath
  number ti          # initial temperature
{
  testherm.t1 p m a = alpha, rn, tc
  heatcap.c1 a = c, ti
  thermcond_gradient.g1 a b = gb
}
```

```
# 1-dimensional TES building block
template tes p m a1 a2 b = alpha, rn, tc, c, g, gb, ti
  electrical p,m
  thermal_k a1,a2    # thermal connection to neighbours
  thermal_k b        # connection to bath
  number alpha       # steepness of transition
  number rn          # normal resistance
  number tc          # critical temperature
  number c           # heat capacity
  number g           # thermal conductivity
  number gb          # thermal conductivity to bath
  number ti          # initial temperature
{
  teselement.t1 p m a1 b = alpha, rn, tc, c, gb, ti
  thermcond.g1 a1 a2 = g
}
```

```
# 2-dimensional TES building block with connections in lateral
# and longitudinal directions
template tes2d e1 e2 e3 t1 t2 t3 b = alpha, rn, tc, c, g, gb, ti
  electrical e1,e2,e3
  thermal_k t1,t2,t3   # thermal connection to neighbours
  thermal_k b          # connection to bath
  number alpha         # steepness of transition
  number rn            # normal resistance
  number tc            # critical temperature
  number c             # heat capacity
  number g             # thermal conductivity
  number gb            # thermal conductivity to bath
  number ti            # initial temperature
{
```

```
  tes.tes1 e1 e2 t1 t2 b = alpha, rn, tc, c, g, gb, ti
  testtherm.tes2 e1 e3 t1 = alpha, rn, tc
  thermcond.g1 t1 t3 = g
}
```

BIBLIOGRAPHY

[1] P. Charles and F. Seward. *Exploring the X-ray universe*. Cambridge University Press, 1995.

[2] K. van der Heyden, E. Behar, J. Vink, A. Rasmussen, J. Kaastra, J. Bleeker, S. Kahn and R. Mewe. High-resolution X-ray imaging and spectroscopy of N 103B. *A&A* **392**: 955–962, 2002.

[3] M. Sako, S. Kahn, E. Behar, J. Kaastra, A. Brinkman, T. Boller, E. Puchnarewicz, R. Starling, D. Liedahl, J. Clavel and M. Santos-Lleo. Complex resonance absorption structure in the X-ray spectrum of IRAS 13349+2438. *A&A* **365**: L168–L176, 2001.

[4] D. Wollman, K. Irwin, G. Hilton, L. Dulcie, D. Newbury and J. Martinis. High-resolution, energy-dispersive microcalorimeter spectrometer for X-ray microanalysis. *J. Microscopy* **188** (3): 196–223, 1997.

[5] E. Leblanc, P. de Marcillac, N. Coron, J. Leblanc, M. Loidl, J. Metge and J. Bouchard. A new absolute method for the standardization of radionuclides emitting low-energy radiation. *Appl. Radiat. Isot.* **56** (1–2): 245–251, 2002.

[6] G. Fraser. *X-ray detectors in astronomy*. Cambridge astrophysics series. Cambridge University Press, 1989.

[7] R. den Hartog, A. Kozorezov, D. Martin, G. Brammertz, P. Verhoeve, A. Peacock, F. Scholze and D. Goldie. Large-format distributed read-out imaging devices for X-ray imaging spectroscopy. In F. Porter, D. McCammon, M. Galeazzi and C. Stahle (eds.), *AIP Conference Proceedings LTD-9*, vol. 605, 11–14. AIP, 2002.

[8] B. Mazin, P. Day, J. Zmuidzinas and H. Leduc. Multiplexable kinetic inductance detectors. In F. Porter, D. McCammon, M. Galeazzi and C. Stahle (eds.), *AIP Conference Proceedings LTD-9*, vol. 605, 309–312. AIP, 2002.

[9] C. Ens. Magnetic sensors for X-ray and gamma-ray detection. In F. Porter, D. McCammon, M. Galeazzi and C. Stahle (eds.), *AIP Conference Proceedings LTD-9*, vol. 605, 5–10. AIP, 2002.

[10] T. V. Duzer and C. Turner. *Principles of Superconductive Devices and Circuits*. Prentice Hall PTR, second edn., 1999.

[11] J. Martinis, G. Hilton, K. Irwin and D. Wollman. Calculation of T_c in a normal-superconductor bilayer using the microscopic-based Usadel theory. *Nucl. Instrum. Methods A* **444**: 23–27, 2000.

[12] S. Moseley, J. Mather and D. McCammon. Thermal detectors as X-ray spectrometers. *J. Appl. Phys.* **56** (5): 1257–1262, 1984.

[13] K. Irwin. An application of electrothermal feedback for high resolution cryogenic particle detection. *Appl. Phys. Lett.* **66** (15): 1998–2000, 1995.

[14] M. Galezzi and D. McCammon. Microcalorimeter and bolometer model. *J. Appl. Phys.* **93** (8): 4856–4869, 2003.

[15] M. de Nivelle, M. Bruijn, R. de Vries, J. Wijnbergen, T. Heidenblut, B. Schwierzi, W. Michalke and E. Steinbeis. Low-noise high-Tc superconducting bolometers on silicon nitride membranes for far-infrared detection. *J. Appl. Phys.* **82** (10): 4719–4726, 1997.

[16] J. Mather. Bolometer noise: nonequilibrium theory. *Appl. Opt.* **21** (6): 1125–1129, 1982.

[17] P. de Korte, M. Bavdaz, M. Duband, A. Holland, A. Peacock and L. Strüder. The X-ray evolving universe spectroscopy mission (XEUS) requirements of the X-ray focal plane instruments. In R. Hoover and A. Walker (eds.), *Proc. SPIE*, vol. 3766, 103–126. 1999.

[18] B. Henke, E. Gullikson and J. Davis. X-ray interactions: photoabsorption, scattering, transmission, and reflection at E = 50–30000 eV, Z = 1–92. *Atomic Data and Nuclear Data Tables* **54** (2): 181–342, 1993. Convenient lookup facility at `http://www-cxro.lbl.gov/optical_constants/`.

[19] C. Kittel. *Introduction to Solid State Physics*. John Wiley & Sons, seventh edn., 1996.

[20] K. Irwin, G. Hilton, D. Wollman and J. Martinis. Thermal-response time of superconducting transistion-edge microcalorimeters. *J. Appl. Phys.* **83** (8): 3978–3985, 1998.

[21] M. Korevaar. *High energy resolution micro-calorimeters for X-rays*. Master's thesis, Utrecht University, 2003.

[22] M. Leivo and J. Pekola. Thermal characteristics of silicon nitride membranes at sub-Kelvin temperatures. *Appl. Phys. Lett.* **72** (11): 1305–1307, 1998.

[23] W. Holmes, J.M.Gildemeister, P. Richards and V. Kotsubo. Measurement of thermal transport in low stress silicon nitride films. *Appl. Phys. Lett.* **72** (18): 2250–2252, 1998.

[24] G. Hilton, J. Martinis, K. Irwin, N. Bergren, D. Wollman, M. Huber, S. Deiker and S. Nam. Microfabricated transition-edge X-ray detectors. *IEEE Trans. Appl. Supercond.* **11** (1): 739–742, 2001.

[25] G. Hölzer, M. Fritsch, M. Deutsch, J. Härtwig and E. Förster. K $\alpha_{1,2}$ and K $\beta_{1,3}$ X-ray emission lines of the 3d transition metals. *Phys. Rev. A* **56** (6): 4554–4568, 1997. Note that the given widths W_i are the *half* widths at half maximum, not FWHM as stated in the paper. The I_i of the Mn Kα_{22} Lorenzian is 0.10 instead of 0.010.

[26] C. Stahle and G. Hilton. Workshop on Transition Edge Sensor Device Physics, NIST, Boulder, CO, 25–26 April 2002. Private communication.

[27] C. Poole, H. Farach and R. Creswick. *Superconductivity*. Academic Press, 1995.

[28] G. van Gurp. Flux-transport noise in type-II superconductors. *Phys. Rev.* **166** (2): 436–446, 1968.

[29] A. Luukanen, K. Kinnunen, A. Nuottajärvi, H. Hoevers, W. Bergmann Tiest and J. Pekola. Fluctuation-limited noise in a superconducting transition-edge sensor. *Phys. Rev. Lett.* **90** (23): 238306, 2003.

[30] H. Hoevers, A. Bento, M. Bruijn, L. Gottardi, M. Korevaar, W. Mels and P. de Korte. Thermal fluctuation noise in a voltage biased superconducting transition edge thermometer. *Appl. Phys. Lett.* **77** (26): 4422–4424, 2000.

[31] R. Voss and J. Clarke. Flicker ($1/f$) noise: Equilibrium temperature and resistance fluctuations. *Phys. Rev. B* **13** (2): 556–573, 1976.

[32] A. Germeau. SRON internal report.

[33] M. Lindeman, R. Brekosky, E. Figueroa-Feliciano, F. Finkbeiner, M. Li, C. Stahle, C.M.Stahle and N. Tralshawala. Performance of Mo/Au TES microcalorimeters. In F. Porter, D. McCammon, M. Galeazzi and C. Stahle (eds.), *AIP Conference Proceedings LTD-9*, vol. 605, 203–206. AIP, 2002.

[34] C. Stahle, M. Lindeman, E. Figueroa-Feliciano, M. Li, N. Tralshawala, F. Finkbeiner, R. Brekosky and J. Chervenak. Arraying compact pixels of transition-edge microcalorimeters for imaging X-ray spectroscopy. In F. Porter, D. McCammon, M. Galeazzi and C. Stahle (eds.), *AIP Conference Proceedings LTD-9*, vol. 605, 223–226. AIP, 2002.

[35] G. Hilton, J. Beall, S. Deiker, J. Beyer, L. Vale, C. Reintsema, J. Ullom and K. Irwin. Surface micromachining for transition edge detectors. *IEEE Trans. Appl. Supercond.* **13** (2): 664–667, 2003.

[36] M. Bruijn, N. Baars, W. Bergmann Tiest, A. Germeau, H. Hoevers, P. de Korte, W. Mels, M. Ridder, E. Krouwer, J. van Baar and R. Wiegerink. Development of an array of transition edge sensors for application in X-ray astronomy. *Nucl. Instrum. Methods A* 2004 (in press).

[37] F. Finkbeiner, R. Brekosky, J. Chervenak, E. Figueroa-Feliciano, M. Li, M. Lindeman, C. Stahle, C. Stahle and N. Tralshawala. Fabrication of close-packed TES microcalorimeter arrays using superconducting molybdenum/gold transition-edge sensors. In F. Porter, D. McCammon, M. Galeazzi and C. Stahle (eds.), *AIP Conference Proceedings LTD-9*, vol. 605, 215–218. AIP, 2002.

[38] K. Irwin. SQUID multiplexers for transition-edge sensors. *Physica C* **368**: 203–210, 2002.

[39] M. Kiviranta, H. Seppää, J. van der Kuur and P. de Korte. SQUID-based readout schemes for microcalorimeter arrays. In F. Porter, D. McCammon, M. Galeazzi and C. Stahle (eds.), *AIP Conference Proceedings LTD-9*, vol. 605, 295–300. AIP, 2002.

[40] J. Beyer, P. de Korte, C. Reintsema, S. Nam, M. MacIntosh, G. Hilton, L. Vale and K. Irwin. Performance of 32-channel time-division SQUID multiplexer for cryogenic detector arrays. *IEEE Trans. Appl. Supercond.* **13** (2): 649–652, 2003.

[41] J. van der Kuur, P. de Korte, H. Hoevers, W. Bergmann Tiest, N. Baars, M. Ridder, E. Krouwer, M. Bruijn, M. Kiviranta and H. Seppä. AC biased TES-based X-ray microcalorimeter with an energy resolution of 6.3 eV at 5.89 keV. *IEEE Trans. Appl. Supercond.* **13** (2): 638–642, 2003.

[42] F. Porter, R. Almy, E. Apodaca, E. Figueroa-Feliciano, M. Galeazzi, R. Kelley, D. McCammon, C. Stahle, A. Szymkowiak and W. Sanders. The XQC microcalorimeter sounding rocket: a stable LTD platform 30 seconds after rocket motor burnout. *Nucl. Instrum. Methods A* **444**: 220–223, 2000.

[43] B. Rabii, C. Winant, M. E. Abroe, P. Ade, A. Balbi, J. Bock, J. Borrill, A. Boscaleri, P. de Bernardis, J. Collins, P. Ferreira, S. Hanany, V. Hristov, A. Jaffe, B. Johnson, A. Lange, A. Lee, C. Netterfield, E. Pascale, P. Richards, G. Smoot, R. Stompor and J. Wu. Maxima: A balloon-borne cosmic microwave background anisotropy experiment 2003. Submitted to ApJ.

[44] ASTRO-E website. `http://lheawww.gsfc.nasa.gov/docs/xray/astroe/`.

[45] P. Shirron, E. Canavan, M. Dipirro, M. Jackson, J. Panek and J. Tuttle. A continuous low-temperature magnetic refrigerator. In F. Porter, D. McCammon, M. Galeazzi and C. Stahle (eds.), *AIP Conference Proceedings LTD-9*, vol. 605, 379–382. AIP, 2002.

[46] W. Press, S. Teukolsky, W. Vetterling and B. Flannery. *Numerical recipes in C*. Cambridge university press, second edn., 1992.

[47] V. Radeka and N. Karlovac. Least-square-error amplitude measurement of pulse signals in presense of noise. *Nucl. Instrum. Methods* **52**: 86–92, 1967.

[48] P. Nicholson. *Nuclear Electronics*, section 3.2.3. John Wiley & Sons, 1982.

[49] A. Szymkowiak, R. Kelley, S. Moseley and C. Stahle. Signal processing for microcalorimeters. *J. Low Temperature Phys.* **93** (3/4): 281–285, 1993.

SUMMARY

This thesis describes the development and device physics of an X-ray microcalorimeter. This is a device for measuring the energy of X-rays. The microcalorimeter measures the temperature increase that is the result of the absorption of an X-ray photon. Since the devices described in this thesis are produced using photolithographic techniques, they have the potential, in combination with suitable X-ray optics, to be made into imaging arrays. The availability of an imaging X-ray spectrometer with a high energy resolving power will have a significant impact in astronomy and material analysis. In astronomy, X-ray spectra provide information about high-energy processes taking place in the universe. In material analysis, the structure and composition of materials can be determined. The work described here is guided by therequirements of an instrument for XEUS, a future space-based astrophysical observatory.

The microcalorimeter is based on a superconducting-to-normal phase transition edge thermometer (TES). This is a superconductor that is voltage-biased in the very narrow transition from superconducting to resistive behaviour. In the transition, the electrical resistance is very sensitive to changes in the temperature, making the TES a good temperature to resistance transducer. The resistive element is easily incorporated in an electrical read-out circuit. The TES is coupled to a cold bath, providing a temperature reference. A voltage-biased TES benefits from negative electro-thermal feedback, which stabilises the sensor and shortens the response time. The energy resolving power of the microcalorimeter is limited by noise. In this thesis, this noise is studied in detail, both in experimental sensors as well as through simulations.

The specifications of the microcalorimeter are subject to a number of constraints. In particular, there is a trade-off between absorption efficiency, detector area and resolving power. The sensor described in this thesis is optimised for the demands of the XEUS mission. The sensor is fabricated using existing Si_3N_4 micromachining and thin-film photolithographical techniques. For testing, there are a number of requirements of which a stable bath temperature and bias voltage are the most important.

Several sensors with small square absorbers were manufactured and tested. With an operating temperature of 0.1 K, their energy resolution was about 4.5 eV for X-ray photons of 5.9 keV. This is equivalent to a resolving power of 1300. Furthermore, a sensor with a bigger, overhanging absorber with a 'mushroom' shape was tested, with a similar result. This energy resolution is satisfactory, but not as good as predicted by theory. This

discrepancy was investigated and forms the heart of this thesis. The difference between theory and measurement was explained by a combination of two effects:

Firstly, because the TES and absorber are seperate parts in the sensor, there can be an exchange of energy between the two. This results in an internal noise component which deteriorates the energy resolution. By changing the sensor geometry, we were able to influence and reduce the spectral density of this noise component. Using a numerical noise simulation, several geometries were evaluated. An analytical relation was derived for the magnitude of this internal noise component as a function of the geometry. Based on the knowledge about the influence of the geometry on the noise, an optimised geometry was designed.

Secondly, besides the internal noise, there is another effect that causes a difference between the theoretical and measured resolution. The predicted resolution is based on a small-signal model, which assumes limited excursions over the transition of the TES. For actual X-ray pulses that use a significant part of the dynamic range of the TES, this model was found to be incorrect. The large excursions cause the pulse shape to deviate from the ideal shape as assumed by the small-signal model. Because of this, the small-signal model predicts a smaller amount of noise to be present in the filtered signal than is the case in reality. This caused the theory to predict a better resolution than could actually be measured. Using measured pulse shapes, a more accurate prediction was made, which is in agreement with the measurements. A simple large-signal model was constructed to simulate pulse shapes based on the sensor parameters. With this model, the energy resolution can be described as a function of the size of the excursion over the transition (equivalent to different X-ray photon energy or device heat capacity). The model can be used for performance prediction at arbitrary X-ray energies and for improved sensor optimisation.

Finally, we have looked at the requirements that using this type of sensor in a space-borne instrument puts on the devices. They were tested for radiation hardness and stability over time. For use in an instrument, imaging capability is required. This makes it necessary to use an array of microcalorimeters. Among the challenges related to the design of a microcalorimeter array are the uniform coupling of the pixels to the cold bath, the lay-out of the electrical wires and multiplexing of the signals.

SAMENVATTING

Dit proefschrift beschrijft de ontwikkeling en de natuurkunde van een röntgenmicrocalorimeter. Dit is een sensor voor het meten van de energie van röntgenstraling. De microcalorimeter meet de temperatuurverhoging die het gevolg is van de absorptie van een röntgenfoton. Aangezien de in dit proefschrift beschreven sensoren geproduceerd worden met behulp van fotolithografische technieken, hebben ze de mogelijkheid om, in combinatie met geschikte röntgenoptiek, tot afbeeldende rasters samengesteld te worden. De beschikbaarheid van een afbeeldende röntgenspectrometer met een hoog energiescheidend vermogen zal een aanmerkelijk invloed hebben in de sterrenkunde en de materiaalanalyse. In de sterrenkunde verschaffen röntgenspectra informatie over hoogenergetische processen in het heelal. In de materiaalanalyse kan de structuur en de samenstelling van materialen bepaald worden. Het hier beschreven werk wordt geleid door de eisen voor een instrument voor XEUS, een toekomstig astrofysisch observatorium in de ruimte.

De microcalorimeter is gebaseerd op een supergeleidende-naar-normale faseovergangsthermometer (TES). Dit is een supergeleider die in de zeer smalle overgang van supergeleidend naar weerstandshebbend gedrag ingesteld wordt met een elektrische spanning. In de overgang is de elektrische weerstand zeer gevoelig voor veranderingen in de temperatuur, zodat de TES een goede omzetter is van temperatuur naar weerstand. Het weerstandselement is op eenvoudige wijze op te nemen in een elektrisch uitleescircuit. De TES is gekoppeld met een koudebad dat een temperatuursreferentie vormt. Een met een spanning ingestelde TES profiteert van negatieve elektro-thermische terugkoppeling, hetgeen de sensor stabiliseert en de reactietijd verkort. Het energiescheidend vermogen van de microcalorimeter wordt beperkt door ruis. In dit proefschrift wordt deze ruis in detail bestudeerd, zowel in experimentele sensoren als door middel van simulaties.

De specificaties van de microcalorimeter zijn onderworpen aan een aantal beperkingen. In het bijzonder is er een afweging tussen absorptierendement, detectoroppervlak en scheidend vermogen. De sensor beschreven in dit proefschrift is geoptimaliseerd volgens de eisen van de XEUS missie. De sensor wordt gemaakt door middel van bestaande Si_3N_4 bewerkingsprocessen op microschaal en dunne-film fotolithografische technieken. Voor het testen is er een aantal eisen waarvan stabiele badtemperatuur en instelspanning de belangrijkste zijn.

Verschillende sensoren met vierkante absorptie-elementen werden gemaakt en getest. Bij een bedrijfstemperatuur van 0.1 K was hun energieresolutie ongeveer 4.5 eV voor

röntgenfotonen van 5.9 keV. Dit komt overeen met een scheidend vermogen van 1300. Bovendien werd een sensor met een groter, overhangend absorptie-element met een 'paddestoelvorm' getest, met een soortgelijk resultaat. Deze energieresolutie is bevredigend, maar niet zo goed als voorspeld werd door de theorie. Deze tegenstelling werd onderzocht en vormt de kern van dit proefschrift. Het verschil tussen de theorie en de metingen werd verklaard door een combinatie van twee effecten:

Ten eerste kan er, omdat de TES en het absorptie-element afzonderlijke delen van de sensor zijn, een energie-uitwisseling plaatsvinden tussen beide. Dit heeft een interne ruiscomponent tot gevolg, die de energieresolutie verslechtert. Door de sensorgeometrie te veranderen waren wij in staat de spectrale dichtheid van deze ruiscomponent te beinvloeden en te verminderen. Door gebruik te maken van een numerieke ruissimulatie werd een aantal geometrieën geëvalueerd. Een analytisch verband werd afgeleid voor de grootte van deze interne ruiscomponent als functie van de geometrie. Gebaseerd op de kennis over de invloed van de geometrie op de ruis werd een geoptimaliseerde geometrie ontworpen.

Ten tweede is er naast de ruis een ander effect dat een verschil veroorzaakt tussen de theoretische en de gemeten resolutie. De voorspelde resolutie is gebaseerd op een klein-signaalmodel, dat beperkte uitwijkingen over de overgang van de TES aanneemt. Voor daadwerkelijke röntgenpulsen die een aanmerkelijk deel van het dynamisch bereik van de TES gebruiken is dit model onjuist gebleken. De grote uitwijkingen veroorzaken dat de pulsvorm afwijkt van de ideale vorm zoals die aangenomen wordt door het klein-signaalmodel. Hierdoor voorspelt het klein-signaalmodel dat er een kleinere hoeveelheid ruis aanwezig is in het gefilterde signaal dan in het echt het geval is. Dit zorgde ervoor dat de theorie een betere resolutie voorspelde dan daadwerkelijk gemeten kon worden. Door gebruik te maken van gemeten pulsvormen werd een nauwkeuriger voorspelling gedaan die in overeenstemming is met de metingen. Een eenvoudig groot-signaalmodel werd opgesteld om pulsvormen te simuleren op basis van de sensorparameters. Met dit model kan de energieresolutie beschreven worden als functie van van de grootte van de uitwijking over de overgang (overeenkomend met verschillende röntgenfotonenergie of warmtecapaciteit van de sensor). Dit model kan gebruikt worden voor het voorspellen van de prestaties bij willekeurige röntgenenergieën en voor verbeterde sensoroptimalisatie.

Tenslotte hebben we gekeken naar de eisen die het gebruik van een sensor van dit type in een instrument in de ruimte stelt aan de componenten. Zij werden getest op stralingshardheid en stabiliteit over lange duur. Voor gebruik in een instrument is de mogelijkheid tot het maken van afbeeldingen vereist. Dit maakt het noodzakelijk om een raster van microcalorimeters te gebruiken. De uitdagingen met betrekking tot het ontwerp van een raster van microcalorimeters zijn onder andere de uniforme koppeling van de beeldelementen naar het koudebad, de lay-out van de elektrische aansluitingen en het multiplexen van de signalen.

PUBLICATIONS

W. Bergmann Tiest, M. Bruijn, H. Hoevers, P. de Korte, J. van der Kuur and W. Mels. Understanding TES microcalorimeter noise and energy resolution. *Nucl. Instrum. Methods A*, 2004 (in press).

W. Bergmann Tiest, M. Bruijn, W. Mels, P. de Korte and H. Hoevers. Cryogene microcalorimeters. *Ned. tijdschrift v. natuurkunde*, **67** (10): 300–305, 2001.

W.M. Bergmann Tiest, H.F.C. Hoevers, W.A. Mels, M.L. Ridder, M.P. Bruijn, P.A.J. de Korte and M.E. Huber. Performance of X-ray microcalorimeters with an energy resolution below 4.5 eV and 100 μs response time. In F.S. Porter, D. McCammon, M. Galeazzi and C.K. Stahle (eds.), *AIP Conference Proceedings LTD-9*, vol. 605, 199–202. AIP, 2002.

M.P. Bruijn, N.H.R. Baars, W.M. Bergmann Tiest, A. Germeau, H.F.C. Hoevers, P.A.J. de Korte, W.A. Mels, M.L. Ridder, E. Krouwer, J.J. van Baar and R.J. Wiegerink. Development of an array of transition edge sensors for application in X-ray astronomy. *Nucl. Instrum. Methods A*, 2004 (in press).

M.P. Bruijn, W.M. Bergmann Tiest, H.F.C Hoevers, J. van der Kuur, W.A. Mels and P.A.J. de Korte. Towards a cryogenic imaging array of transition edge X-ray microcalorimeters. In *Proc. SPIE*, vol. 4012, 145–153. 2000.

M.P. Bruijn, M. Ridder, H.F.C. Hoevers, W.M. Bergmann Tiest, P.A.J. de Korte, Z. Moktadir, R.J. Wiegerink, E. Berenschot and M. Elwenspoek. Micro-machining of a cryogenic imaging array of transition edge X-ray microcalorimeters. In *Proc. Sensor Technology Conf.*, 179–184. 2001.

M.P. Bruijn, M.L. Ridder, E. Krouwer, H.F.C. Hoevers, W.M. Bergmann Tiest, P.A.J. de Korte, Z. Moktadir, R. Wiegerink, J. van der Kuur, D. van Gelder and M. Elwenspoek. Development of arrays of transition edge sensors for application in X-ray astronomy. In *Proc. SeSens*, 598–602. 2002.

M.P. Bruijn, W.M. Bergmann Tiest, H.F.C. Hoevers, E. Krouwer, J. van der Kuur, M.L. Ridder, Z. Moktadir, R.J. Wiegerink, D. van Gelder and M. Elwenspoek. Development of arrays of transition edge sensors for application in X-ray astronomy. *Nucl. Instrum. Methods A*, **513**: 143–146, 2003.

S.I. Han, R. Almy, E. Apodaca, W. Bergmann, S. Deiker, A. Lesser, D. McCammon, K. Rawlins, R.L. Kelley, S.H. Moseley, F.S. Porter, C.K. Stahle and A.E. Szymkowiak. Intrinsic $1/f$ noise in doped silicon thermistors for cryogenic calorimeters. In *Proc. SPIE*, vol. 3445, 640–644. 1998.

P.A.J. de Korte, W.M. Bergmann Tiest, M.P. Bruijn, H.F.C. Hoevers, J. van der Kuur, W.A. Mels and M. Ridder. Noise and energy resolution of X-ray microcalorimeters. *IEEE Trans. Appl. Supercond.*, **11** (1): 747–750, 2001.

P.A.J. de Korte, H.F.C. Hoevers, J.W.A. den Herder, J.A.M. Bleeker, W.M. Bergmann Tiest, M.P. Bruijn, M.L. Ridder, R.J. Wiegerink, J.S. Kaastra, J. van der Kuur and W.A. Mels. A TES X-ray microcalorimeter-array for imaging spectroscopy. In *Proc. SPIE*, vol. 4851, 779–789. 2003.

J. van der Kuur, P.A.J. de Korte, H.F.C. Hoevers, W.M. Bergmann Tiest, N.H.R. Baars, M.L. Ridder, E. Krouwer, M.P. Bruijn, M. Kiviranta and H. Seppä. AC biased TES-based X-ray microcalorimeter with an energy resolution of 6.3 eV at 5.89 keV. *IEEE Trans. Appl. Supercond.*, **13** (2): 638–642, 2003.

A. Luukanen, W.M. Bergmann Tiest, H.F.C. Hoevers, K.M. Kinnunen, I. Maasilta, A.K. Nuottajärvi and J.P. Pekola. Critical fluctuations as a source of excess noise in a TES in a Corbino geometry. *Nucl. Instrum. Methods A*, 2004 (in press).

A. Luukanen, K.M. Kinnunen, A.K. Nuottajärvi, H.F.C. Hoevers, W.M. Bergmann Tiest and J.P. Pekola. Fluctuation-limited noise in a superconducting transition-edge sensor. *Phys. Rev. Lett.*, **90** (23): 238306, 2003.

D. McCammon, R. Almy, E. Apodaca, W. Bergmann Tiest, W. Cui, S. Deiker, M. Galeazzi, M. Juda, A. Lesser, T. Mihara, J.P. Morgenthaler, W.T. Sanders, J. Zhang, E. Figueroa-Feliciano, R.L. Kelley, S.H. Moseley, R.F. Mushotzky, F.S. Porter, C.K. Stahle and A.E. Szymkowiak. A high spectral resolution observation of the soft X-ray diffuse background with thermal detectors. *ApJ*, **576** (1): 188–203, 2002.

C.H. Whitford, W.M. Bergmann Tiest and A.D. Holland. Practical considerations in optimal filtering of TES signals. *Nucl. Instrum. Methods A*, 2004 (in press).

CURRICULUM VITAE

Wouter Michiel Bergmann Tiest

Born August 7, 1975 in Naarden

1987–1993:   VWO at St. Vituscollege in Bussum

1993–1994:   English language course at EF Language School, Cambridge, UK

1994–1999:   Physics and Astronomy at Utrecht University. Master's research project at the University of Wisconsin, Madison, USA. Master's degree in experimental physics 'met genoegen'

1999–2003:   Employed by SRON National Institute for Space Research, Utrecht

TRANSITION EDGE

Alpha

ITFN

Resistance Bridge

Loop Gain

Black hole

Convolution

Pile-up

Line Forest

Johnson

CRYOSTAT

Photon Peak

Integral

FERMI SEA

Full Width Half Maximum

X-ray

Phonon

Supernova Remnants

T

S   E

1   2   3 4   6   10   20   40 60 100